INVESTIGATIONS OF SPHEROMAK PLASMA DYNAMICS:

HIGH-SPEED IMAGING AT THE SUSTAINED SPHEROMAK PHYSICS
EXPERIMENT AND MAGNETIC DIAGNOSTICS AT THE CALTECH SPHEROMAK
EXPERIMENT

Thesis by

Carlos Alejandro Romero Talamás

In Partial Fulfillment of the Requirements

for the Degree of

Doctor of Philosophy

California Institute of Technology

Pasadena, California

2005

(Defended September 28, 2004)

Acknowledgments

I have many persons and organizations to thank for their help and support during my time as a Ph.D. student at Caltech. The list of those I will mention in this section might seem long, but it was thanks to them, and many more whom I might have met only briefly or through correspondence, that I consider my experience at Caltech unique, unforgettable, and very rewarding.

I am grateful to my advisor, Prof. Paul M. Bellan, for his excellent mentoring and careful advice. Whether it was in informal discussions during lunch, or meticulous derivations of equations on the blackboard, Paul always showed an enthusiasm for science that was contagious. This manuscript also benefitted greatly from his help. I will continue to value his advise and friendship beyond my days as a graduate student.

Thanks to those that are or have been part of Bellan's Plasma Physics group during my time here: Steve Pracko, Shreekrishna Tripathi, Settivoine You, Gunsu Yun, Deepak Kumar, Erik Grandstet, Scott Hsu, Freddy Hansen, Eli Jorné, Dave Felt, Frank Cosso, and Eleonora Chetverikova. I thank them for their valuable help and advice when assembling an experiment or analyzing data. Special thanks to Steve for helping me proofread many documents (including parts of this manuscript), and for his patience and wisdom in helping me understand the U.S. culture; to Shreekrishna and Sett, for all the physics discussions which helped me organize my ideas and forced me to be precise, and for sharing their expertise to solve so many hardware and software problems; to Dave, for his help during the construction of the magnetic probe, and for his patience in explaining to me so many details of the hardware that he built. To all, I would like to thank them for their great friendship and support.

Abstract

This thesis consists of two parts. The first part describes a specially designed high-speed imaging system installed at the Sustained Spheromak Physics Experiment (SSPX). Thousands of images have been obtained at SSPX using a high-speed, 1280 x 1024 pixel, cooled and intensified CCD camera with double frame capability, and show unprecedented details of the SSPX plasma. From these images, three different stages were identified according to distinct plasma features. These stages are breakdown and ejection, sustainment, and decay.

During the breakdown and ejection stage, $\mathbf{J} \times \mathbf{B}$ forces push the plasma and stretches the initial vacuum field into the flux conserver. As the plasma enters the field of view of the camera, undulations in the expansion front are visible. These undulations are caused by filaments formed in the gun region, and merge as they travel towards the flux conserver and rotate around the chamber axis. In less than 100 μs after breakdown, a transient plasma column is formed. Just microseconds after this, the column bends impulsively and seemingly merges in the toroidal direction (around the axis of the chamber). It is conjectured that the bending precedes a reconnection event that leads to magnetic flux amplification.

Images taken during the sustainment stage show the presence of a central column which is very stable. Some images suggest nested current channels in this column. Comparisons of column diameter measurements versus numerical modeling (using the CORSICA code) are presented here. Bright and distinct patterns were observed on the surface of the source cathode, and appear to be related to the sustainment column and open flux surfaces. These patterns elongate toroidally in a constant direction which depends on the bias field polarity. It is conjectured that the pattern motion is caused by $E \times B$ drifts, or $J \times B$ effects near the cathode surface.

Most of the hardware was specially designed for the high-speed imaging system, including a double-branch fiber bundle that was used to produce rough tomography (at midplane) of the transient central column. The algorithm used for tomographical reconstruction is based on a maximum entropy restoration method that was also used to improve noisy and blurry images.

The second part of this thesis describes a 60-element magnetic probe array that was constructed using miniature commercial chip inductors. The coils are oriented in orthogonal directions to yield three-dimensional information. The probe has been used to investigate magnetic evolution at the Caltech Spheromak Experiment.

Table of Contents

List of Figures

List of Tables

Chapter 1

Introduction

1.1 Spheromaks

Spheromaks are plasmas (ionized gases) with very large internal currents and internal magnetic fields and are in a nearly force-free equilibrium [1]. This means that currents and magnetic fields are essentially aligned. In mathematical terms, force free equilibrium in plasmas can be expressed as $\mathbf{J} \times \mathbf{B} \simeq \mathbf{0}$, which implies that the current $\mathbf{J}$ is parallel (and thus proportional) to the magnetic field $\mathbf{B}$. Using Ampere's law, $\nabla \times \mathbf{B} = \mu_0 \mathbf{J}$, the following expression is readily obtained

$$\nabla \times \mathbf{B} = \lambda \mathbf{B} \tag{1.1}$$

where λ is effectively an eigenvalue.

The spheromak is considered a plasma confinement concept and is toroidal in nature. However, this concept has the interesting property that no materials such as magnetic field coils or vacuum vessels link the torus (unlike other magnetic confinement configurations, e.g. the Tokamak [2], the Stellarator [3,4] or the Reversed Field Pinch [5]). The first wall (or first closed magnetic flux surface) of a spheromak is topologically a sphere. Both toroidal and poloidal fields exist within this first wall, and the flux surfaces in which these fields exist are closed. These are indeed defining characteristics of a spheromak and result from plasma self-organization that tends to the so-called Taylor (or minimum energy) states [6,7]. In a relaxed state, the confinement of plasma by magnetic fields involves symmetry [1]. Lundquist [8] was the first to report the solution to Equation 1.1 in cylindrical

geometry. He showed that this equation provides the simple solution

$$\mathbf{B} = B \left(J_1(\lambda r)\hat{\theta} + J_0(\lambda r)\hat{z} \right) \tag{1.2}$$

where J_0 and J_1 are Bessel functions and B is a constant.

It is possible to solve Equation 1.1 in spherical geometry [9]. In this case, the poloidal flux Ψ can be determined by evaluating the field B_r that intercepts a dome-shaped surface with a constant radius r subtending a conical angle θ about the z axis. The resulting expression for Ψ is

$$\Psi = \frac{2\pi r B_0 a}{\lambda(r^2 + z^2)} \left(\frac{\sin\left(\lambda\sqrt{r^2 + z^2}\right)}{\lambda\sqrt{r^2 + z^2}} - \cos\left(\lambda\sqrt{r^2 + z^2}\right) \right) \tag{1.3}$$

Figure 1.1 shows a plot with contours of constant Ψ. Although the flux configuration is axisymmetric, the magnetic field on those surfaces is helicoidal. This condition makes numerical modeling of spheromaks inherently difficult, making experiments necessary in order to validate the theory. Interestingly (and presented here only as a curiosity), the contours obtained from Equation 1.3 are mathematically the same as the ones obtained in a special type of purely hydrodynamic configuration known as Hill's vortex ring [10, 11]. Figure 1.2 shows an example of a very laminar vortex ring produced in a laboratory using smoke in air. Note the similarity between the contours shown in Figure 1.1 and the ones in Figure 1.2.

Spheromaks have been produced in laboratories around the world using various methods [13, 14] . Scientific research of these configurations has traditionally been geared towards the goal of building controlled thermonuclear fusion reactors. However, since spheromaks arise from turbulent states by relaxing to organized (or at least less turbulent) states, it is believed that this configuration occurs in nature. Thus, spheromak research is relevant to other fields, such as astrophysical jet mechanics [15], solar prominence formation
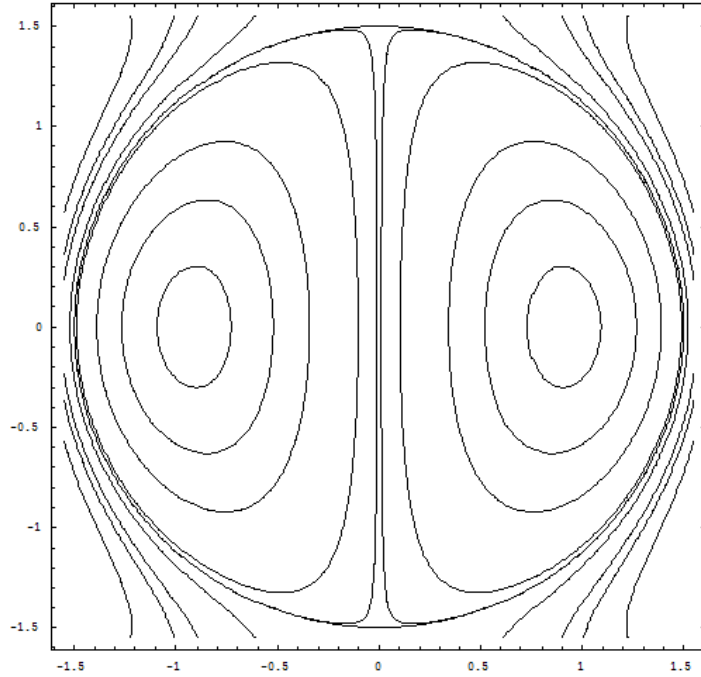
Fig. 1.1. Plot of contours of constant Ψ for a field that satisfies Equation 1.1. The vertical axis corresponds to the z direction, and the horizontal axis to the r direction. The first wall corresponds to the circumference with radius $r = 1.5$. Arbitrary units used on both axes.

and evolution [16–18], magnetospheric dynamics [22], and magnetic reconnection [20,21]. These and other applications are described in detail by Bellan in reference [23].

1.2 Bounded versus unbounded spheromaks

Until recently, all laboratory spheromaks had bounded walls, i.e., where the first wall of the spheromak conforms to the shape of the vacuum chamber in which it is created. These chamber walls are also used as flux-conserving boundaries, preventing the magnetic field in the closed flux surfaces from escaping the chamber (at least on the timescale of the experiment). As mentioned in the previous section, the main goal of spheromak research is controlled thermonuclear fusion. For this reason, plasma confinement time, density,
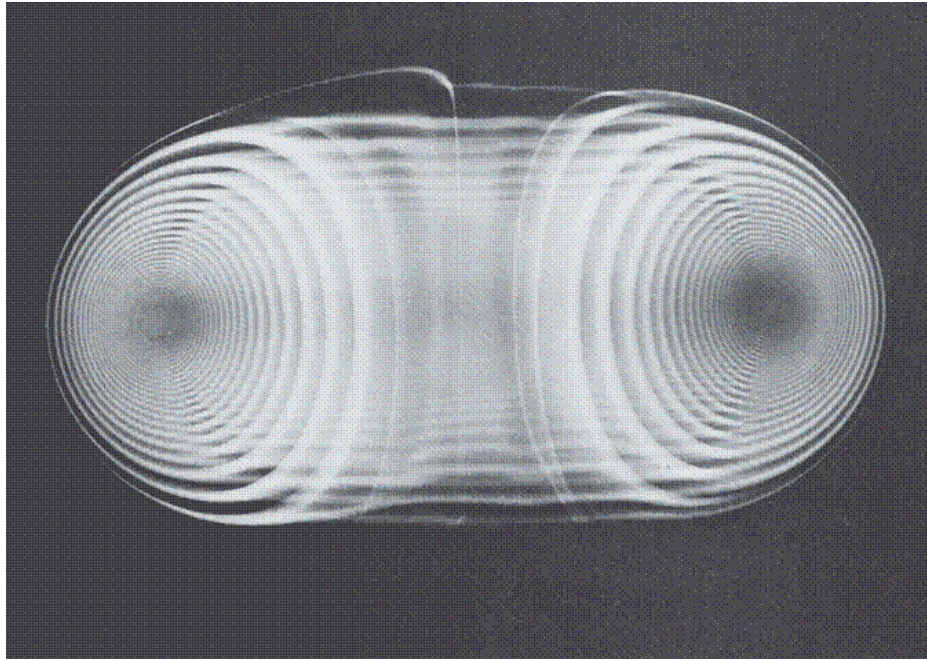
Fig. 1.2. Structure of a smoke ring. Image by R. H. Magarvey and C. S. MacLatchy [12], reproduced with kind permission of the National Research Council of Canada.

and temperature are important parameters. If a spheromak fusion reactor is ever built, the plasma temperature will have to be greater than 100,000,000 K.

Although recent experimental results at the Sustained Spheromak Physics Experiment (SSPX, see Chapter 2) are encouraging [24, 25], temperatures and confinement times achieved in spheromaks are still orders of magnitude lower than those required for fusion conditions. Thus, spheromak formation, sustainment, decay, and plasma-wall interactions are ongoing areas of research crucial to fusion applications.

Many space plasmas, in contrast, have the property of being unbounded. These plasmas might be held together by gravity (like the Sun and other stars), or by magnetohydrodynamic (MHD) effects (like solar prominences), or by a combination of both (like astrophysical jets). For the cases in which spheromak physics is relevant, the evolution of

space plasmas might be topologically different from the evolution of bounded spheromaks, even though the configurations might be similar after Taylor relaxation.

In any spheromak experiment (bounded or unbounded), the details of helicity injection and how it can cause instabilities are poorly understood. Magnetic helicity, $K = \int \mathbf{A} \cdot \mathbf{B} dV$ (where $\mathbf{B} = \nabla \times \mathbf{A}$), is the measure of the linkage of magnetic flux. If a plasma obeys ideal MHD (i.e., the plasma remains 'frozen' to the field lines), then the total helicity for that plasma remains constant [7]. The formation and sustainment of spheromaks can be modeled using concepts of helicity injection and decay [26]. At Caltech, experiments are carried out to investigate the detailed physics of helicity injection in unbounded spheromaks[1]. A magnetized coaxial planar plasma gun [27] fires plasma into a large (1.3 m diameter and 2 m long) vacuum chamber. The evolution of the spheromak's magnetic topology is studied on the sub-microsecond time-scale using high-speed photography [28] and magnetic probes (see Chapter 8, also published in Reference [29]). Even though the plasma gun is axisymmetric, photographs reveal the formation of reproducible non-axisymmetric flux tubes (see Figure 1.3).

The study of bounded and unbounded spheromaks is helping elucidate the complex dynamics involved in creating these self-organized configurations and the instabilities that could destroy them.

---

[1] The Caltech spheromak facility is the only experimental laboratory reported to date in which the spheromaks produced are considered unbounded.
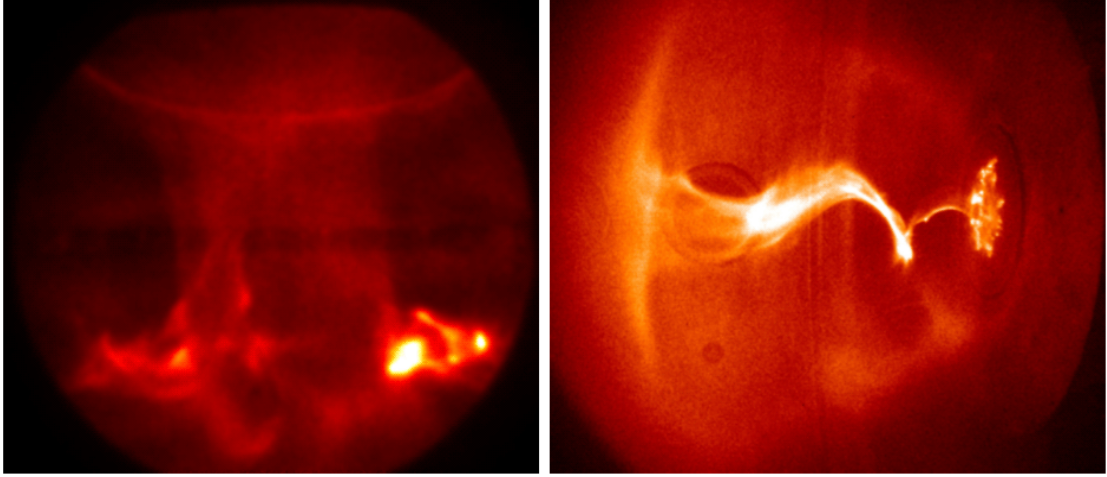
Fig. 1.3. Example of bounded and unbounded spheromak formation. Left, early formation of the SSPX plasma. The walls of the cathode and anode act as a flux conserver. Chamber axis is vertical. Right, kink formation in the unbounded Caltech spheromak facility (image courtesy of S. C. Hsu and P. M. Bellan). Chamber axis is horizontal.

1.3 Why are spheromaks attractive candidates for thermonuclear fusion?

The answer lies in the topological simplicity of the reactor chamber and magnetic system, and the ability to contain high plasma betas[2] [30]. Compared to the tokamak (considered the 'conventional' magnetic fusion concept), a spheromak reactor would result in a much smaller mass, overall dimensions, and cost. Studies performed in the 1980's [31, 32] showed that the mass of the fusion power core would be on the order of 500 tons. In contrast, the International Thermonuclear Experimental Reactor (ITER) [33], a tokamak that if built will produce the first burning plasma that could yield fusion power 10 times the input power, is expected to have a mass of 20,000 tons.

---

[2] Plasma beta, or β, is the ratio of hydrodynamic to magnetic pressure, i.e., $\beta \equiv 2\mu_o p/B^2$, where p is the plasma pressure, B is the magnetic field, and μ_o is the permeability of free space.

Of all the known fusion reactions, the deuterium-tritium (D-T) reaction has the highest reaction rate for the lowest temperature, 60 keV[3]. Even at temperatures of 10 keV (which are more likely for practical fusion reactors) the D-T reaction rate is still higher than all others by at least an order of magnitude [34]. This fact, together with the extremely low costs expected for obtaining deuterium and tritium, makes D-T the best candidate for the first commercial fusion energy reactor. The D-T reaction yields a total of 17.6 MeV [35]

$$D + T \rightarrow He^4 \text{ (3.5 MeV)} + n \text{ (14.1 MeV)} \tag{1.4}$$
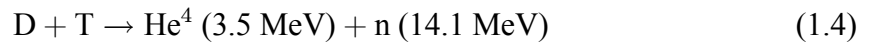
which is about an order of magnitude higher than the nuclear yield per fuel mass in typical fission reactors. The ionized alpha particles (He^4) would be trapped inside the closed magnetic flux surfaces (until removed through divertors), but the neutrons would easily escape across the magnetic field. A way to slow down the neutrons produced in a fusion reaction would be to use liquid metal and molten salt walls. This would be a way of converting neutron kinetic energy into thermal energy for commercial energy generation, without the problem of activating or damaging the reactor walls.

A recent study by Moir et al. [36] proposes a spheromak fusion reactor with liquid molten salts and liquid metal walls. Figure 1.4 shows this design next to the more detailed ITER design. Note that both designs are approximately equal in size. However, liquid walls would be easier to implement in a spheromak reactor due to its simple shape.

It is very likely that ITER will be the first experimental device to study the physics of burning and magnetically confined plasmas under reactor-relevant conditions. The design and engineering of materials and components to withstand harsh neutron bombardment and temperature conditions will also be a valuable contribution to future commercial fusion energy reactors. Hopefully, the parallel research and development of alternative concepts like

---

[3]   The temperature associated with 1 eV is 1.1604×10^4 K.
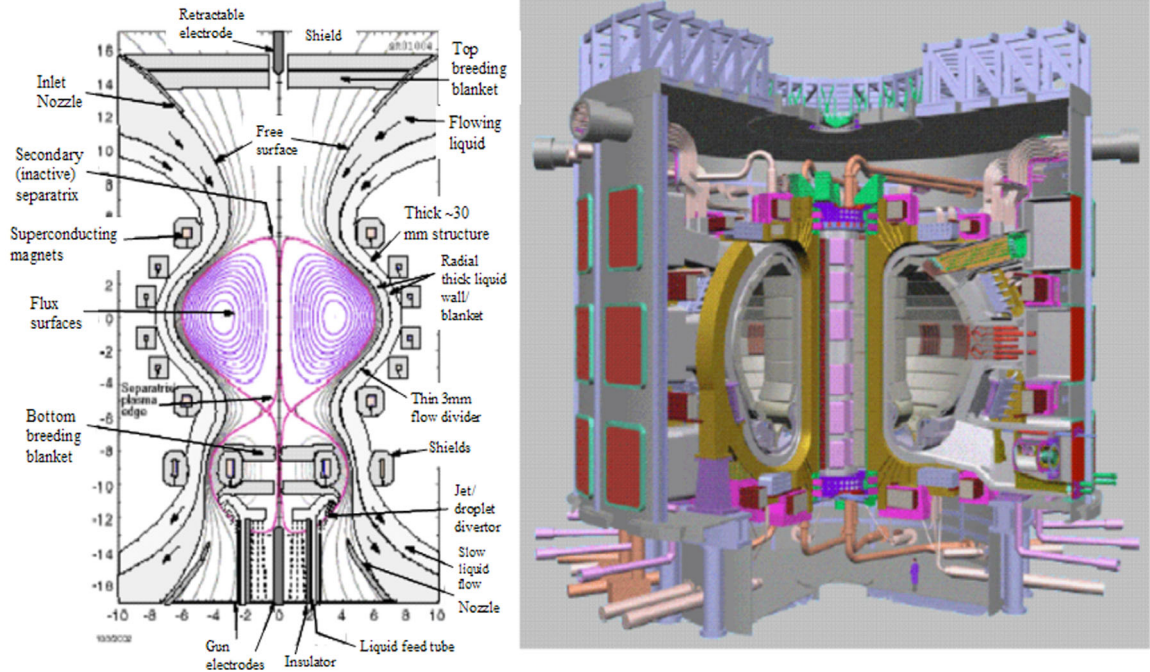
Fig. 1.4. Left: Liquid wall spheromak reactor design by Moir et al. [36] (reproduced with kind permission of the author). Fusion power 2500 MW, energy amplification Q = 20. Liquid walls conform to the shape of the reactor by centrifugal forces from the rotation of the reactor walls (mechanisms complexity not shown). Right: Artist concept of the ITER design [37] (reproduced with kind permission of ITER). Fusion power 500 MW, energy amplification Q = 10. Energy conversion from neutron to electrical power is not incorporated in the ITER design. The spheromak, unlike the tokamak, has no coils linking the closed magnetic surfaces.

the spheromak will benefit from the knowledge gained from ITER, resulting in commercially viable and environmentally friendly energy production reactors in the near future.

1.4 Motivation behind the present work

The motivation behind the work in this thesis is to further understanding of spheromaks. To aid in the study of phenomena such as reconnection and filamentation, a high-speed imaging system was installed at the Sustained Spheromak Physics Experiment (SSPX). The imaging system has the advantage of being completely passive and remote (does not perturb

the plasma), and its field of view covers most of the plasma volume. With phenomena such as filamentation and plasma-surface interactions being important in any magnetic fusion configuration, photographic images provide researchers the unique opportunity to visualize these features with a great level of detail. Images allow, to some extent, the possibility of measuring the size and position of these features. If several images per shot are acquired, it is sometimes possible to also measure their displacement and velocity (the camera used at SSPX provided two images per shot). These characteristics made the high-speed camera system a stand-alone diagnostic. Furthermore, the capability to synchronize the images to known signals (typically plasma breakdown) allowed the coordination of the camera timing with other diagnostics installed on SSPX. Thus high-speed images served also as a complement to other diagnostics.

Another important diagnostic for plasmas is the signal from magnetic probes. At SSPX, magnetic probes are placed at the walls of the flux conserver. Measurements from these probes serve as constraints for numerical reconstruction codes. Given these constraints and certain assumptions, the magnetic field can be estimated for all the plasma volume during a given shot. Unfortunately, non-axisymmetric complex structure in the magnetic field usually cannot be reconstructed using these codes. To measure this complex structure, probes immersed in the plasma are necessary. However, at SSPX the ability to produce high-temperature plasmas is very important, and thus these intrusive probes are undesired since plasma interaction with the surface of probes might create impurities that decrease, through atomic line radiation, the maximum temperature achievable in a plasma shot.

At the Caltech Spheromak Experiment the cleanliness requirements are not as stringent as at SSPX. Although at Caltech the spheromaks produced are considered unbounded, it is also interesting to investigate how magnetic fields evolve in this configuration. For

this reason, a multielement magnetic probe was installed at the Caltech Spheromak Experiment. The probe consists of sixty commercial miniature chip inductors that are arranged in a linear array of twenty clusters (20 mm apart from each other). Each cluster measures the magnetic field in three orthogonal directions, thus yielding three-dimensional information of the magnetic field at the probe location. The probe has been used to create contour maps of the magnetic flux from the unbounded spheromaks produced at Caltech.

1.5 Organization of this thesis

This thesis consists of two parts and a summary (Chapter 9). The first part covers the implementation in SSPX of the high-speed imaging system and the measurements obtained with it, and it spans chapters 2 through 7. The second part covers the details of the multielement magnetic probe, and is presented in Chapter 8.

The breakdown of the high-speed imaging part is as follows. A description of SSPX is presented in Chapter 2. The high-speed imaging hardware, including details of the optics, vacuum equipment, the camera, and remote operation of the equipment, are presented in Chapter 3. A classification of stages according to features seen in the high-speed images during a plasma shot in SSPX, is presented in Chapter 4. Measurements of the sustainment central column diameter (boundary of the open field lines) using high-speed images, and comparison to CORSICA (an MHD equilibrium reconstruction code), are presented in Chapter 5. Measurements and analysis of bright patterns observed near the surface of the cathode (inner electrode), are presented in Chapter 6. An image restoration method based on the maximum entropy principle (applied to information theory), and an adaptation of this method to rough tomography using only two projections, are presented in Chapter 7.

1.6 References

[1]   P. M. Bellan, *Spheromaks: A Practical Application of Magnetohydrodynamic Dynamos and Plasma Self-Organization,* (Imperial College Press, London, 2000), Chapter 1.

[2]   J. Wesson, *Tokamaks*, (Clarendon Press, Oxford, 1997).

[3]   D. A. Hartmann, Fusion Sci. and Tech. **45** (2T), 64 (2004).

[4]   J. F. Lyon, Plasma Phys. Control. Fusion. **32** (11), 1041 (1990).

[5]   P. Martin, Plasma Phys. Control. Fusion. **41**, A247 (1999).

[6]   J. B. Taylor, Phys. Rev. Lett. **33** (19), 1139 (1974).

[7]   J. B. Taylor, Phys. Plasmas **7** (5), 1623 (2000).

[8]   S. Lundquist, Arkiv for Fysik **B2**, 361 (1950).

[9]   P. M. Bellan, *Spheromaks: A Practical Application of Magnetohydrodynamic Dynamos and Plasma Self-Organization,* (Imperial College Press, London, 2000), pp. 80 - 85.

[10] G. K. Batchelor, *An Introduction to Fluid Dynamics*, (Cambridge Mathematical Library, New York, 2002), pp. 522 - 539.

[11] K. Shariff and A. Leondard, Annu. Rev. Fluid Mech. **24**, 235 (1992).

[12] R. H. Magarvey and C. S. MacLatchy, Can. J. Phys. 42, 678 (1964).

[13] T. R. Jarboe, Plasma Phys. Control. Fusion **36**, 945 (1994).

[14] P. M. Bellan, *Spheromaks: A Practical Application of Magnetohydrodynamic Dynamos and Plasma Self-Organization,* (Imperial College Press, London, 2000), Chapter 7.

[15] S. C. Hsu and P. M. Bellan, Mon. Not. R. Astron. Soc. **334**, 257 (2002).

[16] P. M. Bellan and J. F. Hansen, Phys. Plasmas **5**, 1991 (1998).

[17] P. M. Bellan, J. Yee and J. F. Hansen, Earh Planets Space **53**, 495 (2001).

[18] J. F. Hansen and P. M. Bellan, Ap. J. **563**, L183 (2001).

[19] J. F. Hansen, S. K. P. Tripathi, and P. M. Bellan, Phys. Plasmas **11**, 3177 (2004).

[20] M. R. Brown, Phys. Plasmas **6**, 1717 (1999).

[21] C. D. Cothran, Geophys. Res. Lett. **30**, 1213 (2003).

[22] L. F. Burlaga, J. Geophys. Res. **93**, 7217 (1988).

[23] P. M. Bellan, *Spheromaks: A Practical Application of Magnetohydrodynamic Dynamos and Plasma Self-Organization,* (Imperial College Press, London, 2000), Chapters 16 and 17.

[24] H. S. McLean, S. Woodruff, E. B. Hooper, et al., Phys. Rev. Lett. **88** (12), art. no. 125004 (2002).

[25] S. Woodruff, D. N. Hill, B. W. Stallard, et al., Phys. Rev. Lett. **90** (9), art. no. 095001 (2003).

[26] P. M. Bellan, *Spheromaks: A Practical Application of Magnetohydrodynamic Dynamos and Plasma Self-Organization,* (Imperial College Press, London, 2000), Chapter 3.

[27] S. C. Hsu and P. M. Bellan, Phys. Rev. Lett. **90**, 215002 (2003).

[28] S. C. Hsu and P. M. Bellan, IEEE Trans. Plasma Sci. **30**, 10 (2002).

[29] C. A. Romero-Talamás, P. M. Bellan, and S. C. Hsu, Rev. Sci. Instrum. **75**, 2664 (2004).

[30] E. B. Hooper, J. H. Hammer, C. W. Barnes, et al., Fusion Technology **29**, 191 (1996).

[31] M. Katsurai and M. Yamada, Nucl. Fusion **22**, 1407 (1982).

[32] R. L. Hagenson and R. A. Krakowski, Fusion Tech. **8**, 1606 (1985).

[33] B. J. Green, Plasma Phys. Control. Fusion **45**, 687 (2003).

[34] J. Lilley, *Nuclear Physics Principles and Applications*, (John Wiley & Sons Ltd, Chichester, 2002), pp. 302-304.

[35] J. D. Huba et al., *NRL Plasma Formulary*. Naval Research Laboratory, Washington, 2002, p. 44.

[36] R. W. Moir, R. H. Bulmer, T. K. Fowler, et al., Fusion Sci. Tech. **44**, 317 (2003).

[37] *ITER website*, http://www.iter.org/, July 2, 2004.

Chapter 2

The sustained spheromak physics experiment

2.1 Introduction

In this chapter, an overview of the Sustained Spheromak Physics Experiment, SSPX, is presented. The SSPX is funded by the United States Department of Energy, and has been in operation at Lawrence Livermore National Laboratory (LLNL) since 1999. The motivation for SSPX is to explore the viability of the spheromak configuration as a thermonuclear fusion reactor. This experiment is aimed to address basic questions about the physics of spheromaks:

- How do currents in the spheromak plasma produce the spheromak configuration?

- How well do spheromak magnetic fields contain hot plasma?

This experiment, however, is intended to handle relatively cool temperatures (< 1 keV), not fusion level temperatures (about 10 keV), and is considered part of a group of concepts [1] that are classified as alternative[1] to the tokamak for fusion. In the scale of experimental magnetic fusion experiments, SSPX is relatively small in size, but with a diverse set of diagnostics. Figure 2.1 shows a picture of the outside of the vacuum chamber.

SSPX uses a magnetized coaxial gun to form and sustain the configuration by inject-ing helicity, $K \equiv \int A \cdot B d^3 r$, into a flux conserver. The total helicity in a spheromak is

---

[1]   In the U. S. they are called Innovative Confinement Concepts, or ICC's.
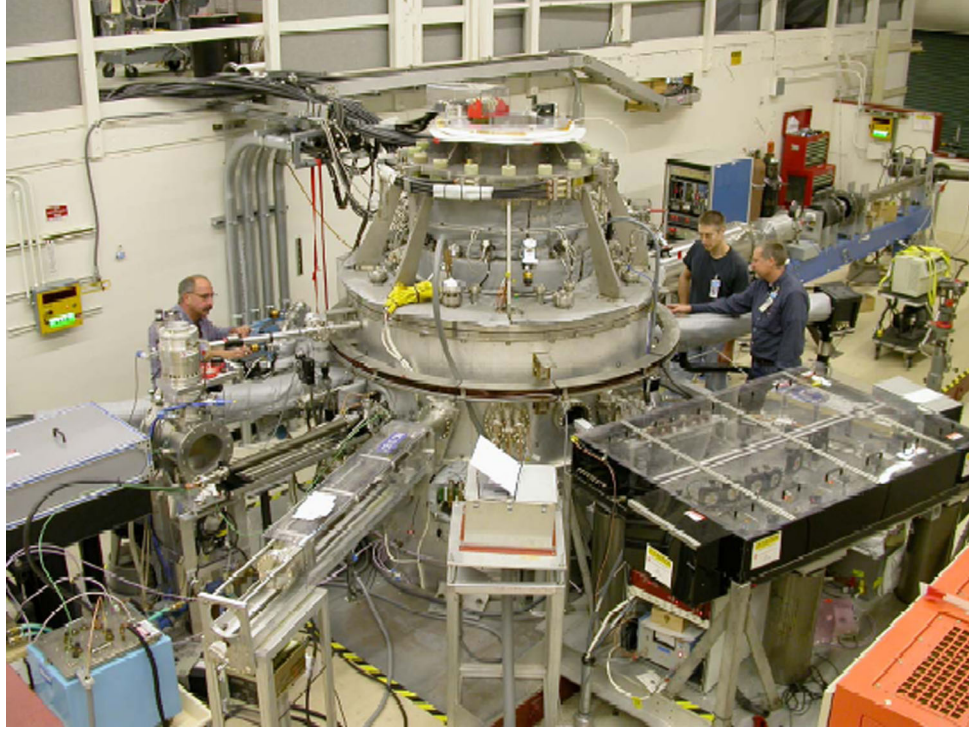
Fig. 2.1. Picture of the SSPX vacuum vessel, and the diagnostics around it. SSPX team members shown in this image (from left to right): Reg Wood, Chris Holcomb, and Harry McLean. Image courtesy of Dave N. Hill.

proportional to the stored magnetic energy W,

$$2\mu_0 W = \lambda K \tag{2.1}$$

where λ comes from the force free field solutions to $\nabla \times \mathbf{B} = \lambda \mathbf{B}$. The outer shell of the flux conserver serves as one electrode of the coaxial gun (typically the anode), and the inner shell serves as the other electrode (typically the cathode).

Helicity decays on a resistive time scale even for a weakly resistive plasma, unless there is a source that compensates for that decay. For a coaxial magnetized plasma gun, the rate of helicity injection is $2\psi_g V$, and so the helicity balance equation can be written as

$$dK/dt = 2\psi_g V - K/\tau_K \tag{2.2}$$
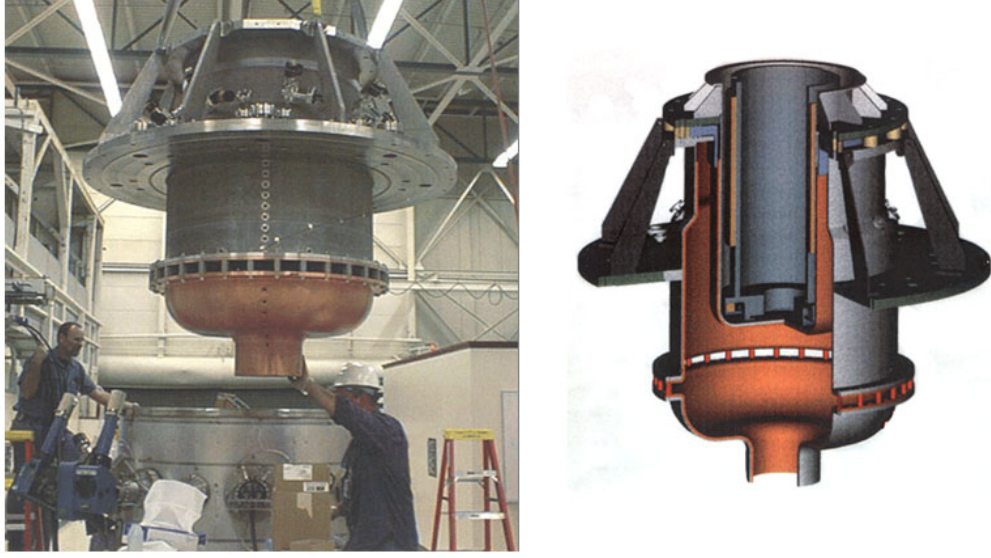
Fig. 2.2. Left: Installation of the flux conserver into the SSPX vacuum chamber. Right: Cuttaway view of the flux conserver. Images courtesy of Dave N. Hill.

where V is the gun voltage, ψ_g is the gun magnetic flux, and τ_K is the helicity decay time. Therefore, for a sustained spheromak, $dK/dt \approx 0$.

Figure 2.2 shows the 1-meter diameter flux conserver. The outer shell of the flux conserver has an opening that is held together by an array of posts. This opening is about 5 cm wide and is used for giving access to plasma diagnostics. The posts ensure good electrical conductivity between the lower and upper parts of the flux conserver shell. To create and sustain spheromaks, the SSPX facility has a large capacitor bank that can deliver peak currents > 400 kA, and sustain currents > 200 kA for more than 2 ms. The total plasma duration is 4 ms for a typical experimental shot (see Figure 2.3). Figure 2.4 shows a side view of the SSPX chamber, with the CORSICA numerical MHD reconstruction [2] of magnetic flux contours during sustainment. Open and closed magnetic flux surfaces are expected inside the flux conserver during gun current sustainment.
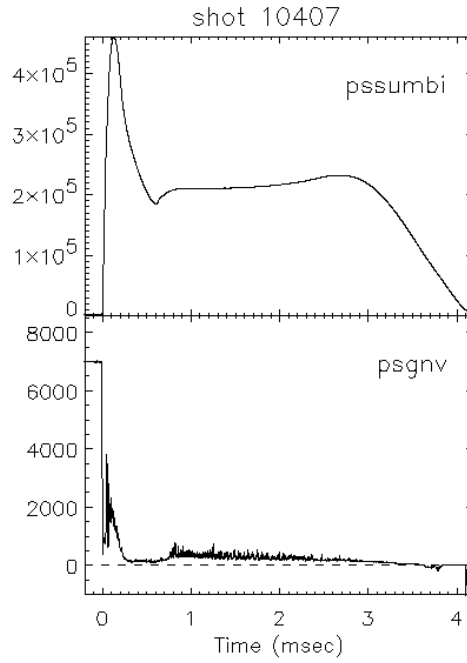
Fig. 2.3. Typical gun current (in amperes; upper frame) and voltage (in volts; lower frame) at SSPX.

2.2 Operation parameters

The goals of SSPX [3] include the following parameters: $n = 0.5 - 3 \times 10^{20}$ m^{-3}, $T_e \approx T_i = 0.1 - 0.5$ keV, $B = 0.5 - 1.5$ T, and $I_p = 0.5 - 1.5$ MA. Recent experimental results have increased the level of understanding of fluctuations in the spheromak plasma [4] and have led to a new mode of operating the SSPX gun [5]. This new mode gives the highest gun voltage during sustainment and the highest sustained helicity injection rate observed in SSPX. The more recent plasma parameters for a typical experimental shot [6] are presented in Table 2.1.
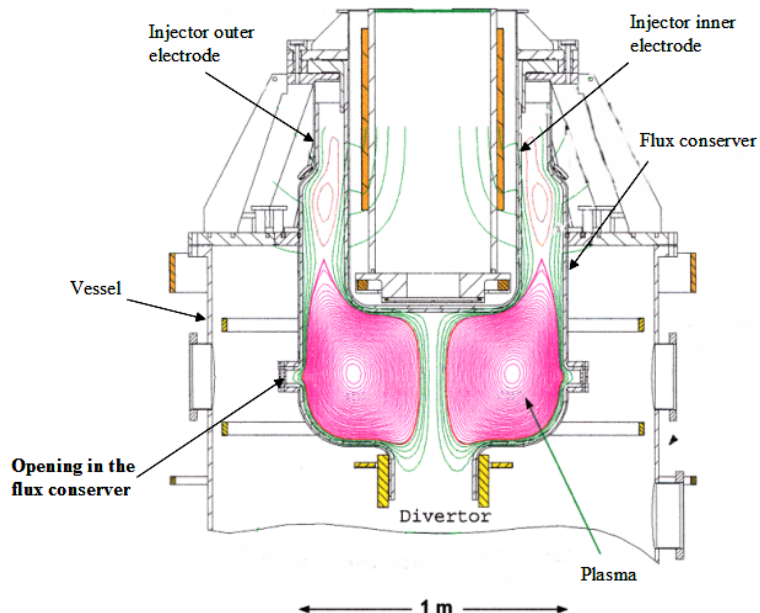
Fig. 2.4. SSPX with CORSICA modeling of equilibrium field profile. Image courtesy of Dave N. Hill.

2.3 Bias flux configuration options

The SSPX machine has 9 coils that can be used to produce a bias magnetic field for every plasma shot. All the coils can be selected individually for a particular shot. The coils and their identification numbers are shown in Figure 2.5. Depending on the combination of coils chosen and the polarity of the current in each coil, different configurations of the bias magnetic field can be produced. Some of those configurations are shown in Figure 2.6.

2.4 Diagnostics

SSPX is one of the best diagnosed experiments considered alternate to the tokamak. Figure 2.7 shows the main diagnostics and their position in the SSPX machine, and Figure 2.8 shows the position of the edge magnetic probes on a side view of the flux conserver. The
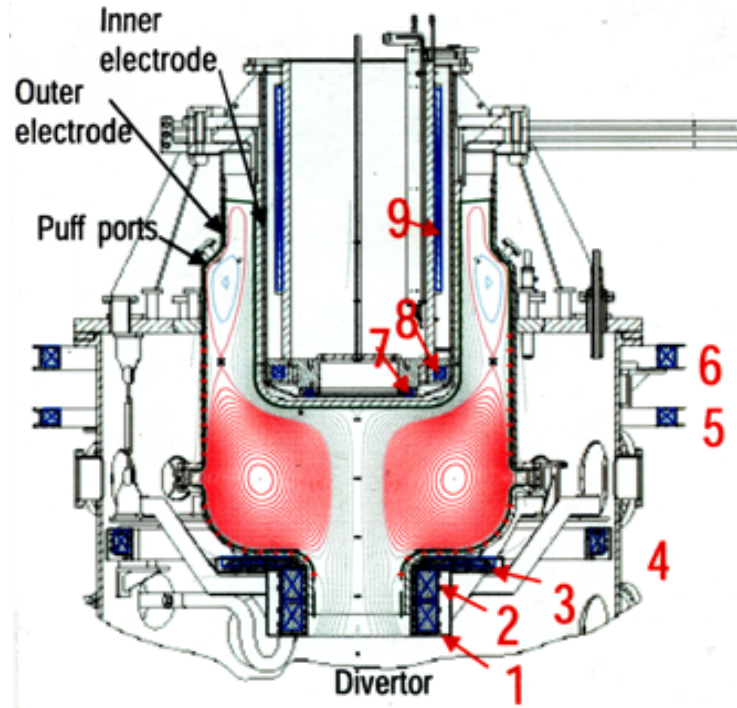
Fig. 2.5. Bias magnetic field coils at SSPX. Each coil is given a unique identification number, and can be operated independently from the others. Image courtesy of Dave N. Hill.
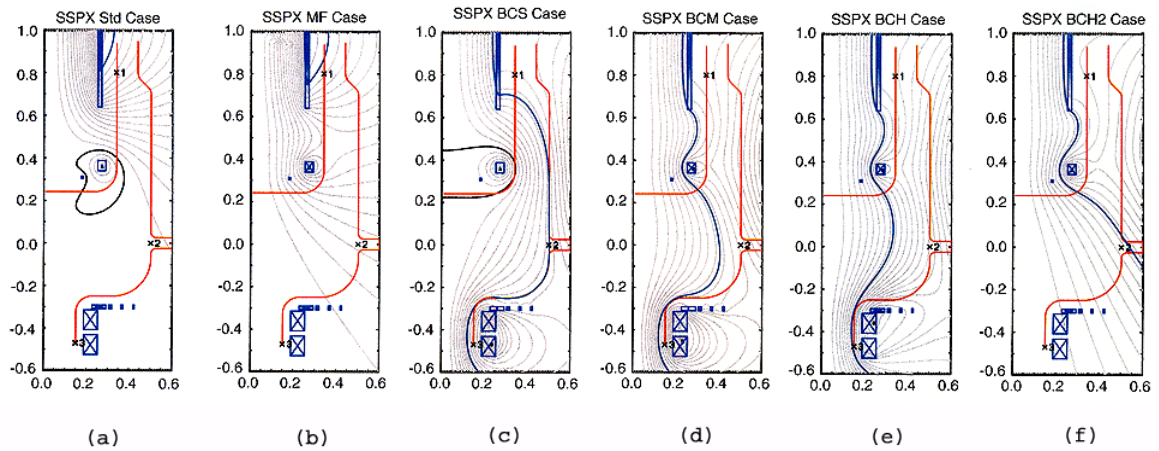
Fig. 2.6. Different bias flux configurations at SSPX. (a) Standard flux. (b) Modified flux. (c) BCS. (d) BCM. (e) BCH. (f) BCH2. Images courtesy of Dave N. Hill.
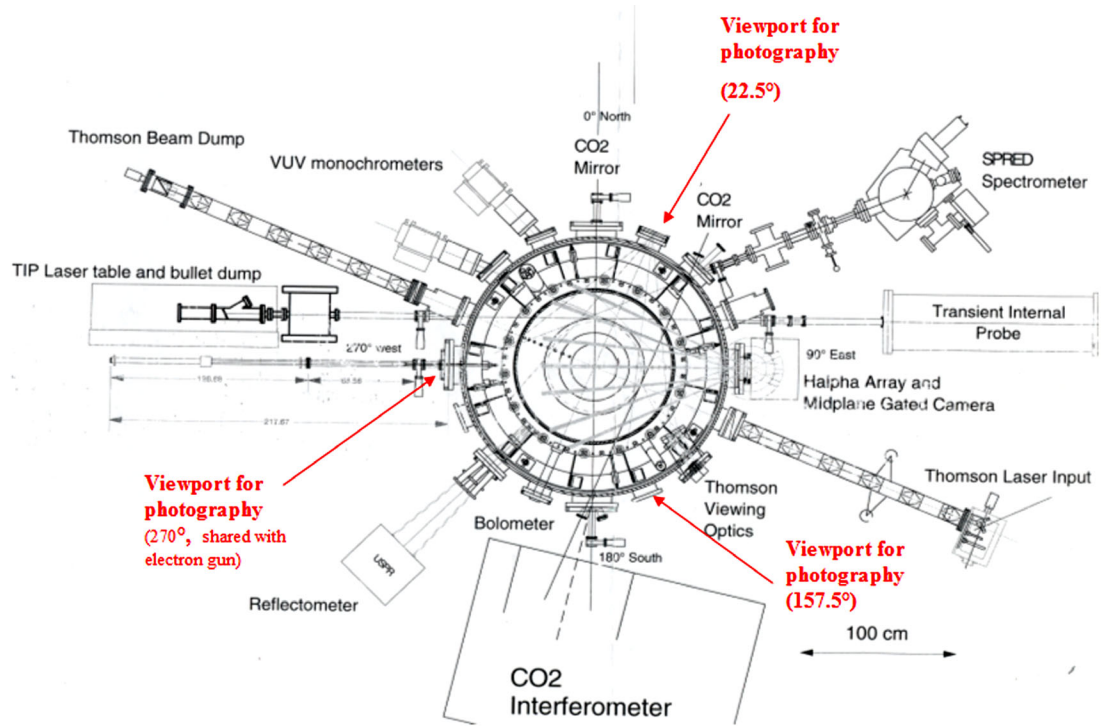
Fig. 2.7. Top view of SSPX diagnostics. Image courtesy of Dave N. Hill.
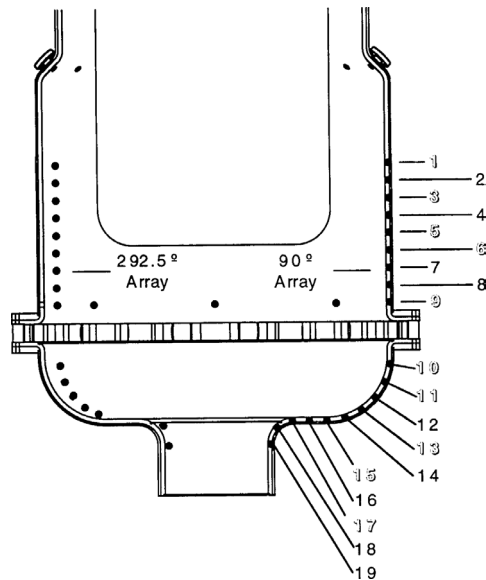
Fig. 2.8. Toroidal location of magnetic probes. Two arrays of magnetic probes at the wall of the flux conserver are shown: at $90\,^\circ$ and at $292\,^\circ$. Image courtesy of Dave N. Hill.

Radius of magnetic axis (m)	0.31
Minor radius (m)	0.23
Discharge current (kA)	200
Toroidal current (kA)	400
Edge poloidal field (T)	0.2
Pulse length (ms)	3.5
Electron temperature (eV)	20-200
Lundquist number, S	10^5
Fluctuations (kHz)	20
Plasma density (m^{-3})	5×10^{19}

Table 2.1. Typical SSPX plasma parameters.

diagnostics are listed in Table 2.2. Rows 1 through 24 in Table 2.2 are described by McLean et al. in Reference [7]. The high-speed imaging system in row 25 is described in detail in Chapter 3.

Diagnostics are normally armed (or prepared) before each plasma shot. The trigger signal for a particular diagnostic usually comes from the closing of the discharge capacitor bank switch, or from a sensor that measures plasma breakdown and gun current. The diagnostics can be operated independently. All the data recorded by the diagnostics is digitized and compiled in a computer server that can be accessed through the Internet (usually restricted to SSPX team members).

Diagnostic	Measures	Time resolved?	Spatial profile?
1. Profile Thompson scattering	n_e, T_e	Gated - single meas.	Yes
2. CO$_2$ laser	n_e	Yes	Two chords
3. USPR	n_e, fluctuations	Yes	Yes
4. Transient Internal Probe	Internal B_t, fluctuations	Yes	Yes
5. 16 ch. photodiode bolo array	P_{rad} energy loss distribution	Yes	Yes
6. 3 ch. filtered bolo array	P_{rad}, W_{rad}	Yes	Views midplane
7. 1 channel thermistor	W_{rad}	Integrating	Views midplane
8. SPRED spectrometer	W_{rad}, T_e, Spectral rad.	Integrating	Single chord
9. Ion doppler spectrometer	T_i, V_i	Yes	Can view select. chords
10. Wall magnetic probes	B_p, B_t at wall	Yes	Wall profile in z, theta
11. Flux conserver Rogowskis	Flux conserver posts current	Yes	Slot profile in theta
12. Visible spectrometer	Impurities	Integrating	Single chord
13. Hard x-ray	Runaway electrons	Yes	Single point
14. VUV monochrometers	Line ratios, impurities, T_e	Yes	Two chords
15. Midplane H_α array	Neutral hydrogen	Yes	Yes - 10 chords
16. Injector H_α	Neutral hydrogen	Yes	Single chord
17. Injector TV camera	Discharge visible light	Gated - single point	Yes
18. Midplane TV camera	Discharge visible light	Gated - single point	Yes
19. Bank Rogowskis	Cap. bank current, W_{input}	Yes	NA
20. Injector voltage	Injector voltage, W_{input}	Yes	NA
21. Bank room TV camera	Monitors for arcs	Yes	Yes
22. Injector room TV camera	Monitors for arcs	Yes	Yes
23. Residual gas analyzer	Vacuum sys. H$_2$O, evolved gas	Yes	NA
24. Vessel pressure	Vacuum sys., gas valve ops.	Yes	NA
25. High-speed ICCD camera	Discharge visible light	Gated - double point	Yes

Table 2.2. List of SSPX diagnostics. Rows 1 through 24 are described in detail in Reference [7]. Row 25 is described in Chapter 3.

2.5 References

[1]   D. C. Robinson, Phil. Trans. R. Soc. Lond. A **357**, 515 (1999).

[2]   J. A. Crotinger, L. LoDestro, L. D. Pearlstein, et al., *CORSICA: A comprehensive Simulation of Toroidal Magnetic Fusion Devices. Final Report to the LDRD Program, UCRL-1D-126284*, Lawrence Livermore National Laboratory, 1997.

[3]   E. B. Hooper, R. H. Bulmer, B. I. Cohen, et al., *Sustained Spheromak Physics Experiment*, UCRL-JC-132034, Lawrence Livermore National Laboratory, 1998.

[4]   H. S. McLean, S. Woodruff, E. B. Hooper, et al., Phys. Rev. Lett. **88** (12), art. no. 125004 (2002).

[5]   S. Woodruff, D. N. Hill, B. W. Stallard, et al., Phys. Rev. Lett. **90** (9), art. no. 095001 (2003).

[6]   D. N. Hill, *Proceedings of the Innovative Confinement Concepts Workshop 2004*, Madison. http://plasma.physics.wisc.edu/icc2004/html/pdfconf/114Hill.pdf. July 3, 2004.

[7]   H. S. McLean, A. Ahmed, D. Buchenauer, et al., Rev. Sci. Instrum. **72**, 556 (2001).

Chapter 3

Design and construction of the high-speed imaging diagnostic

3.1 Introduction

In this chapter, a description is presented of the design, construction, and operation of the high-speed imaging diagnostic for the Sustained Spheromak Physics Experiment, SSPX. The purpose of this diagnostic is to obtain images of the SSPX plasma during a discharge and use those images to

- help understand spheromak formation dynamics,

- measure, together with other diagnostics, quality of confinement,

- help in validating theory and numerical modeling of the SSPX spheromak,

- help in troubleshooting malfunctions of the equipment.

Various pieces of hardware had to be specially designed, built, and tested to accomplish this. A wide field of view and high-resolution are desired in order to obtain the most information from a single photograph. This principle was taken as the driving requirement in the design of the high-speed imaging system installed in SSPX. In addition to this requirement, operation, safety and machine constraints also had to be taken into account. The total set of requirements as agreed with the SSPX team during the design phase are summarized in Table 3.1:

1. The re-entrant ports shall be high-vacuum compatible.
2. Components exposed to plasma shall withstand ~40 MW of radiated power and 0.2 T fields during ~2ms, repeating every 3min.
3. To view the entire flux conserver, a high angular field of view is desired ($>$90deg).
4. The vacuum components shall be bakeable to 200 ^oC.
5. All components shall be serviceable and removable.
6. The system shall withstand gettering.

Table 3.1. Design requirements for the high-speed imaging system

A description of the hardware is presented in the sections below and is organized as follows. The vacuum hardware needed to obtain optical access to the flux conserver is presented in Section 3.2. The high-speed camera is presented in Section 3.3. Optical access to the flux conserver was challenging. However, it was possible to obtain images from up to two different views simultaneously with specially designed lenses and coherent optical fiber bundles. Details of the optical hardware are presented in Section 3.4. The manufacturer of the high-speed camera specified that the camera should not be operated in strong magnetic fields. For this reason, a magnetic shield had to be designed and installed to attenuate the field near the camera. Details of the magnetic shield are presented in Section 3.5. Camera mounts and supports are presented in Section 3.6.

3.2 Vacuum system

The SSPX vacuum chamber uses standard metal seal flanges[1] to maintain high-vacuum. This same standard was used for the re-entry port vacuum flanges used in the high-speed imaging system. All the metal components were made from 304 or 316 grade stainless steel. Both types of stainless steel are non-magnetic and do not interact chemically with

---

[1]   This type of flanges are commonly known as ConFlat, CF or knife-edge flanges.

other materials and gases used in the SSPX vacuum chamber. The vacuum system flanges, ports and mechanisms (those that would remain attached to the chamber during baking) were chosen or built to withstand an equilibrium temperature of 200 ^{o}C, as specified in Table 3.1.

3.2.1   First generation re-entry port system

It was determined that the camera lens should be placed close to the edge of the flux conserver to have a high angular field of view (design requirement 3 in Table 3.1). However, it was not desired to modify the shape of the flux conserver or drill holes through it. For this reason, the width at the midplane opening (~ 5 cm) of the flux conserver was taken as an additional constraint.

The SSPX port originally assigned to the high-speed imaging diagnostic was located at SSPX toroidal position 22.5 $^\circ$ (see SSPX schematics in Chapter 2), and had an 8 inch CF flange. The nominal inner diameter of an 8 inch flange is 6 inches. This inner dimension constrained the distance to the flux conserver at which the camera could be placed, since the high-speed camera (which is bigger than 6 inch on any of its sides) would not fit inside the re-entry port.

In order to take visible light photographs, a window was required in the re-entry port. The window used in this design was made of sapphire. Gettering, which is the process of depositing a thin film of contaminant-trapping material in plasma-facing components, was of concern because it could coat the window. Titanium is used as the gettering material at SSPX. Although the transmissivity of light through an exposed window is almost unchanged on a single gettering session, over many sessions the window eventually becomes opaque. For this reason, a shutter was designed and installed on the re-entry port to protect the window.
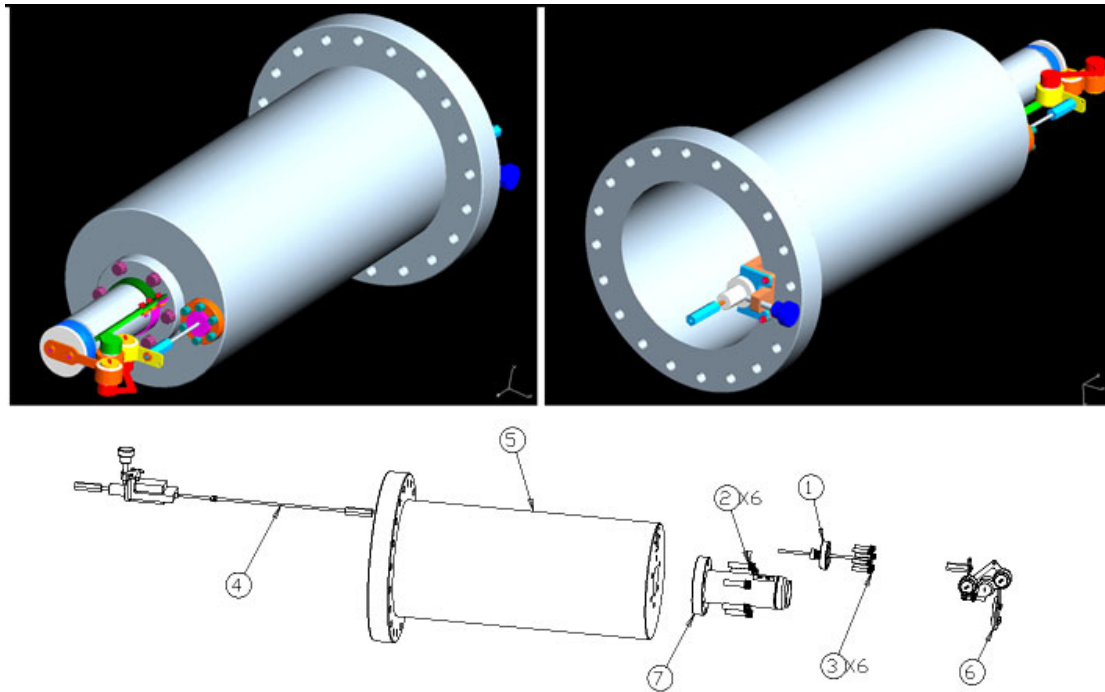
Fig. 3.1. Computer rendering of the first generation re-entry port. Upper left: plasma facing side of the port. The shutter mechanism is seen in closed configuration. Upper right: rear view of the re-entry port. Optics and other components can be placed inside the port and remain at atmospheric pressure. Note: Colors added for clarity. Most parts are stainless steel or ceramic. Bottom: exploded view of the re-entry port. 1) Bellows with support and flange. Used to transmit force between the shutter and latch mechanisms while keeping vacuum. 2) Bolts 1/4-28 x 1 inch. 3) Bolts 8-32 x 3/4 inch. 4) Latch mechanism. 5) Re-entry shell. The bigger OD is 8 inch. The knife-edge (not shown) is on the shutter side. 6) Shutter mechanism. 7) Small re-entry shell with window.

The complete design of the first generation re-entry port is shown in Figure 3.1. It was called the first generation re-entry port because it was the first high-speed imaging port to be installed at SSPX, with a window so close to the plasma. The latch shown in Figure 3.1 was operated manually, making it necessary for a member of the SSPX team to close the shutter before every gettering session, and open it for imaging. The shutter could be left open or closed during experimental runs, and if the camera was not in operation, it was decided to leave it closed to reduce damage to the window (from direct plasma impingement) during plasma shots.
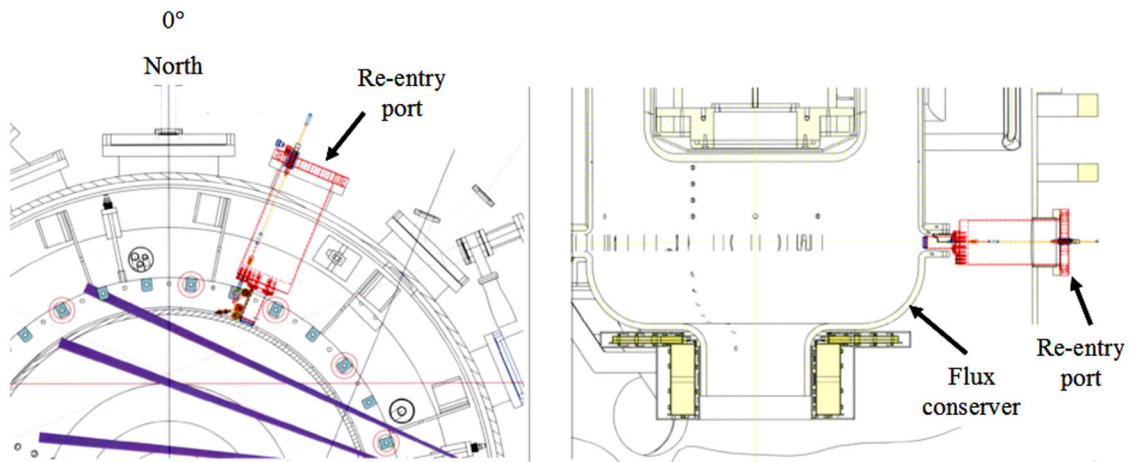
Fig. 3.2. Schematic view of the position of the first generaiton re-entry port in SSPX. Left: top view showing re-entry port installed at the 22.5° port. Right: side view. Note in both views that the small part of the re-entry port is very close to the inner edge of the flux conserver. Images courtesy of Harry S. McLean.

Figure 3.2 shows a schematic view of the position of the re-entry port in SSPX. Figure 3.3 shows a computer 3D rendering of the re-entry port in open and closed configurations as viewed from the inside of the flux conserver. The ceramic disk shown in this figure is the widest component of the shutter mechanism and has a diameter of 1.54 inch (39 mm).

There was enough clearance between any of the components of the re-entry port or shutter mechanism, and the flux conserver (including the posts that hold the flux conserver shell) to avoid mechanical interference and minimize the possibility of electrical arcs that could damage the mechanisms. In SSPX, induced currents could be strong enough to spot-weld metal components together. For that reason, care was taken that none of the moving parts had metal-to-metal moving joints. Instead, metal-to-ceramic joints were used for the vacuum components of the shutter mechanism, and metal-to-teflon was used for the latch mechanism, which was at atmospheric pressure.

The first generation re-entry port was tested for mechanical operation and leaks at the Caltech spheromak vacuum chamber before installing it on SSPX. All tests at Caltech were
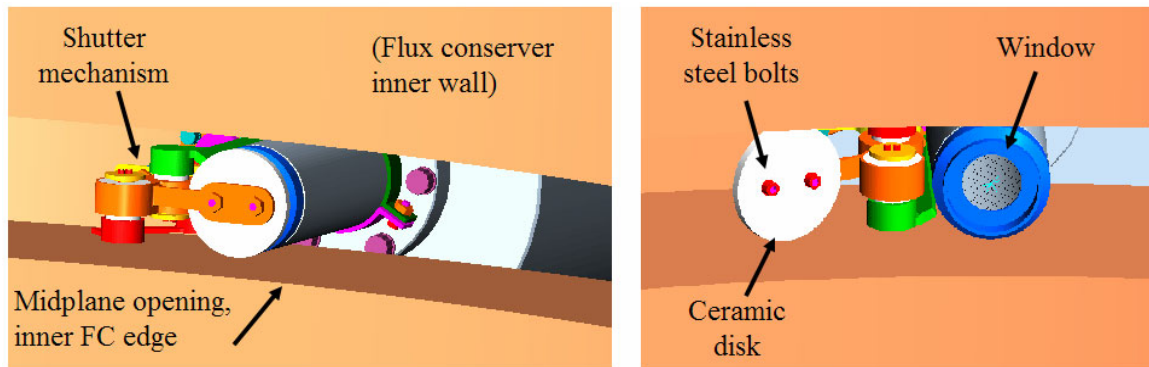
Fig. 3.3. First generation re-entry port viewed from inside the flux conserver (FC). The posts that hold the outer shell of the flux conserver are not shown for clarity.

satisfactory. Once shipped to SSPX, it was leak-checked again and then installed in the SSPX chamber. Images were successfully taken through the re-entry port's window using the high-speed camera.

The shutter mechanism eventually failed (by getting stuck and remaining in the open position) after hundreds of plasma shots taken over more than three months. The window was also damaged (metal-coated) so severely that it was not possible to continue taking images through it.

3.2.2 Failure analysis of the first generation re-entry port system

It was not possible to know the cause for the shutter mechanism failure until the re-entry port was taken off the SSPX vacuum chamber. Visual inspection of the shutter mechanism revealed that its components had been repeatedly impacted by energetic plasma. Direct plasma impingement caused sputtering, melting and deformation of metal surfaces. This plasma impingement also caused erosion of ceramic surfaces in a manner analogous to the desert wind and sand eroding the nose of the Great Sphinx in Egypt. Sputtering was possibly the cause for the window being metal-coated, since sputtered particles from metal
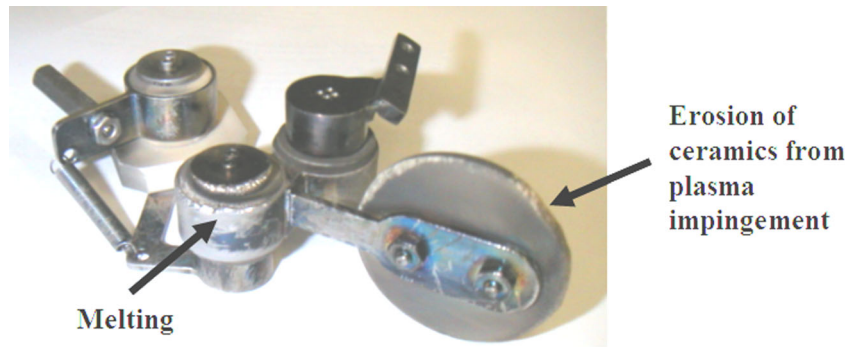
Fig. 3.4. Failure of the shutter mechanism. Melting, sputtering and erosion by direct plasma impingement caused the mechanism to get stuck.

surfaces could land anywhere, including the nearby window. Figure 3.4 shows a picture of the shutter mechanism after failure. The ceramic disk and bushings shown in the figure were white and smooth before operation in SSPX. After hundreds of plasma shots, erosion is clearly visible at the edge of the disk.

The window was salvaged and returned to excellent operation condition by carefully removing the metal coating. This was done by polishing the window with a diamond paste using a specially designed drill bit to create a rotary mini-polisher.

3.2.3   Second generation re-entry port system

It was decided to redesign the first generation re-entry port after inspection of the damaged window and shutter mechanism. A new set of design requirements was created based on the failure analysis of these components. In addition to the requirements in Table 3.1, the following specifications were made to provide a new guideline for the re-entry port system redesign:

- The shutter should be placed as far from energetic plasma as possible, while effectively protecting from gettering.

- A removable or retractable port is desirable to minimize damage from sputtering and prolong the window lifetime.

The shutter in the resulting new design was made of Macor (a machinable ceramic) and was much simpler and remained farther away from the plasma than the previous shutter. The window port was made retractable via a bellows and thus could be moved away from the plasma when not in use. The maximum stroke length of the bellows was 7 inch.

This new version of the high-speed imaging re-entry port is shown in Figure 3.5 and Figure 3.6. Three identical re-entry port systems were fabricated to take advantage of available ports in SSPX. All three ports and shutters were installed on SSPX at the same time. To the time of writing of this chapter, the ports had withstood thousands of plasma shots and are in good operating condition.

3.2.4 Electromechanical controls and interlock design

A remotely operated ball drive actuator (shown in Figure 3.6) was used to move the port into and away from the flux conserver. A special controller box was designed and built to provide power to the motor of the actuator. Three units of this controller were built, each corresponding to a different re-entry port unit. Figure 3.7 shows the assembled controller box.

To protect the window, the re-entry port was moved away from the flux conserver before the getter process was activated. This was done by manually selecting the direction of travel at the controller box. An interlock was installed between the getter controller and the re-entry port controllers to prevent damaging the window from gettering in the event that the SSPX operator forgets to retract the re-entry ports. The wiring diagram of the controller box and the interlock system is shown in Figure 3.8. Two limit switches installed
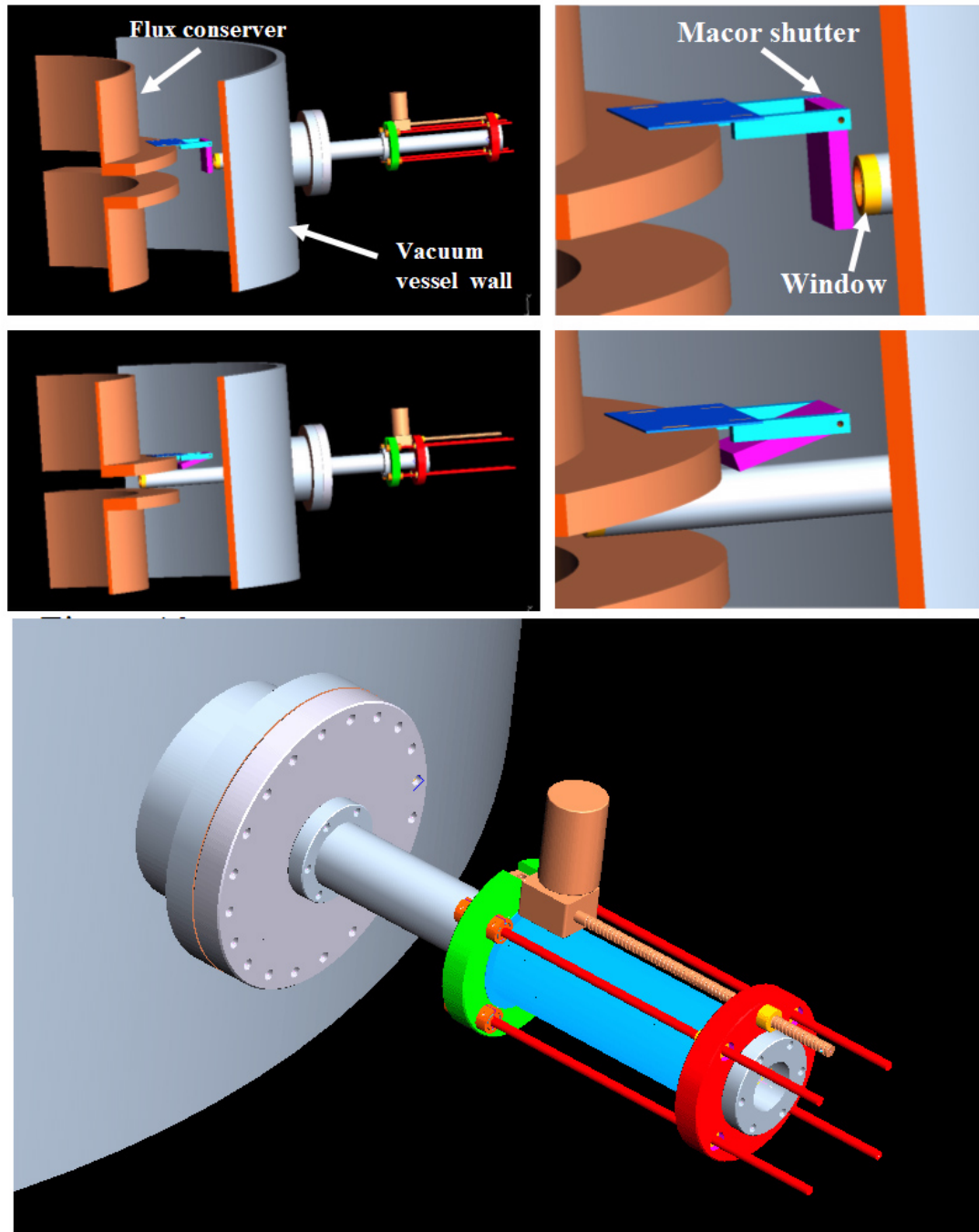
Fig. 3.5. Cuttaway view of the SSPX chamber with the second generation re-entry port. Upper images show the re-entry port retracted and the shutter protecting the window from gettering. Middle images show the port moved close to the edge of the flux conserver. Bellows not shown in these images. The lower image shows the re-entry port with the bellows, in the retracted position.

12	1	Sapphire Vieport (Mockup ISI)	9711008
11	8	Retaining ring external (stainless steel McMa	91590A122
10	1	Re-entry port for optical fiber bundle (on be	SPX-P-056
9	1	Nut for Ball drive actuator (100 lbs Mockup M	85616-NUT
8	4	Hardened precision aluminum shaft (1/4in OD -	5911K21
7	4	Frelon-lined linear bearing (mockup McMaster	5986K2
6	8	Clamp-on shaft collar (aluminum)	6157K12
5	1	Bellows-welded mockup (Huntington)	247-13
4	1	Ball drive actuator (100 lbs Mockup Motion Sy	85616
3	1	4-5/8in flange with reducer 2-3/4in for bello	SPX-P-055
2	1	4-5/8in flange with reducer 2-3/4in for bello	SPX-P-054
1	1	2.75in Nipple 6in length	SPX-P-053
Item	Qty	Name	Part #

Fig. 3.6. Exploded view of the second generation re-entry port. The part numbers starting with SPX were created for this project. The engineering drawings corresponding to those part numbers are archived with the Caltech Plasma Physics Group.
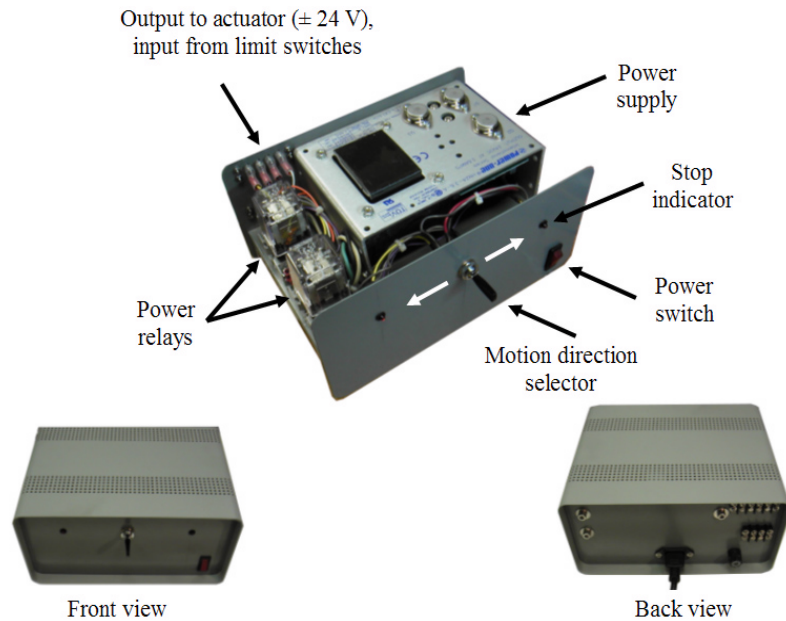
Fig. 3.7. Controller box for the ball drive actuator of the second generation re-entry port.

on the re-entry port allowed flexibility on choosing the re-entry port position close to and away from the flux conserver.

3.3 High-speed camera system

Photographing plasmas is a challenging task, because of the speed at which features change in the plasma. Typical plasma duration in spheromak experiments ranges from a few microseconds to milliseconds, with plasma light intensity and topology varying dramatically in these time ranges. Plasma features (filaments, spots, etc.) cannot be photographed with commercial film or CCD cameras because their shutters are not fast enough. Even if they were, the film or CCDs are not sensitive enough at the required short exposure times. To overcome these problems, a specialized camera is used which has light intensifiers and

Fig. 3.8. Electrical wiring diagram for the controller box of the second generation re-entry port and interlock for the SSPX getter. Courtesy of Robert Geer, LLNL.
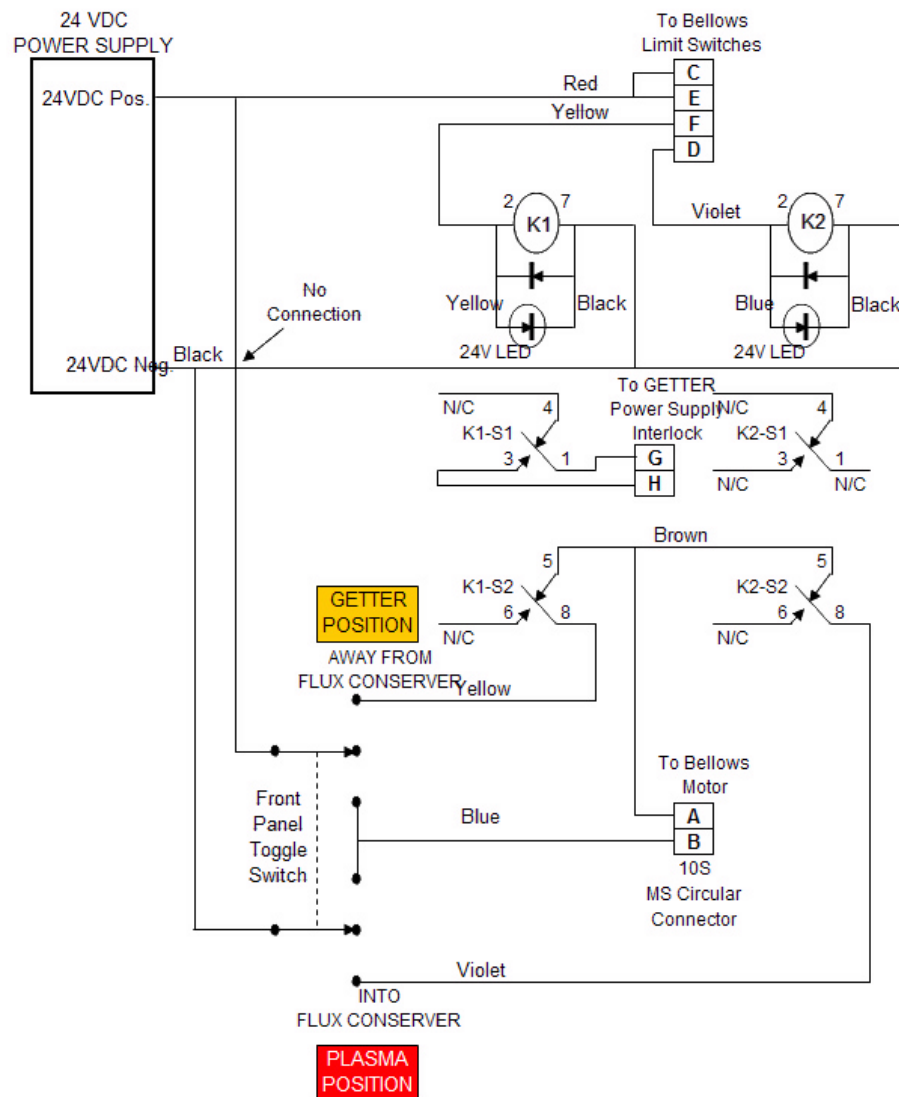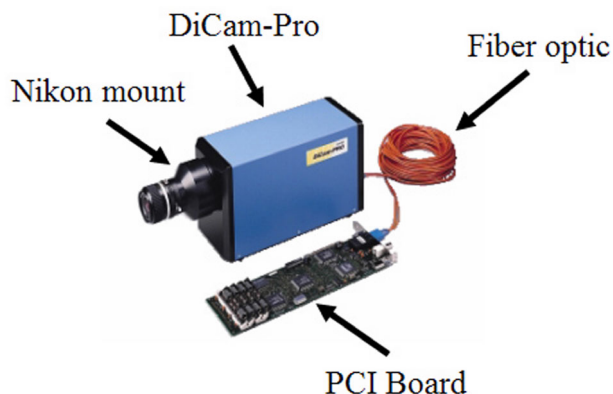
Fig. 3.9. High-speed camera used to photopraph SSPX plasmas. The dimensions of the DiCam-Pro unit are $120(W) \times 180(H) \times 340(L)$ mm. The camera was ordered with a standard Nikon lens mount. Image courtesy of The Cooke Corporation.

electronic shutters (gates) that allow nanosecond shutter speeds and photon-counting capabilities.

Experience with the spheromak plasma imaging at Caltech was helpful in choosing an appropriate camera to capture SSPX plasmas. After review of several brands and types of cameras, it was decided to use the DiCam-Pro camera from The Cooke Corporation [1]. The camera, shown in Figure 3.9, included a fiber optic cable, a PCI board installed on a computer, and the software to control the camera and process the images taken with it. The specifications for intensified CCD (or ICCD) for this camera are shown in Table 3.2.

12-bit dynamic range
Shutter down to 3 ns
Sensor resolution: 1280×1024 (VGA)
ICCD Cooled down to $-12\,°C$
2 images per shot with interframe time down to 500 ns
25 mm MCP image intensifier
Spectral sensitivity: 280 nm to 1000 nm.

Table 3.2. Specifications of the DiCam-Pro ICCD.

Operation of the camera was simple once the camera was installed at SSPX. A user needed only to turn on the power to the camera, wait about three minutes (for the electronics to be cooled down), and run the software on the system computer. The trigger for the camera was a low-voltage electronic signal that came from the SSPX gun current sensors, and thus most of the timing of the images was programmed with respect to plasma breakdown.

3.3.1 Remote control and operation of the high-speed camera

The computer used to control the DiCam-Pro had the Windows ME operating system [2]. A program called VNC [3] was installed on this operating system. This program, like many others commercially available, allows for the control of the host computer by a remote user over the Internet, as if the user was sitting in front of the host computer. The Internet connection between the SSPX control room at Livermore, and any computer at Caltech is fast enough to allow a reliable operation of VNC. Given this, it was possible to control the high-speed camera (situated at LLNL, over 300 miles away) from Caltech.

Interaction with a computer outside the LLNL's network, specially when downloading data from an experiment, required special approval from LLNL's management. Strict LLNL policies required two levels of security on the communication between computers at SSPX and Caltech. The first level was a firewall for the entire LLNL network. Authorization to allow a remote computer's IP address through the firewall was required for every session. The second level was the encryption of all communication using a program called VPN [4]. Both levels of security required a username and a one-time password (OTP)[2].

---

[2] One-time passwords, or OTPs, are passwords that contain two parts. The first one is chosen by the user and can be considered permanent (hence the name one-time). The second part is a six-digit number that randomly changes every thirty seconds. For this second part, a device given to each user (similar to a stopwatch) tells the number that is sinchronized with the main server. The user must type both parts of the password before every session.

Communication with team members at the SSPX control room was essential when operating the high-speed camera remotely. During experimental campaigns, a chat window on an Internet browser (also inside the secure connection) was used between team members at the SSPX control room and the remote user controlling the high-speed camera. The chat channel was dedicated to SSPX operations, and only authorized users could login in. All text typed through the chat channel was recorded and archived in a LLNL server.

3.4 Optics

The dimension constraints mentioned in Section 3.2 and the dimensions of the high-speed camera (see the caption of Figure 3.9) made it necessary to place the camera away from the flux conserver. However, to obtain a high angular field of view as required in Table 3.1, it was necessary to have a wide-angle lens as close as possible to the edge of the flux conserver. To bridge this gap between the lens and the camera, a relay lens was used. In the following sections, the different relay lenses used in the high-speed imaging system at SSPX are presented, including the double fiber bundle used to obtain simultaneous images from two different ports.

3.4.1 First generation relay lens

The first generation relay lens was specially designed for the first generation re-entry port (Section 3.2.1). Off-the-shelf relay lenses do exist for industrial and commercial applications. However, none of these were useful for the high-speed imaging system at SSPX. The main reason was that the outer diameter of the relay lenses was too big to fit in the re-entry port. For this reason, a specially designed relay lens had to be constructed to fit in

the re-entry ports of the high-speed imaging system. Only wide angle lenses that would fit through the small re-entry port's inner diameter (35.14 mm) could be used.

A ray tracing computer program called OLIVE [6], distributed by Edmund Industrial Optics (EOI) [7], was used to design the optical layout for the relay lens. Achromat lenses from EOI were chosen to relay the light from the wide angle lens to the high-speed camera. The distance between optical components inside the relay lens, as well as the theoretical aberrations at the image plane were calculated using OLIVE. Figure 3.10 shows the theoretical performance of the first generation relay lens calculated with OLIVE. Figure 3.11 shows the assembled relay lens. The wide angle lens used was a Computar 2.6 mm, format 1/3", CS mount (part number T2616FICS-3)[3].

All mount components of this relay lens were specially designed and fabricated at Caltech. The achromat lenses were mounted on internally threaded tubes that could be screwed on to externally threaded ones that served as extensions. Internal locking rings were used on these tubes to fix the lenses in place. External locking rings (the same diameter as the external tubes) were used to secure the distance between tubes. To focus the lens on the high-speed camera, or any other camera with a Nikon mount (or an adapter for this mount) it was only necessary to loosen the external locking rings, and thread or unthread the tubes to increase or decrease the distance between lenses.

The image quality obtained with this relay lens was limited mostly by the alignment of the tubes in which the wide angle lens and the achromat lenses were mounted. In particular, the alignment of the wide angle lens was critical to obtaining high-quality images. An image relayed through the misaligned optical system could end up blurred at the camera, or even disappear completely. If the relay lens was not centered in the re-entry port, or

---

[3]   Other commercial lenses were also used, but the computar lens was used for most of the images taken with the high-speed imaging system.

Focal plane of wide
angle lens

Focal plane
on ICCD

Achromat
(EIO 32884)

Achromat
(EIO 45214)

Double-concave
(EIO 32993)

Paraxial Data					Seidel Aberration Coefficients						DATA	
Surface	Z	Y marg.	Y chief	Radius	Lens	Sph.	Coma	Astig.	Petzv.	Dist.	Object size	3.00
Object	0.000	0.000	3.000	inf.	32884	0.0149	0.0018	0.0002	0.0001	0.0000	Image size	-11.04
1	177.444	11.153	0.097	109.160	45214	0.0002	-0.0001	0.0001	0.0001	0.0000	pMag	-3.68
2	183.444	11.193	0.030	-79.380	32993	-0.0002	-0.0002	0.0001	-0.0008	-0.0050	parx. focus	49.34
3	186.444	11.250	0.000	-226.030	Totals	0.015	0.002	0.000	-0.001	-0.005	system len.	476.30
4	220.212	11.200	-0.566	139.530							working F#	29.28
5	223.212	11.115	-0.595	-100.210							Stop Radius	11.25
6	225.712	11.077	-0.618	-291.320							Ent. Pup. Pos.	-5.90
7	424.464	0.890	-3.433	-39.780							Ent. Pup. Dia.	23.05
8	426.964	0.842	-3.548	39.780							Exit Pup. Pos.	-72.69
Image	476.302	0.000	-11.043	inf.							Exit Pup. Dia.	2.48
											FOV	0.94
											Optical Inv.	0.19

Fig. 3.10. Theoretical performance of the first generation relay lens. The paraxial data is measured at every surface where there is a transition in the refractive index (acrhomats have three surfaces).

the lens was accidentally moved against the walls of the re-entry port (or pressed strongly against the re-entry port window), then mechanical stresses would cause the entire relay lens to deform. This deformation was caused by the slight play between the threads of connecting tubes, not by individual tubes deforming, since these were fabricated from rigid aluminium.

To prevent blurred images, the lens was aligned with the port at the beginning of every shot campaign. Image centering was verified by taking images without plasma and identifying known features inside the flux conserver (e.g., the opening of the flux conserver, the posts that hold it together, or the inner electrode).
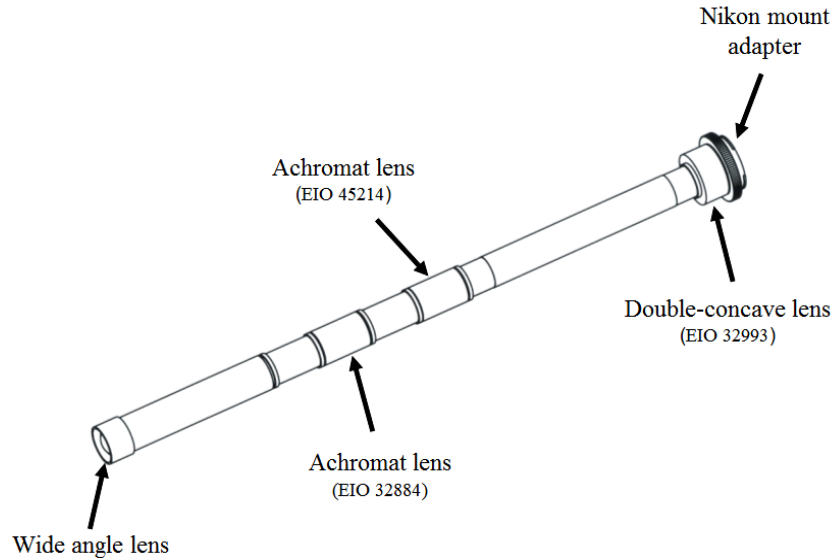
Fig. 3.11. First generation relay lens. This lens was designed to fit the first generation vacuum re-entry port. The position of the optical elements inside the tubes, and the part number of each element from EIO is indicated by arrows. The nominal length of the relay lens was 560 mm.

3.4.2   Second generation relay lens

The change in the high-speed imaging system to the second generation re-entry port (Section 3.2.3) required a relay lens with almost double the length of the first generation relay lens. Calculations using the OLIVE [6] software showed that the use of the achromat lenses from the first generation relay lens would yield images that would be too blurred to distinguish plasma features like filaments or cathode spots. Furthermore, with the availability of three different viewing ports, a relay lens that could change in length without loss in performance was desired. Even though the second generation re-entry ports were identical, equipment from other diagnostics near each of the three re-entry ports imposed different constraints on the space available for the high-speed imaging system. Therefore, a completely new relay lens design was necessary.

Experience with the first generation relay lens was useful in designing the second generation one. A schematic of the design[4], as well as the theoretical performance of the achromat pair (calculated using OLIVE), is shown in Figure 3.12. This design has several advantages with respect to its predecessor. In the previous design, to focus the lens it was necessary to adjust two or three tubes in the lens; a process that could be time-consuming.

Focusing was much faster with the second generation design because different elements could be adjusted independently. The adjustment of the wide angle lens was done by looking directly at the image formed on the wider side of the fiber taper. The distance between the fiber taper and the first achromat lens could also be checked independently since the image formed after the achromat is focused at infinity (rays are collimated, that is, parallel to the optical axis). Varying the distance of the projection plane (in a dark room, for example) should not change the image if the first achromat is at the focal distance from the fiber taper. For this reason, the distance between achromats (labeled χ in Figure 3.12) could be arbitrarily varied without affecting the image at the focal plane of the system.

Another advantage of having collimated light between the achromats was that interference filters[5] could be placed between those two lenses without affecting the focusing of the lens. A picture of the assembled second generation relay lens is shown in Figure 3.13. From all the optical systems used in the high-speed imaging system, this relay lens had the best resolution.

3.4.3 Double-branch coherent optical fiber bundle

The availability of three different optical viewports in SSPX opened the possibility of obtaining plasma images simultaneously from different angles. To do this, the first idea con-

---

[4] There is a patent pending by C. A. Romero-Talamás and P. M. Bellan on this relay lens design.

[5] Interference filters require collimated light and perpendicular to their surface to operate optimally [8].

Focal plane of wide angle lens

χ

Focal plane on ICCD

Fiber taper (EIO 55135)

Achromat (EIO 32494)

Achromat (EIO 45414)

Paraxial Data					Seidel Aberration Coefficients						DATA	
Surface	Z	Y marg.	Y chief	Radius	Lens	Sph.	Coma	Astig.	Petzv.	Dist.	Object size	9.00
Object	0.000	0.000	9.000	inf.	32494	0.0006	-0.0007	0.0037	0.0022	-0.0154	Image size	-16.52
1	145.958	10.944	14.722	197.710	45414	0.0001	-0.0001	0.0016	0.0012	0.0001	pMag	-1.84
2	148.158	10.993	14.708	66.210	Totals	0.001	-0.001	0.005	0.003	-0.015	parx. focus	271.94
3	153.858	11.232	14.797	-91.370							system len.	679.98
4	400.546	11.250	0.000	171.030							working F#	12.24
5	405.546	11.138	-0.198	-121.540							Stop Radius	11.25
6	408.046	11.109	-0.288	-352.460							Ent. Pup. Pos.	375.53
Image	679.983	0.000	-16.519	inf.							Ent. Pup. Dia.	-34.43
											Exit Pup. Pos.	-276.76
											Exit Pup. Dia.	22.61
											FOV	-2.25
											Optical Inv.	0.67

Fig. 3.12. Theoretical performance of the second generation relay lens. Calculations with the OLIVE softare start at the right of the fiber taper. The paraxial data is measured at every surface where there is a transition in the refractive index (acrhomats have three surfaces).

sidered was to simply purchase more high-speed cameras. This idea was quickly discarded because of the high-cost of the cameras. Instead, a double-branch fiber bundle was designed such that it could be used with the existing high-speed camera. Two bundles of coherently arranged optical fibers (that is, the matrix position of each fiber, or pixel, is the same on both ends of each bundle) were fused together on a single end. The double image obtained on the single end was relayed to the high-speed camera, where the two images were captured as a single image. The two images were then digitally separated and stored using simple computer routines.
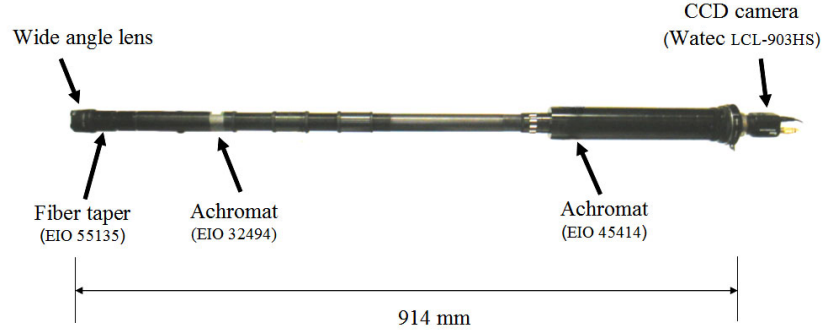
Fig. 3.13. Second generation relay lens. A monochromatic CCD camera was used to test the performance of the relay lens. Nominal length of this optical system: 914 mm.

The double-branch optical fiber bundle was designed at Caltech, and commissioned to Schott Optics [9] for fabrication. The finished product is shown in Figure 3.14. The characteristics of the double-branch fiber bundle are listed in Table 3.3.

Length of each branch: 4.5 m
Resolution: 50 lines/mm
Optical area of each bundle: 6×6 mm^2
Bundle rotation: $360°$
Bend radius: 4 inch
Maximum temperature: 120 °C

Table 3.3. Double-branch optical fiber bundle characteristics.

The double-branch fiber bundle had some advantages and disadvantages with respect to the first and second generation relay lenses. Besides the obvious advantage of simultaneously obtaining images from two different ports, the length and flexibility of the bundles was very convenient. Once the single end was mounted on the camera, the bundles could be routed around the chamber and inserted into different ports without the need of alignment. The camera did not need to remain close to the ports, or even be mounted on a tripod. Furthermore, the flexible stainless steel conduit (covered with shrink tube for electrical in-

Fig. 3.14. Double-branch, coherent optical fiber bundle. Left: full view of the coherent bundles. Center: close-up of the cladding of both branches. Right: using a magnifying lens, two distinct images of the same object (a photographic camera) are seen at the common end of both fiber branches.

sulation) that protects the optical fibers was sturdy enough that no special care was needed when handing the bundles.

The disadvantage of the double-branch fiber bundle with respect to the relay lenses was the decrease in resolution. Having two images in the same ICCD meant the resolution was at best half of that of the relay lenses. Stray light was also a problem. During the fabrication of the fiber bundles, the optical fibers for a given branch were arranged in non-coherent subgroups that formed one pixel. Those subgroups were bundled and glued together on both ends of the fiber, and formed the coherent matrix that displayed the images. It was possible that non coherent light 'leaked' through the space between pixels. This unwanted light increased the noise and the blurriness in the images captured by the camera. This negative aspect of the double-branch fiber bundle made it unfit for plasma images during sustainment of the SSPX discharge because the signal-to-noise ratio in the images was too low. Nevertheless, images taken during the formation phase with the fiber bundles were acceptable because features were bright, and thus the signal-to-noise ratio was high.

Image at fiber
bundle end

Focal plane
on ICCD

Achromat
(EIO 32724)

Achromat
(EIO 32494)

Paraxial Data					Seidel Aberration Coefficients						DATA	
Surface	Z	Y marg.	Y chief	Radius	Lens	Sph.	Coma	Astig.	Petzv.	Dist.	Object size	6.70
Object	0.000	0.000	6.700	inf.	32724	0.0338	-0.0228	0.0261	0.0174	-0.0006	Image size	-16.68
1	52.230	9.790	0.779	1029.790	32494	0.0006	-0.0002	0.0101	0.0076	0.0019	pMag	-2.49
2	54.630	10.041	0.621	29.950	Totals	0.034	-0.023	0.036	0.025	0.001	parx. focus	145.55
3	63.630	11.250	0.000	-31.940							system len.	220.11
4	66.656	11.249	-0.338	91.370							working F#	6.64
5	72.356	11.009	-0.750	-66.210							Stop Radius	11.25
6	74.556	10.959	-0.897	-197.710							Ent. Pup. Pos.	-6.87
Image	220.107	0.000	-16.679	inf.							Ent. Pup. Dia.	22.16
											Exit Pup. Pos.	-153.82
											Exit Pup. Dia.	23.16
											FOV	6.47
											Optical Inv.	1.26

Fig. 3.15. Theoretical performance of the double fiber bundle relay lens.

3.4.4 Relay lens for the double-branch fiber bundle

A relay lens was required to convey the images formed at the single end of the double-branch fiber bundle to the high-speed camera. In this case there were no constraints on the length or size of the relay lens since the high-speed camera could be placed away from the ports or other equipment around the SSPX chamber. These lenses can actually be purchased from a number of manufacturers. However, off-the-shelf relay lenses for fiber bundles usually have no magnification in the image. To maximize the use of the ICCD area in the high-speed camera, we decided to design and build a relay lens with a magnification power of 2.5. The theoretical performance of the resulting relay lens is shown in Figure 3.15. A picture of the assembled lens taken during a test at Caltech is shown in Figure 3.16.
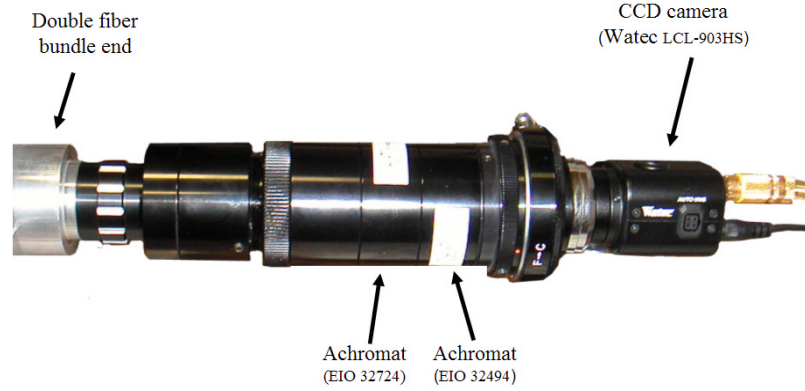
Fig. 3.16. Relay lens for the double fiber bundle.

3.5 Magnetic shield for the high-speed camera

Representatives from the Cooke Corporation [1] recommended that the DiCam-Pro high-speed camera should not be exposed to magnetic fields stronger than[6] 5×10^{-4} T. The stronger fields expected at midplane, near the SSPX vacuum chamber wall where the high-speed camera was located, were approximately 3×10^{-2} T [5] (when all the bias coils were used in BCS configuration; see Chapter 2). Therefore, an attenuation of 100 was required for the strongest magnetic field near the high-speed camera.

The materials selected to build the magnetic shield were galvanized steel and a high magnetic permeability material called mu-metal. The mu-metal was purchased from a company called The MμShield Company [10]. This company also provided technical support to design a shield with the dimensions and attenuation required for the high-speed camera. The formula they recommended for the shield calculations was

$$A = \frac{\mu t}{d} \tag{3.1}$$

---

[6] The reason given was that it could damage some of the trigger electronics.

48
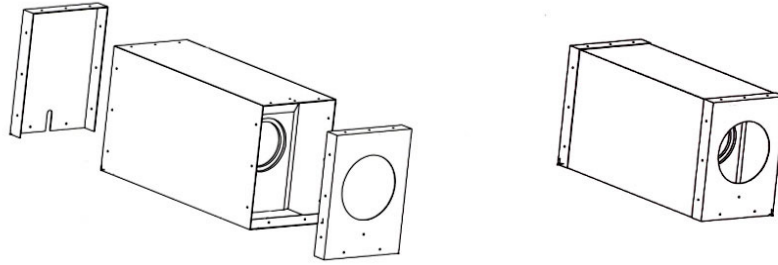
Fig. 3.17. Magnetic shield. Left: exploded view. The DiCam-Pro is seen inside (without the Nikon mount adapter). Right: Assembled magnetic shield. The dimensions of the shield are $200\,\mathrm{mm} \times 225\,\mathrm{mm} \times 475\,\mathrm{mm}$.

where A is the desired attenuation, d is the shield diameter (the longest side, in a rectangular cross-section), μ is the permeability, and t is the mu-metal thickness. A mu-metal thickness of $1.02\,\mathrm{mm}$ was chosen. For this thickness, the MμShield support engineers determined that the permeability of the mu-metal immersed in a 5×10^{-4} T non-oscillating field would be about 10×10^3. A shield diameter of $225\,\mathrm{mm}$ was chosen based on the dimensions of the high-speed camera enclosure. For these numbers, an attenuation factor of about 45 is obtained.

The shield was built and tested using large pancake coils[7] (approximately 70 cm in diameter). The magnetic field without the shield near the pancake coil was measured to be 2.8×10^{-2} T. To achieve a field inside the shield of 2.8×10^{-4} T (i.e., an attenuation of $A = 100$), layers of galvanized steel (separated by layers of plastic) were added to the inside of the shield until the required attenuation was reached. The finished magnetic shield is shown in Figure 3.17.

---

[7] These coils are used in the Plasma Waves experiment of the APh77 course at Caltech.

3.6 Camera mounts and supports

The field of view of the high-speed imaging system was very sensitive to the distance between the wide angle lens and the re-entry port window. To obtain the maximum field of view, it was desired to have the wide angle lens as close to the re-entry port window as possible. For this reason, sliding plates were specially designed and built to achieve millimetric precision in the positioning of the lens near the window. The plates are shown in Figure 3.18.

With the first generation re-entry port, the use of the plates was as follows. The lower plate (labeled 3 in the exploded view) was bolted to a heavy duty tripod head (Bogen, model 3057). The high-speed camera inside the magnetic shield was bolted onto the upper plate (labeled 4, with the screws labeled 2). The two plates could slide smoothly even when the camera was mounted on them. Once the lens was set at the desired distance from the window, the two plates were secured using four bolts (labeled 1). The camera tripod (Bogen, model 3036) was bolted to the floor to prevent movement of the camera if accidentally hit during service to nearby SSPX diagnostics. The camera mounted on the plates and the tripod is shown in Figure 3.19.

The sliding mechanism was modified for use with the second generation re-entry ports. The moving re-entry port required the upper plate to be connected to the re-entry port, such that the camera could move in and out, and the relay lens would remain fixed with respect to the port window. Sliding rails with ball bearings were adapted to fit between the plates, and thus allow a very smooth sliding of the camera when the re-entry port was moved. This was done to prevent overheating the ball drive actuator (shown in Figure 3.6).
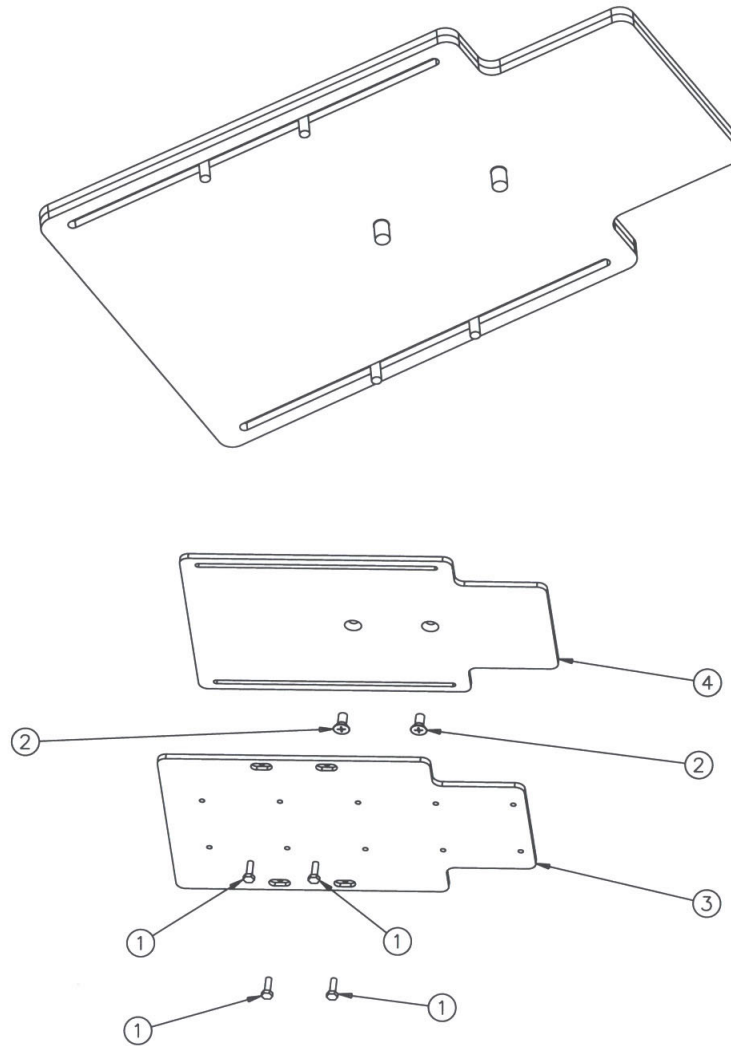
4	1	Tripod head mount plate	SPX-P-041
3	1	Tripod camera mount plate	SPX-P-040
2	2	Screw flat head 3/8 x 0.5in (mockup)	
1	4	Brass cap screw 1/4-20 x 3/4in (mockup)	
Item	Qty	Name	Part #

Fig. 3.18. Camera mount plates.
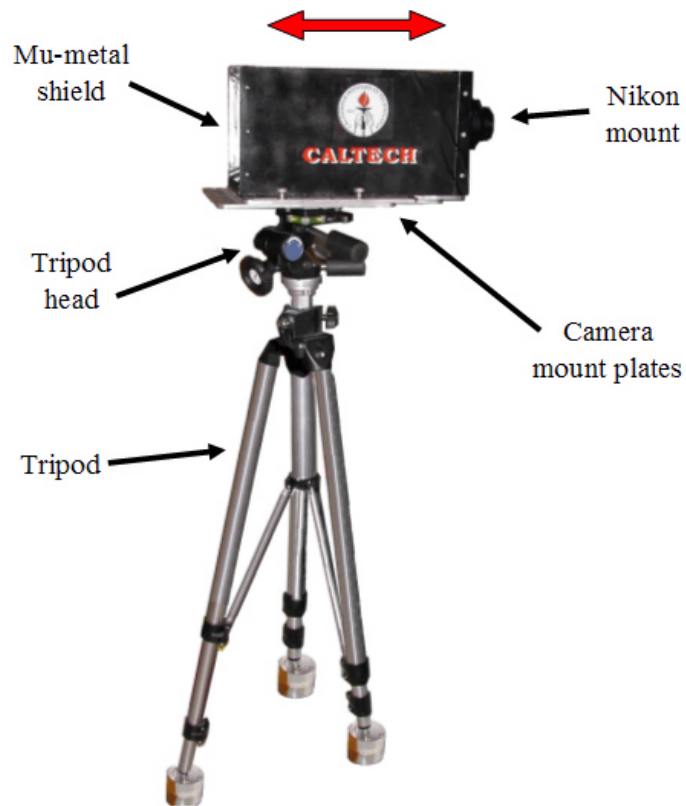
Fig. 3.19. Camera (inside mu-metal shield) mounted on sliding plates and tripod. The sliding direction allowed by the camera mount plates is indicated by the arrow on top.

3.7 References

[1]   The Cooke Corporation, http://www.cookecorp.com/. July 30, 2004.

[2]   Microsoft Windows ME, http://www.microsoft.com/WindowsMe/. July 30, 2004.

[3]   RealVNC Ltd., http://www.realvnc.com/. July 31, 2004.

[4]   Cisco Systems VPN, http://www.cisco.com/en/US/products/hw/vpndevc/index.html. August 1, 2004.

[5]   S. Woodruff. Personal communication. June, 2001.

[6]   High Chiva, http://www.highchiva.com/OLIVE.htm. August 1, 2004.

[7]   Edmund Industrial Optics, http://www.edmundoptics.com/. August 1, 2004.

[8]   Edmund Industrial Optics, 2001 Optics and optical instruments catalog N011B, pp. 71 - 73.

[9]   Schott Optics, http://www.us.schott.com/. August 5, 2004.

[10]   The MμShield Company, Inc., http://www.mushield.com/. August 5, 2004.

Chapter 4

Identification of plasma stages in SSPX using high-speed imaging

4.1 Introduction

Images of the Sustained Spheromak Physics Experiment (SSPX) plasma were obtained during thousands of experimental shots. These images were taken at various times during the shots (typical shot duration 4 ms) and revealed characteristics in the plasma that were common to most shots, even though the conditions of the shots were varied according to the purpose of each experimental campaign. These characteristics can be grouped in three stages, depending on the discharge time at which the images were taken. The first stage is the breakdown and plasma ejection from the gun into the flux conserver region. The second stage is the gun current sustainment. The third stage is the gun current decay. These stages are indicated on a typical gun current trace in Figure 4.1.

Description of these stages, along with the typical images during those stages, are presented in the sections below. For reference, the view of the flux conserver (without plasma), as seen through the relay lens and the high-speed camera, is shown in Figure 4.2. The horizontal field of view inside the flux conserver is almost 1 meter, limited only by the window edge in the re-entry port and the edges of the flux conserver opening at midplane. The vertical field of view is more than 0.5 meters.

Most of the images shown below were taken from hydrogen plasmas. Only some of the images taken during the breakdown and ejection stage correspond to helium shots.
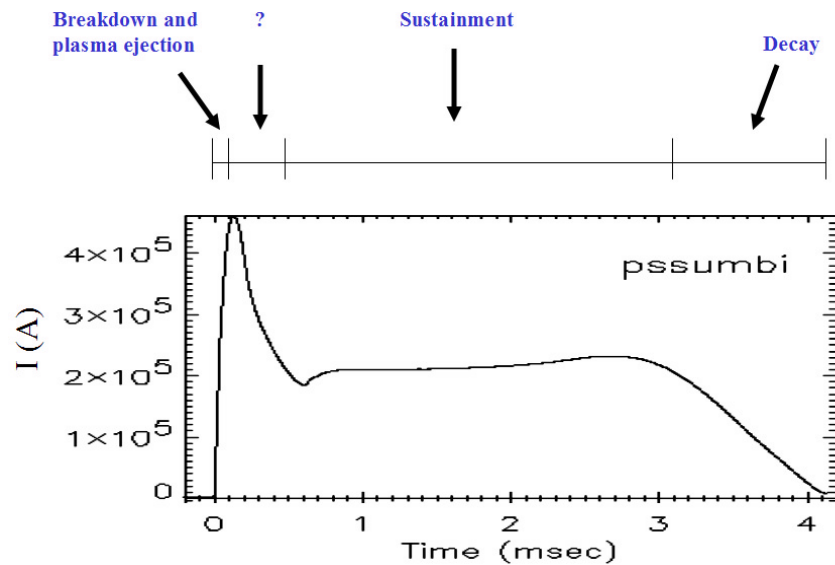
Fig. 4.1. Plasma stages at SSPX. The three stages used to identify plasma images are shown above a typical gun current trace. In the time range indicated with a question mark (?) no features can be seen because the plasma is either 'burned out', that is, no light in the visible range comes out of the plasma, or there is bright plasma too close to the window (analogous to dense fog covering the windshield of a car). The initial and final times of each stage is approximate.
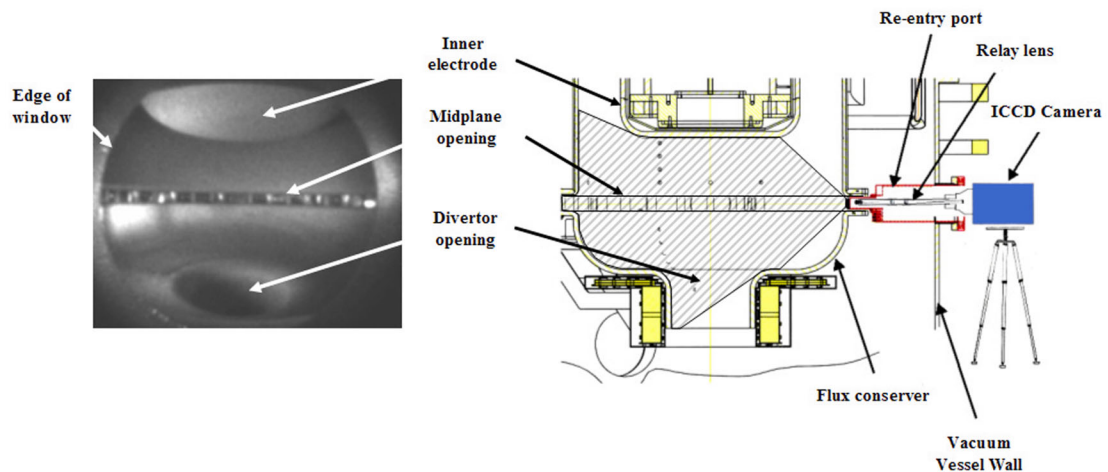
Fig. 4.2. Interior view of the flux conserver as seen through the relay lens and the DiCam-Pro high-speed camera. The shaded area on the diagram on the right corresponds to the field of view of the camera.

Images from these shots show features that are similar to those in hydrogen shots, but are brighter and move slightly slower (probably because helium is heavier than hydrogen). Color was added to all images, using a special program compiled with the software called IDL [1], to illustrate light intensity levels.

4.2 Breakdown and plasma ejection

In this stage the plasma typically breaks down in the gun region, outside the field of view of the camera. Breakdown time is considered $t = 0$ for all the images presented below. After breakdown, $\mathbf{J} \times \mathbf{B}$ forces rotate and push the plasma into the flux conserver region. As the plasma travels into the flux conserver, it drags and deforms the magnetic field. This process is shown in Figure 4.3. Initially, only the bias field is present in the vacuum chamber, and is constant in time. A gas is then puffed in the gun region and after some time the high voltage switch is closed to initiate the breakdown. A detailed description of what has been observed during this stage with the high-speed camera now follows.

In a few tens of microseconds after breakdown, the plasma enters the field of view of the high-speed camera, as seen on the left image in Figure 4.4. Just a few microseconds later, as the plasma continues traveling along the axis of the gun, some structure can be observed (right image in Figure 4.4). The structure typically observed resembles descending theater curtains due to its undulations. At this stage, the expansion speed of these 'curtains' into the flux conserver region is in the order of 50 km/s. As the plasma continues filling the rest of the flux conserver, the undulations merge to form a more uniform expansion front. This merging is partly caused by the plasma rotating around the axis of the gun.

The plasma expansion into the flux conserver is inherently three-dimensional since the plasma moves radially (inwards), toroidally, and axially, as it balloons into the flux
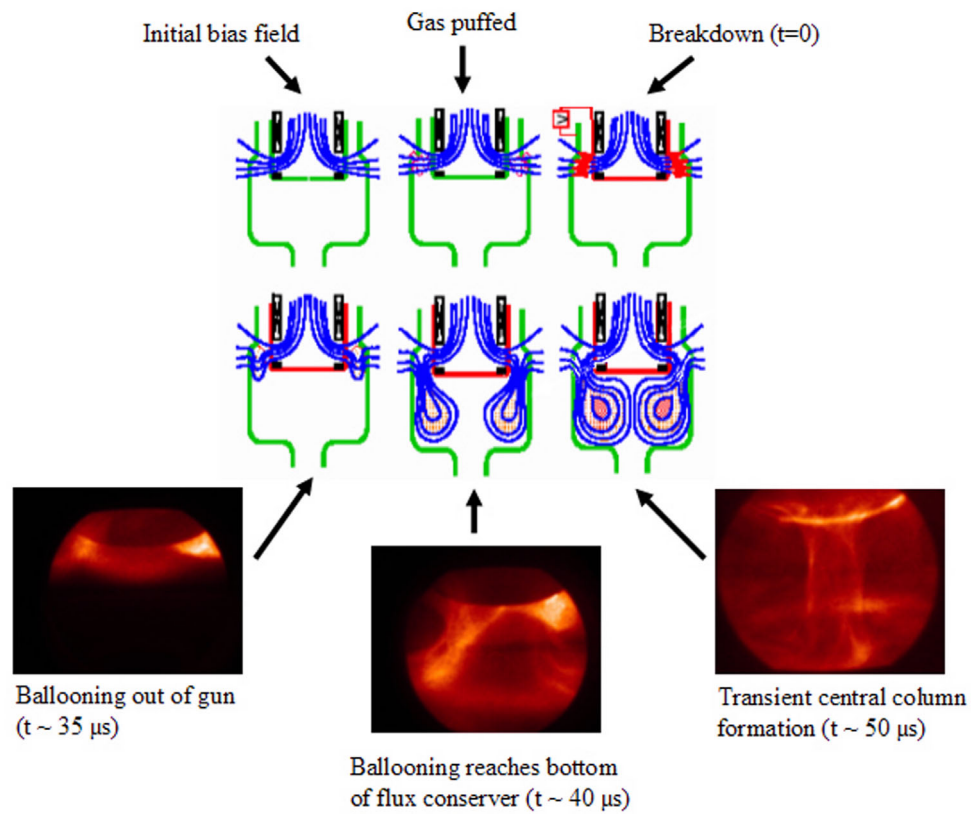
Fig. 4.3. Deformation of magnetic flux surfaces during the breakdown and ejection stage.
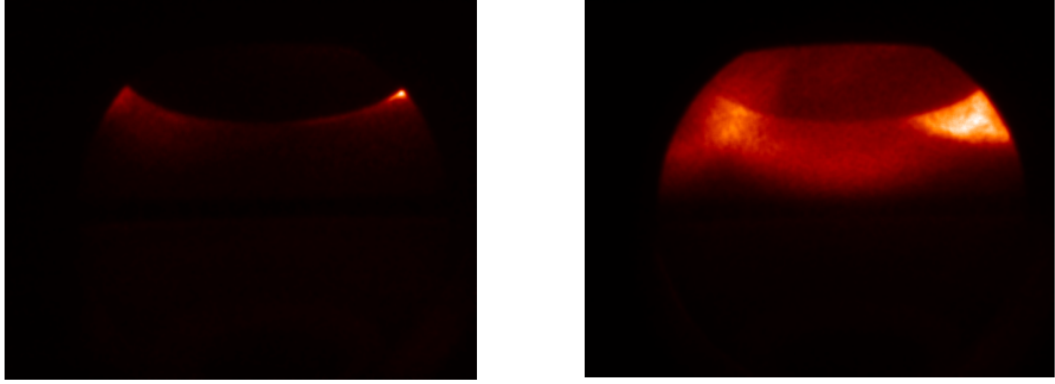
Fig. 4.4. Shot 8045. Left image: $t = 30\ \mu s$. Right image: $t = 35\ \mu s$. Gas used: hydrogen.

conserver. This ballooning can be interpreted as a helicoidal expansion plus a radial pinch towards the axis of the gun. The helicoidal part of the motion describes a 'barber pole' trajectory around the inner electrode. An example of this 'barber pole' motion is shown in Figure 4.5. A bright spot (indicated with an arrow) is identified on the left image. After five microseconds, the bright spot moved toroidally almost as much as it has traveled along the axis of the gun. Note that some filaments are visible on the image on the right, probably created in the gun region. There is evidence of filamentation in the gun region from the scratches left by filaments that travel down the gun region. This instability in SSPX has been studied extensively by Ryutov et al. [4].

It should be noted that in the images obtained at this stage, the distance traveled by the spot in the radial direction cannot be discerned from the high-speed images (which, after all, are two-dimensional projections[1]). However, images like those shown in Figure 4.6, taken at later times, suggest that at this stage the plasma moves much faster helicoidally (describing the 'barber pole' motion) than radially. In these images the expansion front

---

[1] The double-brach fiber bundle, which could have helped in making three-dimensional measurements, was not used for this purpose because the resolution was not high enough to measure translation of small or fine features in the plasma.
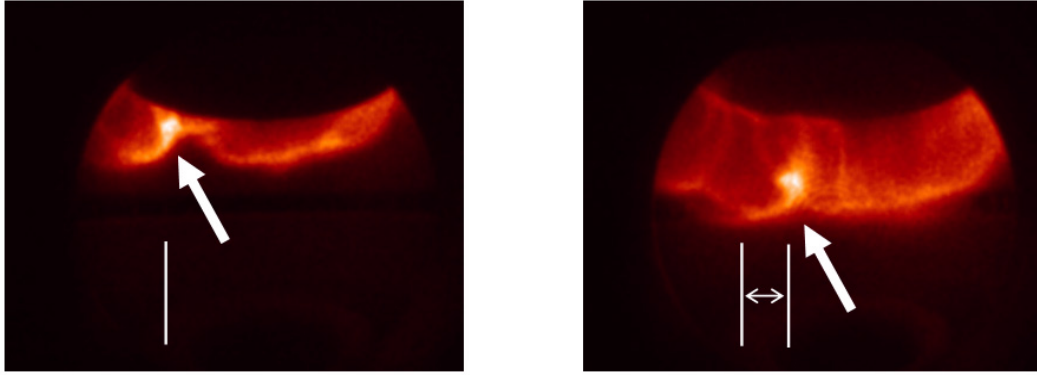
Fig. 4.5. Shot 8036. Left image: $t = 30 \ \mu s$. Right image: $t = 35 \ \mu s$. Gas used: hydrogen. Arrows indicate the change in position of the bright spot seen on both images.

reaches the bottom of the flux conserver (about 50 cm traveled from the edge of the electrode) faster than it reaches the center of the inner electrode (about 25 cm away from the edge). In fact, plasma stagnates at the bottom of the flux conserver before reaching the center of the electrode, and a central column becomes more apparent. This is shown in Figure 4.6. We refer to this column as the transient central column, because it is very short-lived, as it will be shown below.

Filamentation along the transient central column is sometimes visible. These filaments are probably the evolution of filaments observed at earlier times, like those in Figure 4.5. Figure 4.6, for example, shows filaments in the left side of both images. The filaments seem to be 'stretching' along with the plasma.

As time progresses, the diameter of the central column decreases and the overall intensity of light emitted is diminished. This is possibly due to a higher ionization percentage of the gas, as seen in Figure 4.7.

It has been observed in some images that plasma rotates around the central column. Shown in Figure 4.8 are two images of the same shot, only $3 \ \mu s$ apart. In the lower half
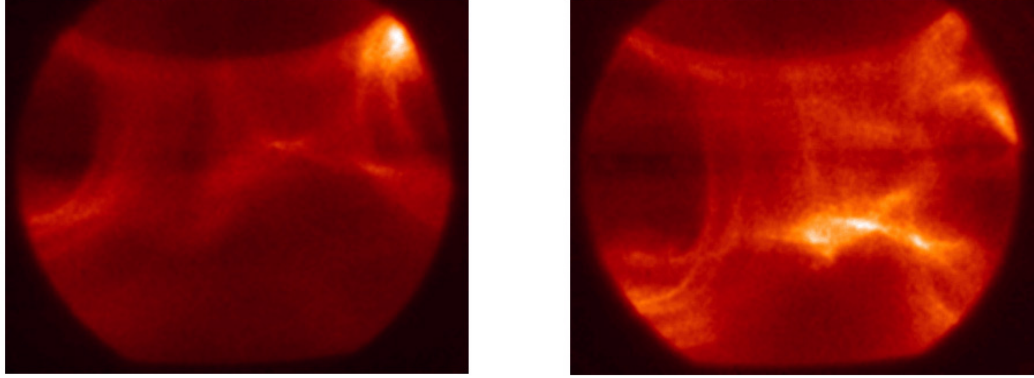
Fig. 4.6. Shot 8162. Left image: $t = 50$ μs. Right image: $t = 53$ μs. Gas used: hydrogen.

of these images, a filament seems to wrap around the column, extending from close to the bottom of the flux conserver, to almost midplane. This elongation suggests that plasma moves helicoidally around the central column. From the right image in Figure 4.8, the pitch angle of this helicoid is estimated to be about $20\,^{\circ}$.

The transient central column bends impulsively just a few microseconds after it began forming (hence the name 'transient'). Figure 4.9 shows a very faint column on the left image. This column seems to have vanished (right image) just after five microseconds. The current from the gun, however, continues to increase uninterrupted (just like in Figure 4.1). The apparent vanishing of the central column is probably caused by a very high degree of ionization, such that no light is emitted by the plasma (for the case of hydrogen) or light is emitted outside the wavelength range of the high-speed camera (for the case of helium or impurities).

Capturing impulsive changes of the transient central column proved to be very challenging. Although many images were obtained to get more details of this process, none showed more detail than that shown in Figure 4.9, even when decreasing the time between images to less than one microsecond. How the plasma rearranges itself shortly after the
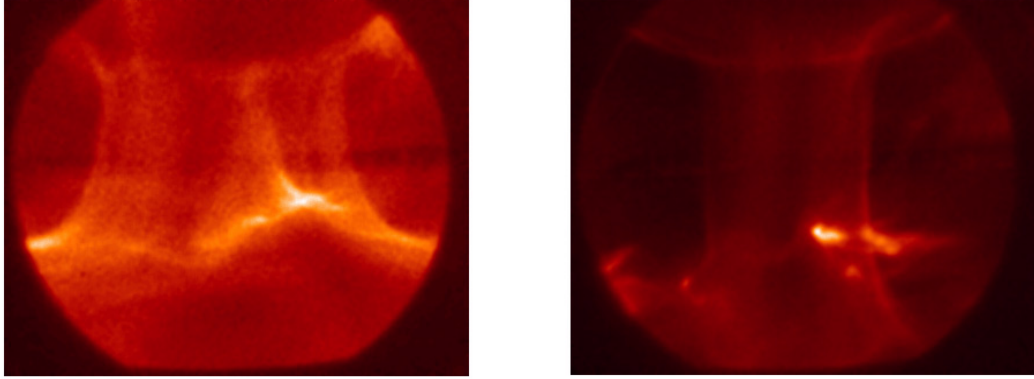
Fig. 4.7. Shot 8200. Left image: $t = 50 \ \mu s$. Right image: $t = 55 \ \mu s$. Gas used: hydrogen.

transient column bends, continues to be a mystery since the gun current flows uninter-rupted. However, it is conjectured that this impulsive bending precedes a reconnection event that leads to flux amplification [2]. Namely, the transfer of toroidal flux (azimuthal to the chamber axis) to poloidal magnetic flux (the transient central column). At a meeting of the Innovative Confinement Concepts group (May 2004), Bellan proposed a topological constraint of two full turns in a flux rope (or column in our case) for flux to be amplified and helicity be conserved in the time scale of the reconnection event. This two-turn constraint applied to SSPX is shown in Figure 4.10. If only one turn occurs before reconnection, then the helicity content would increase discontinuously (i.e., a stepwise jump)[2]. Ongoing research at SSPX is expected to provide further insight into this important physical process.

After the bending event, there is a black out time for the high-speed camera, since no imaging was possible during those times. This black out time is indicated with a question mark (?) in Figure 4.1. Imaging of the plasma during this time could perhaps be done with other gases (used as tracers and injected at selected times) to maximize the light emitted

---

[2]   More details on the geometric interpretation of helicity can be found in Reference [3].
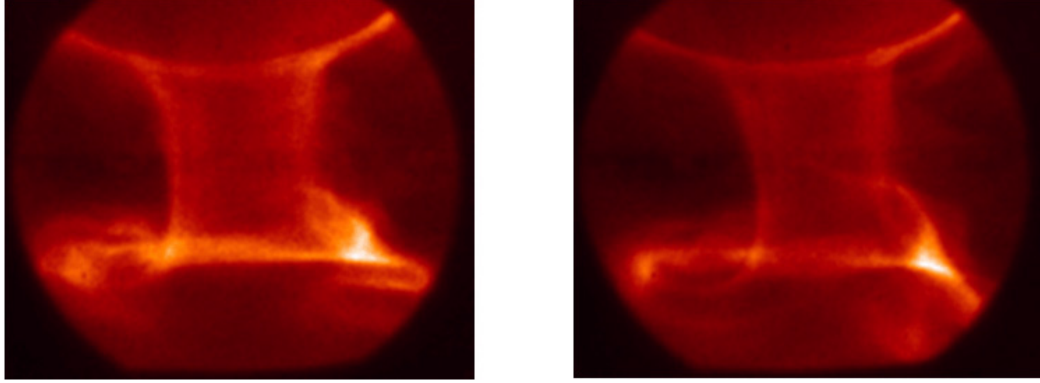
Fig. 4.8. Shot 8164. The times of these images are, with respect to breakdown: $t = 70\ \mu s$ (left) and $t = 73\ \mu s$. The gas used on this shot was helium. For this gas, plasma moves slower than hydrogen. However, the evolution of the plasma is the same as with hyrdrogen.

from the plasma features during small periods of time. However, this approach was not attempted in the present work.

4.3 Sustainment

Plasma continues to be mostly ionized by the time gun current sustainment is achieved (flat portion of the curve in Figure 4.1). There are, however, some characteristic features seen in high-speed images taken during this stage. Two of these characteristics are present throughout sustainment. The first characteristic is the formation of a faint central column that is much more stable (in time) than the column described in the previous section. We call this column the sustainment central column. The second characteristic is the spot and pattern formation in the electrodes. Of most interest are the patterns formed on the end surface of the cylindrically shaped cathode (inner electrode), which evolve in time and appear to be related to plasma drifts.
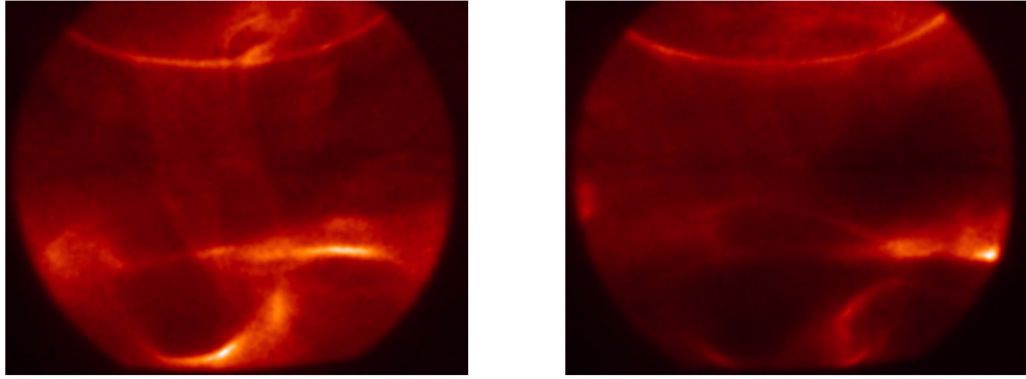
Fig. 4.9. Shot 8175. Left image: $t = 80\ \mu s$. Right image: $t = 85\ \mu s$. Gas used: helium.

Images of these two characteristics during the sustainment stage are presented below. However, details and measurements of the sustainment central column are presented in Chapter 5, and details of the patterns formed on the electrodes, their drifts, and the implications they have on the current profile, are presented in Chapter 6.

Early in this stage there are no cathode patterns or indications of a central column. As mentioned earlier, a plasma column (or other features) could be there, but the plasma either does not emit light, or it does not emit it in the visible range of the high-speed camera. Only some bright spots at the flux conserver midplane can be seen, probably caused by wall recycling and plasma impingement on the posts that hold the flux conserver together (see Chapter 2 for diagrams of the SSPX flux conserver). Sometimes, there is also a bright glow at the edge of the cathode, as shown in Figure 4.11. Spot appearance at the midplane could last tens to hundreds of microseconds, but their position and intensity could vary in just a few microseconds.

The bright spots at the midplane eventually disappear. Shortly after that, spots on the inner electrode start to appear. Figure 4.12 shows two spots that formed at the surface of the electrode. The figure also shows a faint boundary on the left image (arrow above
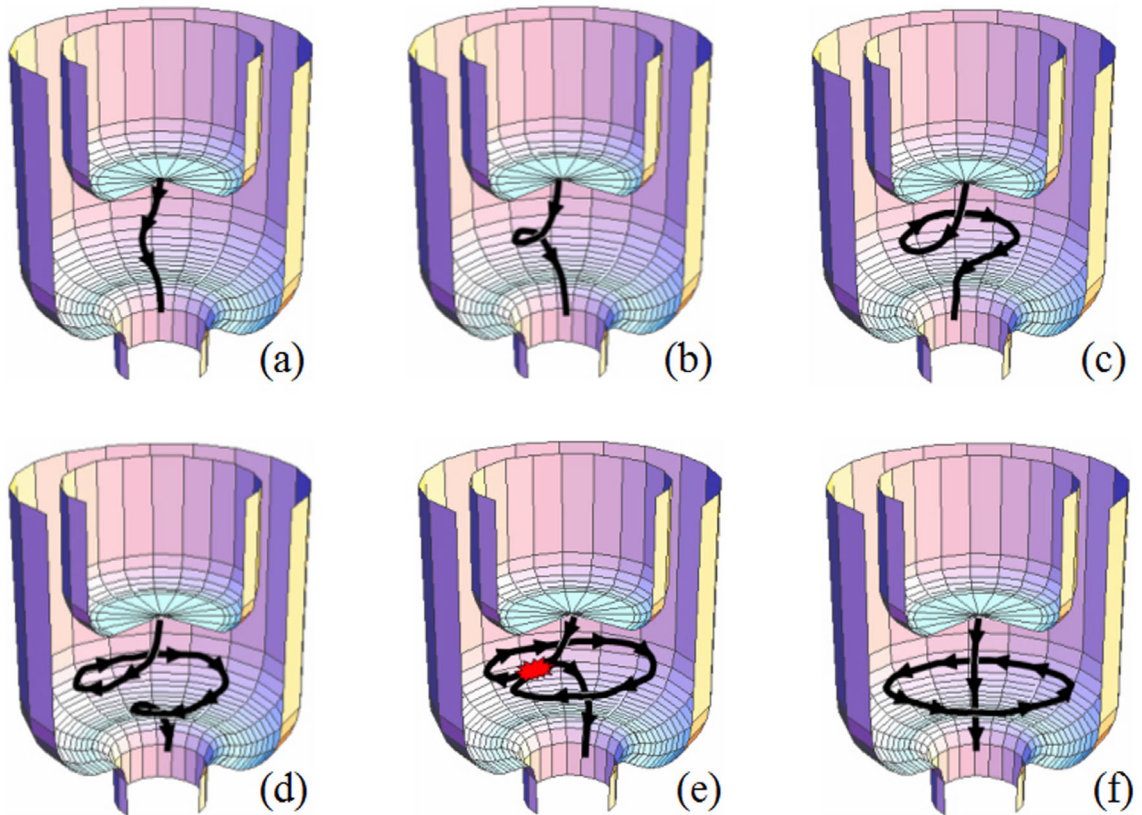
Fig. 4.10. Bending of the transient central column, and the two-turn constraint for flux amplification. The images on Figure 4.9 correspond to somewhere between frames (a) and (c). The red area in frame (e) shows where reconnection occurs, resulting in a flux rope linked as in frame (f).
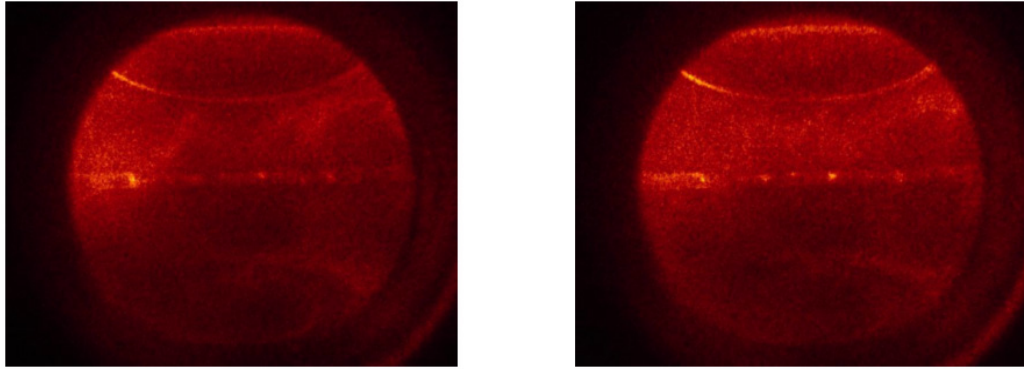
Fig. 4.11. Shot 9038. Left image: $t = 520 \ \mu s$. Right image: $t = 525 \ \mu s$. Gas used: hydrogen.

midplane), which could indicate the presence of the sustainment central column or a wide current sheet. Other images taken under similar conditions showed how the spots varied rapidly in intensity (in just a few microseconds), but not in their location on the cathode surface. These spots seemed to have served as footpoints for the patterns that appeared and evolved during the sustainment stage.

The spots grow in number over time-scales of tens to hundreds of microseconds. At the same time, patterns start to elongate from these spots. The elongation could be over hundreds of microseconds and extend over centimeters on the cathode surface. It was observed in some images that two or more different patterns could merge or intersect each other, sometimes forming a single and longer pattern. Figure 4.13 shows an example of the appearance of these patterns during the sustainment stage. Notice how the pattern indicated on the upper part of both images elongated considerably over two hundred microseconds. The detailed behavior of these patterns during the sustainment stage is discussed in Chapter 6.

Indicated also in Figure 4.13 are the boundaries of what was identified as the sustainment central column. This central column differs from the transient central column
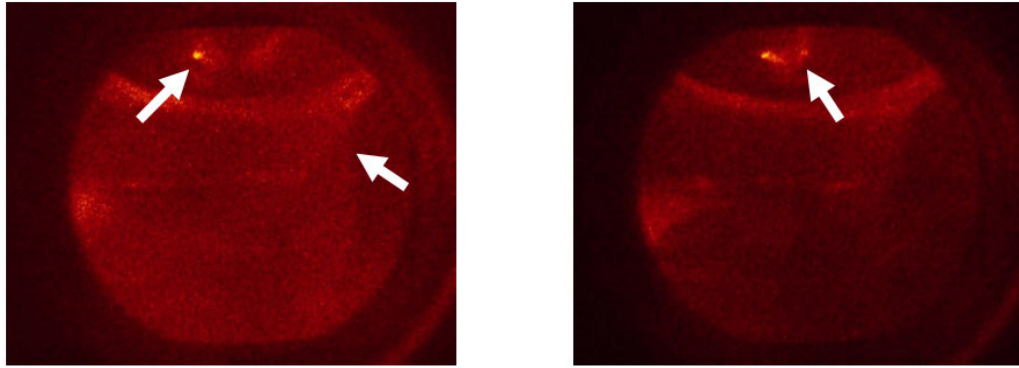
Fig. 4.12. Shot 9024. Left image: $t = 740$ μs. Right image: $t = 745$ μs. Gas used: hydrogen. Arrows indicate initial spot formation on the cathode, and the appearance of a faint boundary that could indicate the presence of a plasma column or sheet.

(Section 4.2) in its lifetime. The sustainment central column survives much longer than the transient column. Measurements of the column diameter during the sustainment stage are presented in Chapter 5.

Interframe times of a few microseconds to hundreds of microseconds (in increments of tens of microseconds and shutter times of a few microseconds) were used to study the behavior of the sustainment central column. It was found that this column does not move or bend significantly (like the transient central column) during the sustainment stage. The intensity of the light coming from the column remains low mainly because the gas is mostly ionized. On the other hand, the intensity of the patterns coming from the cathode surface is very bright, and possibly caused by glowing neutrals being recycled near the surface.

Towards the end of the sustainment stage, the patterns continue to elongate and cover most of the cathode's planar surface, as shown in Figure 4.14. Also shown in this figure are bright and wide patterns near the divertor opening. Just like the patterns on the cathode, these patterns evolve in time. Nevertheless, they seem to vary in intensity and position around the divertor on a much faster time-scale than the cathode patterns. It is possible that
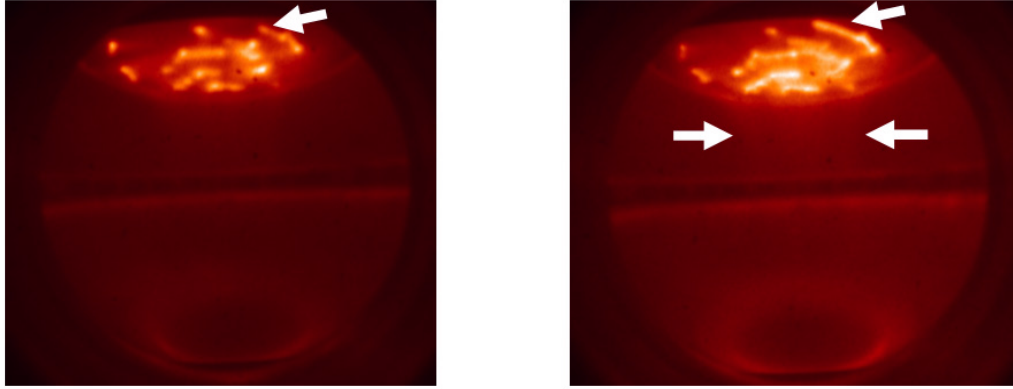
Fig. 4.13. Shot 10407. Left image: $t = 1000$ μs. Right image: $t = 1200$ μs. Gas used: hydrogen. Arrows indicate the pattern that most noticeably elongated (upper), and the faint boundaries of the sustainment central column (horizontal arrows on right image).

these patterns are caused by runaway electrons that scrape the bottom of the flux conserver (which is also the anode).

Note the dim glow around the divertor on both images of Figure 4.13. The patterns near the divertor are very dim (or non-existent) at the beginning of the sustainment stage, and become brighter as time progresses.

4.4 Decay

At this stage the gun current decreases and recombination of plasma into neutrals increases. Features that were previously dim, start to become brighter thanks to more neutrals glowing. At the beginning of the current ramp-down, all the features seen during sustainment remain (the central column, and the cathode and anode patterns). However, changes in the central column do occur. As current decreases, the diameter of the central column increases. For example, Figure 4.15 shows two images taken during the decay stage, with arrows indicating the diameter of the column near midplane. The image on the right shows
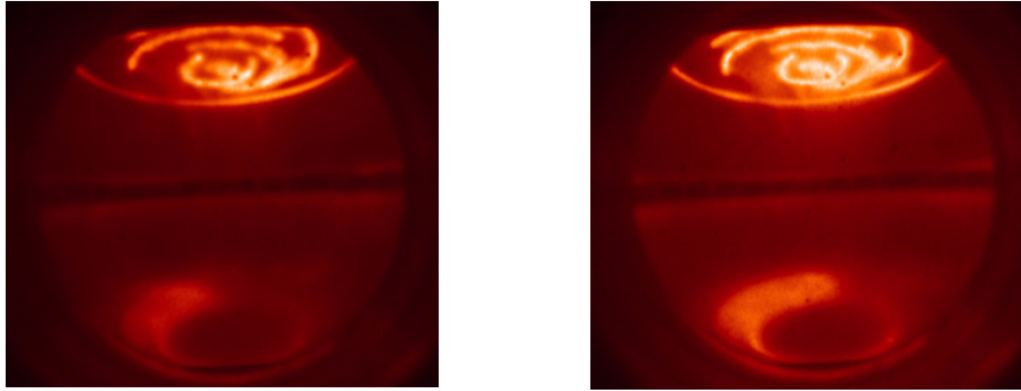
Fig. 4.14. Shot 10409. Left image: $t = 2500\ \mu s$. Right image: $t = 2700\ \mu s$. Gas used: hydrogen.

a column that is brighter and wider. The increase in diameter at the height indicated by the arrows is about 15 percent on the second image.

The column diameter continues to increase until at some point the column drastically seems to break into filaments, like those shown in Figure 4.16. On both images, the cathode displays some patterns similar to those seen at previous times, but these patterns seem segmented, like 'strings of pearls'. Note that the glow on the cathode shown on the right image could still be caused by recycling at the surface since the current flowing into the cathode is still a few kiloamperes.

Near the end of the gun current discharge, no more filaments or other features are seen in the images, except for the cathode patterns that eventually fade away. A discussion about the filamentation process at this stage is also presented in Chapter 6.
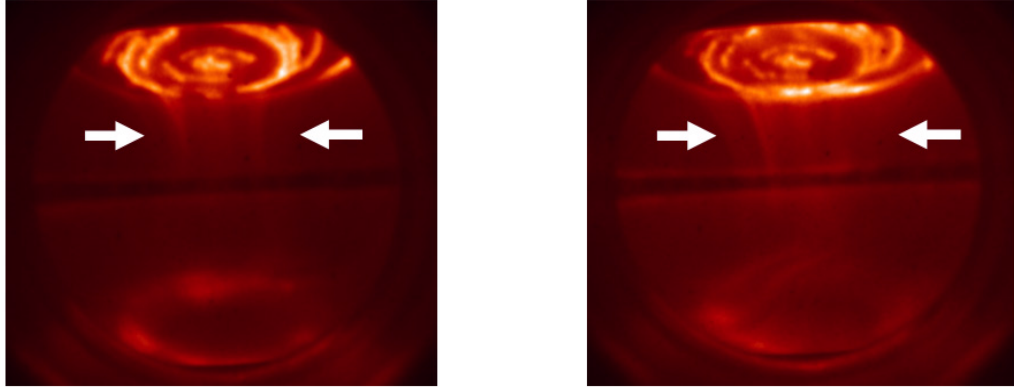
Fig. 4.15. Shot 10420. Left image: $t = 3300 \ \mu s$. Right image: $t = 3500 \ \mu s$. Gas used: hydrogen.
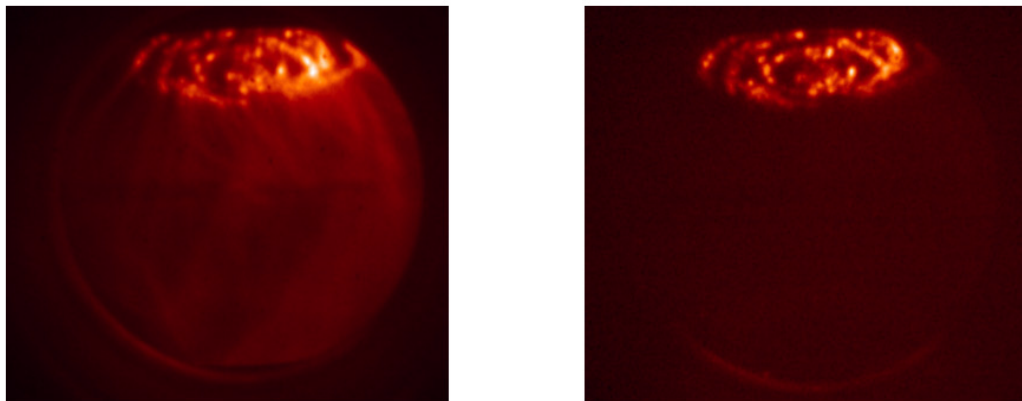
Fig. 4.16. Shot 10436. Left image: $t = 3900 \ \mu s$. Right image: $t = 4000 \ \mu s$. Gas used: hydrogen.

4.5 References

[1]   IDL Version 6.0, Research Systems Inc., http://www.rsinc.com/, August 20, 2004.

[2]   S. C. Hsu and P. M. Bellan, *On the jets, kinks, and spheromaks formed by a planar magnetized coaxial gun*, (to appear in Physics of Plasmas), 2004.

[3]   P. M. Bellan, *Spheromaks: A Practical Application of Magnetohydrodynamic Dynamos and Plasma Self-Organization,* (Imperial College Press, London, 2000), pp. 60 - 69.

[4]   D. D. Ryutov, R.H. Cohen and D. N. Hill. Plasma Phys. Rep. 29 (7), 605 (2003).

Chapter 5

Measurements of the SSPX sustainment central column diameter using high-speed imaging

5.1 Introduction

A central column is expected during gun current sustainment at the Sustained Spheromak Physics Experiment (SSPX). This central column is believed to carry most of the gun current, and is formed by open field lines that intercept the cathode (mostly at the flat end and the edges of the cylindrically shaped cathode) and the anode (also the flux conserver) at various locations. The sustainment central column is sometimes referred to as the 'hole' of the spheromak, because the edge of the column represents the boundary between open and closed magnetic surfaces. Closed magnetic surfaces are expected to be completely contained inside the flux conserver, that is, no field lines from the closed surfaces intercept the flux conserver walls.

Measurements of the central column diameter were obtained during gun current sustainment, using high-speed imaging. These measurements were made from images taken during several experimental runs with similar plasma parameters. The modified flux configuration (see Chapter 2) was used, with a gun flux of 28 mWb. The gas used for all the shots was hydrogen. The gas valve plenum pressure used was about 140 psig. Gettering was performed on most of the runs every third shot to ensure clean plasmas. Reproducibil-

ity between shots of a given run was verified by looking at traces from diagnostics like gun current, gun voltage, and edge magnetics.

This chapter is organized as follows. The method used to find the column diameter from the high-speed images is described in Section 5.2. The column diameter measurements for a large number of shots are presented in Section 5.3. A comparison of some of these results to CORSICA [1], an MHD equilibrium code widely used in SSPX, are presented in Section 5.4.

5.2 Column diameter measurement method

This section describes the method used to measure the central column diameter using high-speed images. All the images used for the measurements were taken through the second generation relay lens (Chapter 3). This lens yielded the best contrast of all the lenses used in the high-speed imaging system. Contrast was important because the sustainment central column was very faint, specially close to midplane.

To increase image contrast and minimize thermal noise in the DiCam-Pro camera, a microchannel plate gain of 30 percent was selected for all the shots. Exposures of up to ten microseconds were also used to increase contrast. These long exposures had the disadvantage of a slight decrease in image resolution. The resulting resolution was of approximately 1 cm near the central column (~ 0.5 m away from the lens).

The acquired images were then digitally processed for further contrast enhancement. The processing was done with Mathematica [2] software. However, before the images could be opened with Mathematica, it was necessary to convert them from 16-bit TIFF format to 8-bit TIFF or JPEG format[1]. Once loaded to Mathematica, the images were

---

[1] The DiCam-Pro camera has its own image format. With the DiCam-Pro software, the images can be converted to 16-bit TIFF. However, Mathematica 5.0 can only read 8-bit TIFF or other standard 8-bit formats.

re-scaled and saved as two-dimensional arrays with 256 levels of gray per pixel (array element). The contrast of this array could be changed using the following operation on every pixel

$$b_{ij} = \left(\frac{a_{ij} - Min[A]}{Max[A] - Min[A]} \right)^n \qquad (5.1)$$

where b_{ij} is the new value of the pixel at array location (i, j), a_{ij} is the original value at that location, $Min[A]$ and $Max[A]$ are the minimum and maximum values of the original image array stored in variable A, and n is the contrast exponent. This contrast exponent was chosen such that the edges of the column near midplane could be distinguished.

A typical image after contrast enhancement is shown in Figure 5.1. The top image is the original plasma image (after digital coloring). The middle image is the contrast enhancement of the top image, using an exponent of $n = 2.3$ in Equation 5.1. The bottom image represents the relative intensity of a row of pixels just above midplane. The vertical dotted lines on the middle and bottom images represent the boundaries of the central column.

The high-speed imaging system has the advantage over many other SSPX diagnostics of having access to almost all of the flux conserver region, and not just the midplane section. This was very useful when finding the edges of the column. That was because, although the edges were typically too faint at midplane, they became more pronounced towards the cathode. This allowed for the measurement to be made just above midplane, and using extrapolation of a straight line over a small distance (about 10 cm) the edge at midplane was estimated.

The central column boundaries were chosen manually for every image[2]. Attempts were made to automate this process by including known edge detection algorithms in Math-

_____

[2] Manually here referrs to a user visually identifying the edges of the central column and recording them one by one.
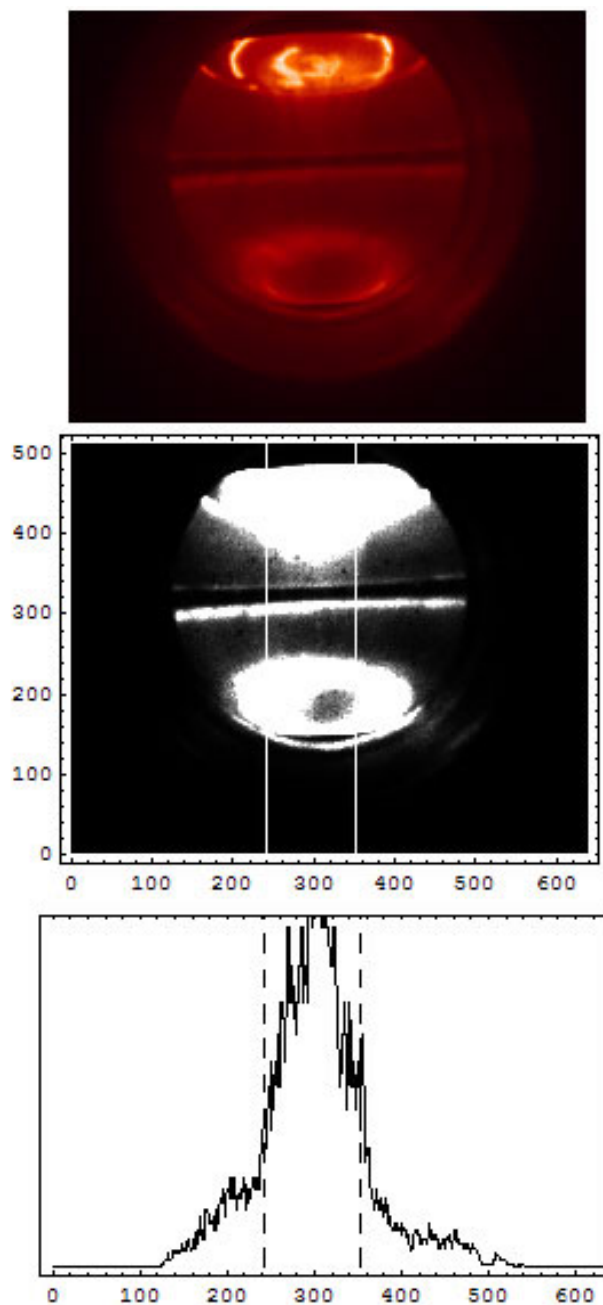
Fig. 5.1. Top: image of shot 10418 at $t = 2300$ μs. Middle: contrast enhancement of the top image to find the central column; the vertical lines mark the center column edges, measured just above midplane. Bottom: relative pixel intensity corresponding to Row 360 in the middle image (after correction for the slight angle of the midplane opening with respect to the horizontal axis of the image).

ematica. Two different edge detection algorithms were tested: the Sobel edge detector, and the Roberts edge detector [3,4]. However, it was found that the uncertainty in the edge position was much greater than in the manual approach. The total uncertainty in the manual measurements, including the uncertainty due to limited resolution, was of ± 1.5 cm. After the edges were selected, their pixel positions were recorded and the width of the plasma column was found (in pixels) by substracting these two values.

A scaling factor was used to convert from pixels to centimeters. This factor was found by measuring the width in pixels of known features (e.g., the opening at midplane, the opening at the divertor, the distance between posts) in shots with no plasma, and compensating for their distance from the camera lens. For example, the opening at midplane (5 cm) and one meter away from the lens took 28 pixels of the image loaded in Mathematica. The same feature would have taken 56 pixels if placed at 0.5 meters from the lens.

5.3 Column diameter measurements

The sustainment central column measurements are shown in Figure 5.2. Five different runs were chosen for their similarities in operation parameters. Due to the limitation of the high-speed camera to obtain only two images per shot, it was not possible to describe precisely the change in diameter of the central column throughout a shot. However, the data indicates a slight column diameter increase (on average) towards the end of the shot.

The best correlation of the column data to SSPX diagnostics was found with the inverse of the poloidal edge magnetic traces. That is, the rate of decrease in poloidal magnetic field at the flux conserver wall correlates well with the rate of increase of the column diameter. A sample of the diagnostic traces is shown in Figure 5.3. These plots show typical traces for the gun current, voltage, and the poloidal and toroidal magnetic fields near the
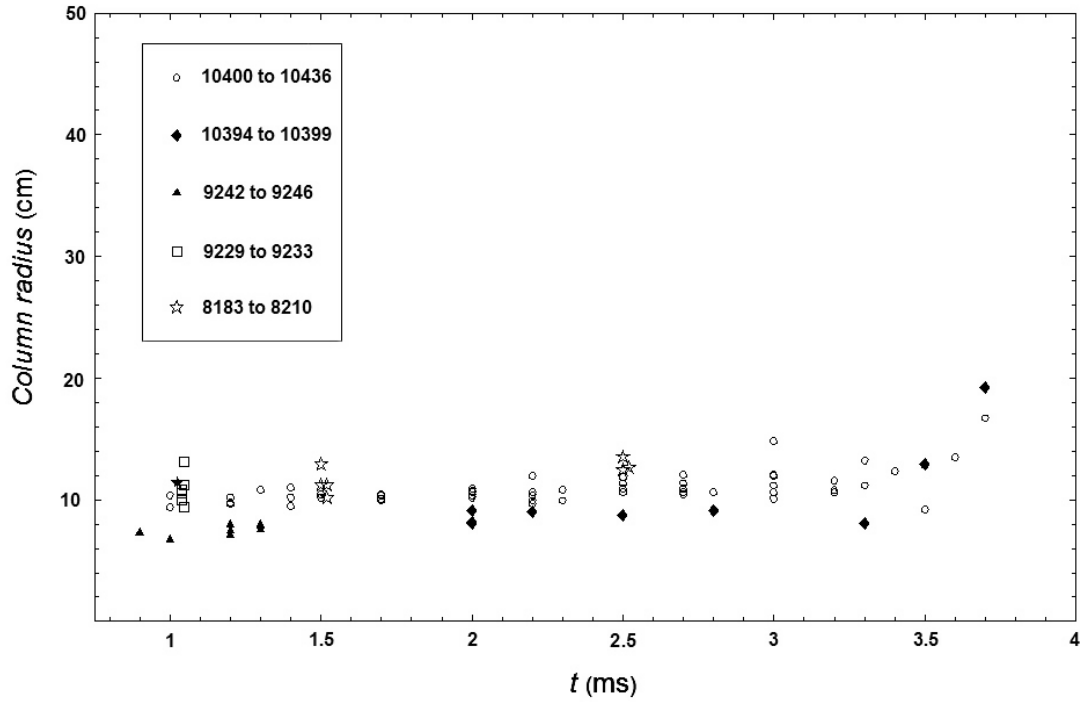
Fig. 5.2. Measured column radius versus time. A total of 92 data points from six different runs (indicated with different symbols) were used for this plot. The uncertainty in these measurements is ± 1.5 cm (except for the data poins near 4 ms, which had more than ± 3 cm uncertainty).

flux conserver wall near midplane. Notice the slope in the poloidal traces on the left plots. The slope decreases towards the end of the shot, until sharply decaying in less than two hundred microseconds.

It is possible that the decrease in magnetic signal at the walls is a consequence of the loss of closed magnetic flux (due to resistive decay), and this in turn decreases the magnetic pressure on the column, allowing it to expand. The central column eventually breaks off into filaments (Chapters 4 and 6), but this happens during current decay. No closed magnetic surfaces are expected after this filamentation event.
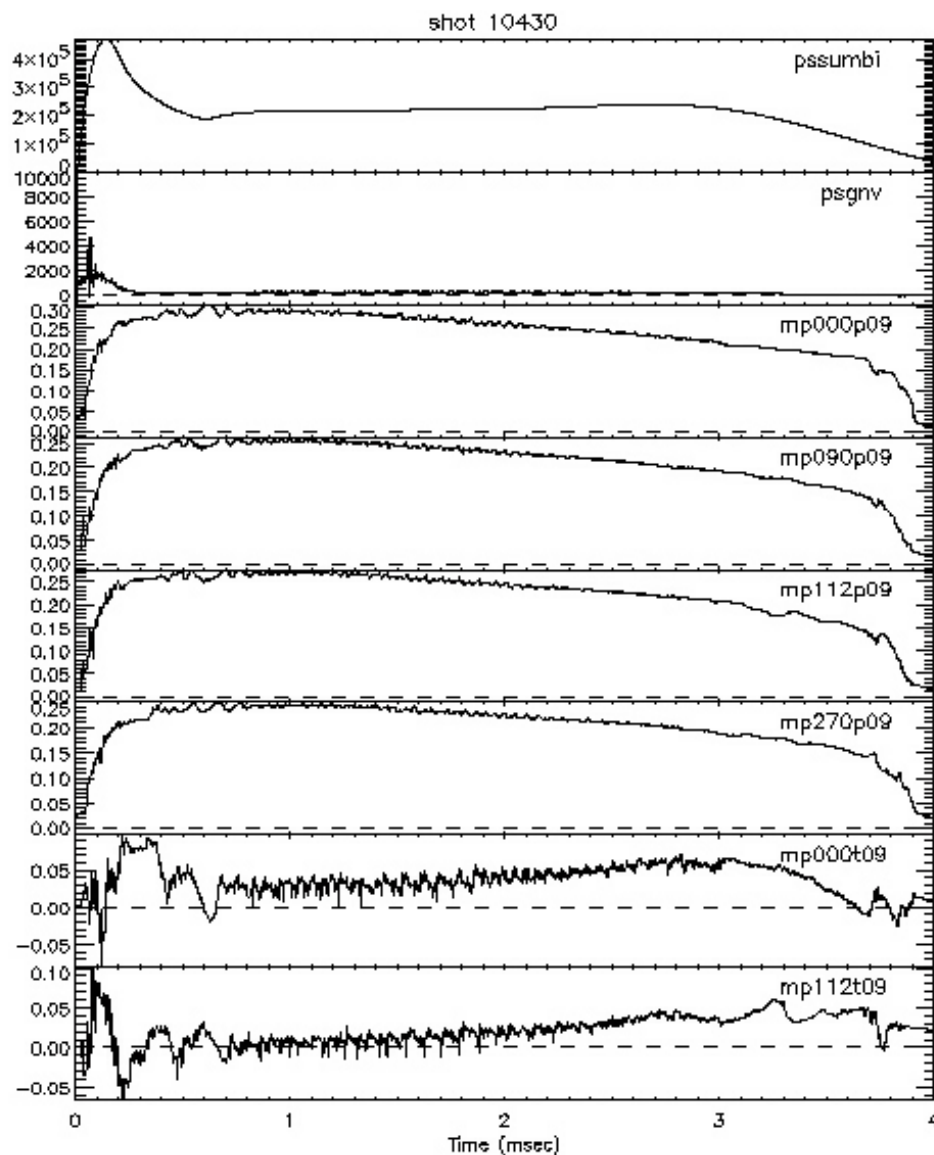
Fig. 5.3. Traces for gun current in units of ampere (top), gun voltage in volts (second from top), and edge magnetics in teslas (bottom six). These traces represent typical data for the shots used in the column radius measurements. For the magnetic traces: mp stands for magnetic probe; the first three digits indicate the position of the probe in degrees around the flux conserver; the following letter p or t, referrs to poloidal or toroidal, respectively; the last two digits indicate that the probes are few centimeters above midplane.
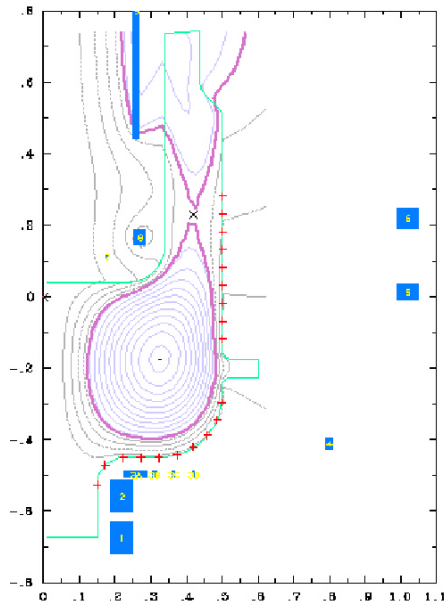
Fig. 5.4. Sample CORSICA output. The purple line in the flux conserver region marks the boundary between open and closed flux surfaces.

5.4 Measurements and CORSICA

A subset of the shots shown in Figure 5.2 was selected to compare the measured column diameter with calculations from CORSICA [1]. This MHD equilibrium code uses the edge magnetic data (like the one shown in Figure 5.3) as boundary conditions to reconstruct the magnetic profile. Figure 5.4 shows a sample CORSICA output after reconstruction of the magnetic profile of an experimental shot. The marks (red crosses) along the outer boundary of the flux conserver indicate the position of the edge magnetic probes.

The radius of the central column calculated by CORSICA is the distance from the chamber axis to the first closed magnetic surface (purple line in Figure 5.4) at midplane. Axial symmetry is assumed in CORSICA, and thus the calculated central column has a circular cross section.
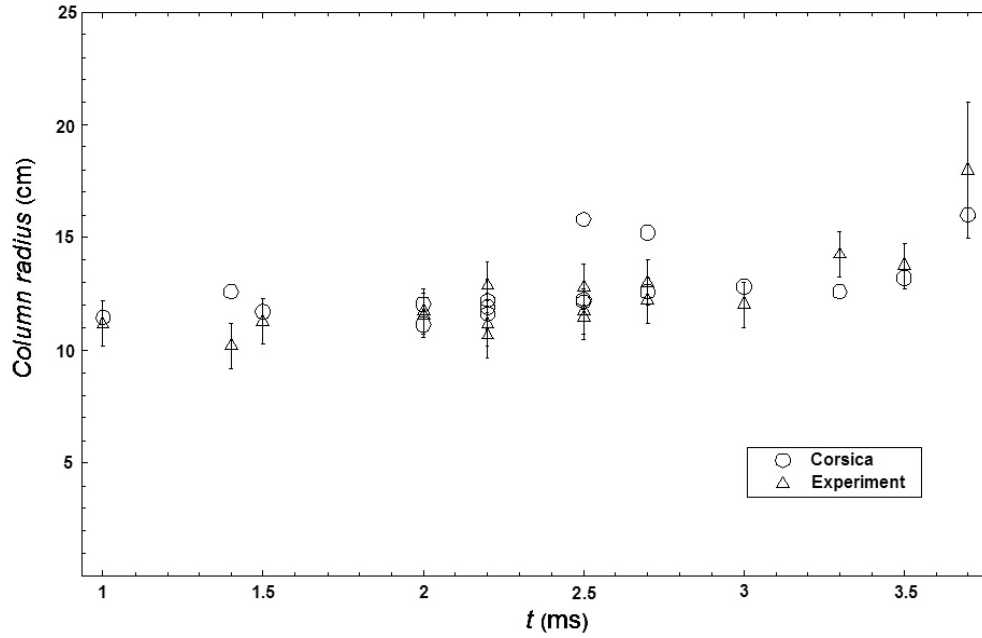
Fig. 5.5. Measured and CORSICA column radius versus time. Selected shots are presented here.

The shots selected for the comparison span the sustainment and decay stages, and were all taken on the run of October 14, 2003. These shots are a subset of shots 10418 to 10436, shown in Figure 5.2). They were chosen because their traces of gun current and edge magnetics have the least shot-to-shot variation. The CORSICA computations were done at the SSPX computer facilities [5], while the images measurements were done at Caltech. The results are shown in Figure 5.5, and they follow closely the experimental results.

5.5 Limitations of the measurement method

For the measurements shown in Figure 5.2, it was assumed that the column was centered in the flux conserver and had a circular cross section. However, this might not be the case. If the column had a non-circular cross section (for example, elliptical) and at every shot

was oriented randomly (or if the column rotates about its axis), the diameter measured with the high-speed camera could have varied as much, or more, as the variation seen in Figure 5.2. One way the issue of the cross-section could be resolved, is by having several views of the central column during the same shot, and perform a tomographic reconstruction of the column[3].

Another limitation of the method used here is the positioning of the column. It was assumed that the column was centered on the axis of the flux conserver. Deviations from the center could lead to an incorrect reading of the diameter of the column. For example, a column that is too close to the lens would give the impression of being much bigger than it really is if it is considered to be on axis.

The off-axis deviation was estimated for the measurements above in the following way. The column edges were first found, as described in the previous sections. With the position of the column edges known, a midpoint between these edges was found. The position of that midpoint was compared to the center of the flux conserver (which was known from calibration of the image to known features), and the distance between the midpoint and the center of the flux conserver was recorded as the off-axis deviation. The measured deviation for the shots presented here was found to be within one or two centimeters, which is comparable to the error in finding the edges.

Even with the mentioned limitations, it might be possible use the column diameter measurements like the ones presented here to further constrain CORSICA, and obtain magnetic profile reconstructions with even higher precision. Additional studies using a combination of the diagnostics and methodology presented here should help to further understand the formation and evolution of bounded spheromaks.

---

[3] The double-branch fiber bundle (Chapter 3) was tested for this purpose, but it was found that the images from the branches were inadequate to distinguish the edges of the column.

5.6 References

[1]   J. A. Crotinger, L. LoDestro, L. D. Pearlstein, et al., *CORSICA: A Comprehensive Simulation of Toroidal Magnetic-Fusion Devices.* Final report to the LDRD program, June 12, 1997.

[2]   Mathematica 5.0, Wolfram Research, Inc., http://www.wolfram.com/, August 20, 2004.

[3]   G. X. Ritter and J. N. Wilson, *Handbook of Computer Vision Algorithms in Image Algebra*, (CRC Press, New York, 2001), Chapter 3.

[4]   S. E. Umbaugh, *Computer Vision and Image Processing: a Practical Approach Using CVIP Tools*, (Prentice Hall PTR, Upper Saddle River, 1998), pp. 61 - 75.

[5]   D. N. Hill, Personal communication. October 24, 2003.

Chapter 6

Measurements of cathode pattern drifts using high-speed imaging in SSPX

6.1 Introduction

During the sustainment part of the current discharge at SSPX, distinct bright patterns were observed close to the electrode surfaces. The most striking patterns were seen on the end face of the cylindrically shaped cathode. These cathode patterns are azimuthally segmented, approximately concentric to the cathode axis, and appear at discrete radial positions. In contrast, the anode patterns which are located near the divertor region are much less well defined than those on the cathode.

Since the DiCam-Pro camera can take two successive images in a SSPX plasma shot, it is possible to study the temporal evolution of these patterns. The cathode pattern morphology did not vary significantly for periods $< 100\ \mu s$, but for times $> 100\ \mu s$ the cathode patterns elongated toroidally and always in the same direction. Measurements obtained from more than thirty shots (at fixed SSPX operational parameters) show that the direction of rotation or elongation of the patterns is counterclockwise. Reversal of the gun bias magnetic field reversed the elongation direction. This suggests the motion is due to $E \times B$ drifts near the surface of the cathode. The direction of rotation or elongation of the patterns on the anode could not be easily measured since the patterns changed at a faster time-scale than that of the patterns observed on the cathode. Nevertheless, some of the images suggest that the anode patterns elongate in a clockwise direction.
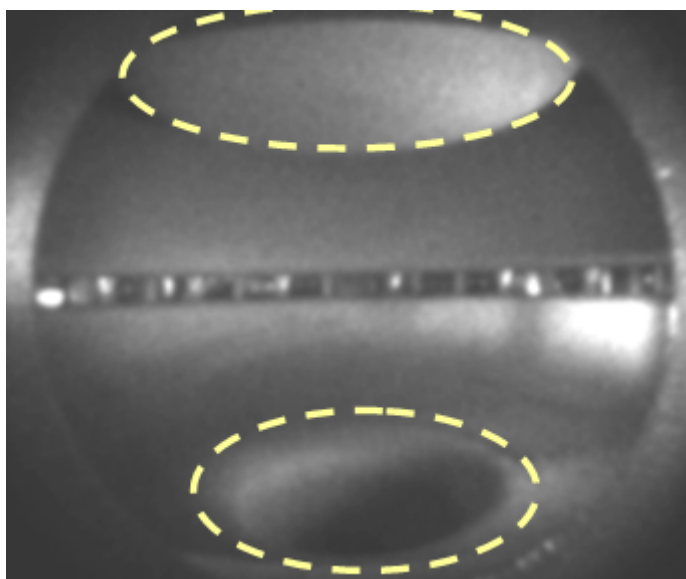
Fig. 6.1. Interior view of the flux conserver as seen through the relay lens on the DiCam-Pro. The upper dotted elipse represents the area of interest on the cathode (inner electrode). The lower dotted elipse represents the area of interest of on the anode (and flux conserver).

Two types of measurements were performed. The first was based on the visual identification of pattern change with respect to time. The elongation of the patterns was calculated by comparing the change in coordinates of the leading edge of the patterns from two subsequent images. The second method was based on a systematic correlation of intensity changes in discrete annular regions. Both methods are discussed in detail in the sections below.

6.2 Stretching of the electrode images for measurements

In order to measure features on the cathode and anode regions, we found it convenient to crop the images to include only the region of interest (marked with dotted lines in Figure 6.1) and then to 'stretch' the resulting images, as shown in Figure 6.2. This stretching gives the impression of looking at the electrodes as if the camera were placed at the axis of the chamber (i.e., rotated $\pi/2$ radians and translated ~ 0.5 meters into the chamber) as shown in Figure 6.3. For the position of the camera lens and the size of the cathode, an aspect ratio of ~ 0.8 was used to map the patterns observed on the electrodes.

It was assumed that the bright features would be close to the electrode surface, such that the stretched images would show the actual shape of the features. However, some distortions exist that cannot be easily corrected. These distortions come from the electrode regions where the surface is either not flat or not parallel to the opening of the flux conserver at midplane. The cathode measurement distortions occur at the edges (which are rounded and smooth) and correspond to the dotted line shown in the upper part of Figure 6.1. The anode distortion due to stretching is at the axis, where the flux conserver opens into what is called the divertor region.
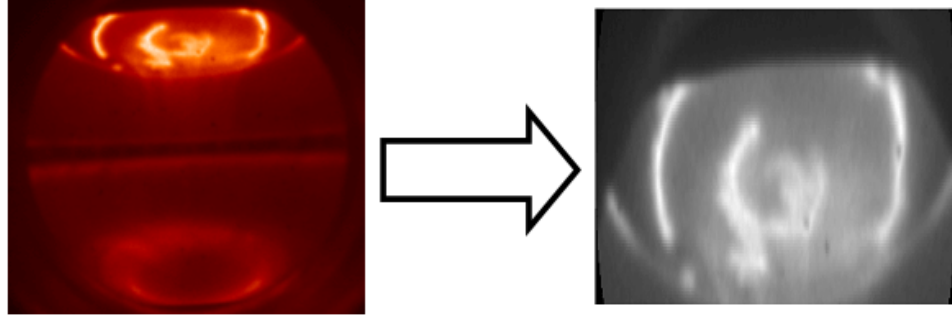
Fig. 6.2. Example of image cropping and stretching. The image to the left is the view of the flux conserver as seen through the lens of the ICCD camera. The image on the right is used for measurements. Shot 10418 at 2.3 ms.
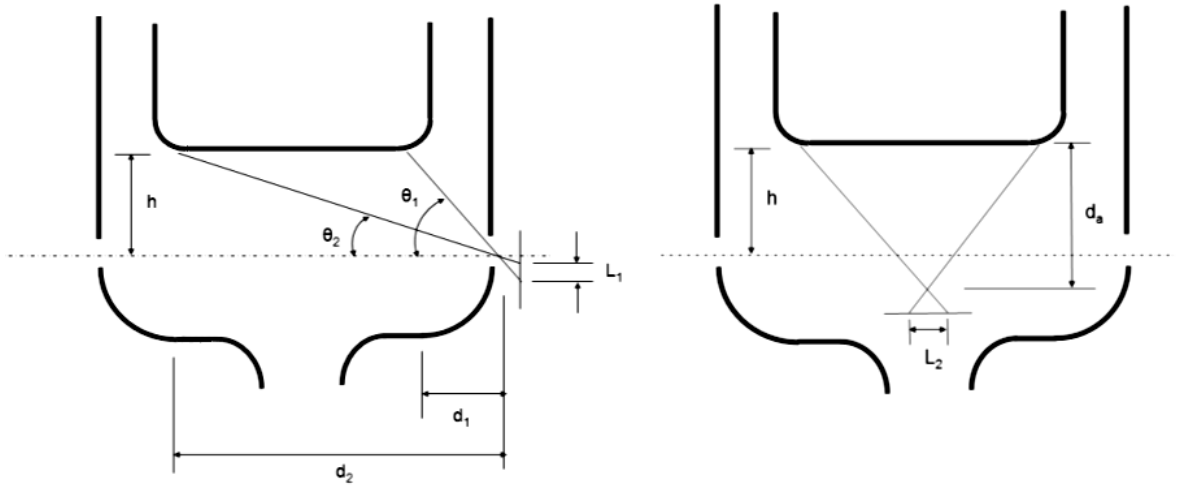
Fig. 6.3. Schematic diagram of the optical field of view of the cathode surface before stretching the image (left) and the apparent field of view after stretching (right). The camera lens is placed where the two rays cross. The ratio of the two images before and after stretching is $\frac{L_1}{L_2} = \frac{hd_a}{d_1 d_2}$. The length d_a can be chosen to be the distance before stretching from the lens (sitting at midplane on the left image) to the cathode surface at the axis of the chamber.

The aforementioned distortion is negligible for the measurements at the cathode, since most of the patterns occur near the center of the electrode. For the anode region the distortion is significant. As will be shown below, the method used to measure the pattern elongation accommodates for distortions, such that the results are unaffected.

6.3 Visual identification and measurement of pattern change at the cathode surface

In this method, pairs of images corresponding to the same shot are compared in order to visually identify those patterns that change in time. A center of rotation in the images is first chosen. Then, the coordinates of those parts of the patterns that changed are recorded. Since the time between images is known, the angular and linear displacement of a given pattern can be estimated, along with the rate of change of the patterns. Figure 6.4 shows an example of pattern change identification. With the aid of a computer program, the images are displayed side by side; the user of the program can then simply select (with the computer cursor) the part of the images that show change in the patterns, and the coordinates of each selection are recorded. The recorded coordinates are used to estimate the radius of rotation, displacement and velocity of the features. In all the images used for these measurements, changes were observed not only in the length of some patterns, but also in the light intensity coming from the patterns. These intensity changes were not taken into account in the method presented in this section since they are difficult to quantify visually. Intensity changes are quantified in the second method (presented in the following section).

It is important to mention that only those patterns that were distinguishable from other patterns in pairs of subsequent images were measured and recorded, as shown in
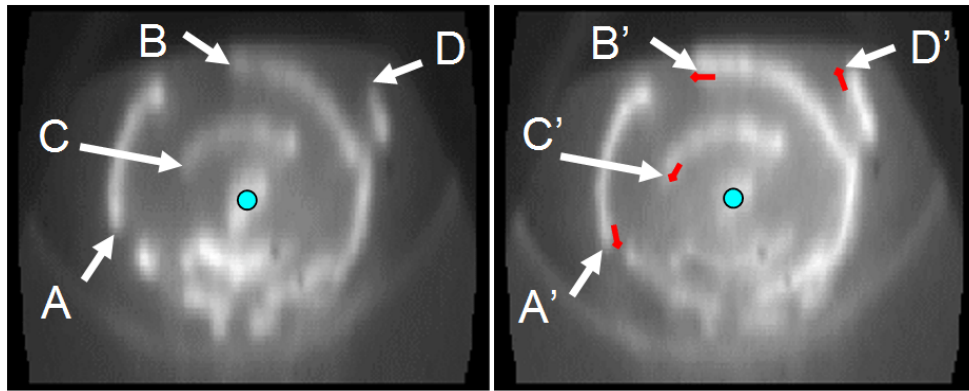
Fig. 6.4. Example of manual identification of cathode pattern elongation. The center of rotation is identified manually (green dots), as well as the patterns to be measured (labeled A through D). The red arrows indicate approximate elongation in counterclockwise direction. Shot 10404, $\Delta t = 0.2$ ms

Figure 6.4. If patterns merged or were too close to other patterns, or if they were too faint to visually distinguish changes, then those pattern changes were not measured.

For images with an inter-frame time of $\Delta t = 0.2$ ms, the average cathode pattern elongation (from 18 different shots with a total of 79 data points) is 2.3 cm ± 1.7 cm. Figures 6.5 and 6.6 show the results for pattern elongation linear velocity and angular velocity and are composed of 112 data points from 25 different shots. The time range between image pairs of every shot is between 0.2 ms and 0.4 ms.

6.3.1 Reversed bias magnetic field

The bias magnetic field was reversed for the same machine operation parameters as those used for the measurements presented above. The measured pattern elongation and velocity remained essentially the same as those presented above, but the patterns elongated in the opposite toroidal direction. Correlation of light-intensity changes of the patterns to their radial position in the cathode (method presented below) was not performed in this case. However, visual inspection of the intensity changes indicates that they are the same as for the case presented for the non-reversed bias field.

6.4 Correlation of intensity changes in discrete annular regions

This section describes the method used to measure intensity changes between images of the same plasma shot. In order to measure intensity changes systematically, a computer program was created to calculate and store the intensity values as a function of the radius r and the angle θ. For a given Δr the program calculates, for both images of a shot, the average intensity values as a function of θ. These average intensity values are kept in one-
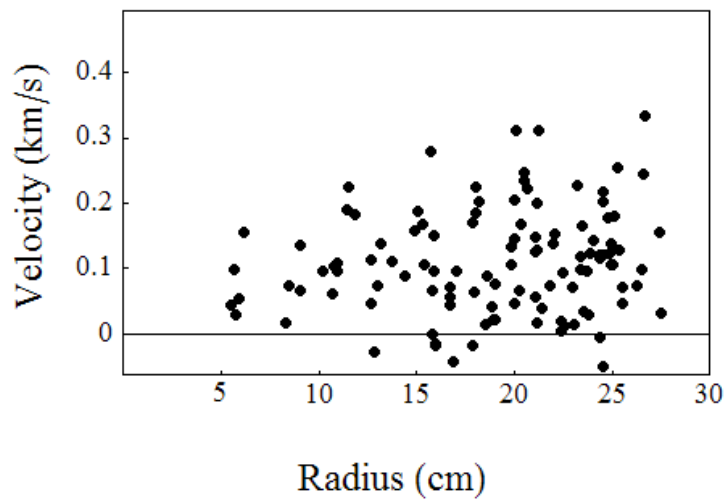
Fig. 6.5. Cathode pattern elongation velocity vs. radius. Δt ranges from 0.2 ms to 0.4 ms. Positive elongation velocity refers to counterclockwise rotation.
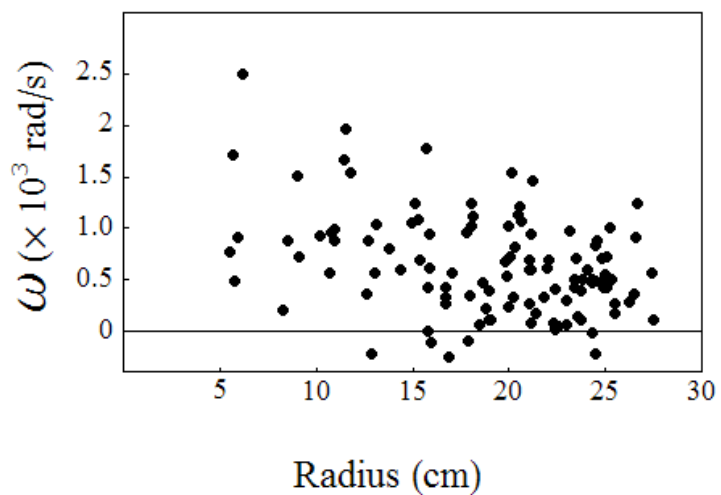
Fig. 6.6. Angular velocity of patterns vs. radius. Δt ranges from 0.2 ms to 0.4 ms.

dimensional vectors, $\mathbf{V}_1$ and $\mathbf{V}_2$, corresponding to every annular region of width Δr in a specified range, $[R_{\min}, R_{\max}]$. A correlation operation is then made between the vectors and is defined as

$$\mathbf{V}_c(r, \theta_s) = \sum_{n=1}^{N} f_1(r, \theta) \cdot f_2(r, \theta + n) \tag{6.1}$$

with

$$f_i(r, \theta) = \begin{cases} 0 & \text{if } \frac{\partial}{\partial \theta} \mathbf{V}_i(r, \theta) \geq 0 \\ \frac{\partial}{\partial \theta} \mathbf{V}_i(r, \theta) & \text{if } \frac{\partial}{\partial \theta} \mathbf{V}_i(r, \theta) < 0 \end{cases} \quad \text{for } i = 1, 2 \tag{6.2}$$

where N is the number of θ-elements in each vector, and θ_s is the shift angle between vectors. The value of θ_s at which the maximum of $\mathbf{V}_c$ occurs corresponds to the most likely value of intensity shift between patterns. Partial differentiation of $\mathbf{V}_i$ with respect to θ, keeping only the negative values of the f functions, helps in defining uniqueness in the maximum value of $\mathbf{V}_c$ (see Figure 6.7).

The computer program inputs required from the user are N, Δr, $R_{\min}$, $R_{\max}$, and the center of rotation of the patterns. In order to match roughly the resolution (in pixels) of the stretched images, and for simplicity, $N = 360$ was used. At every θ location, an average intensity value was found across each Δr slice.

The cathode images were subdivided into forty slices of $\Delta r = 5$ pixels (6.2 cm), from $R_{\min} = 25$ pixels (3.1 cm) to $R_{\max} = 225$ pixels (27.8 cm, which corresponds roughly to the visible cathode radius). Figure 6.9 shows the results for calculations of the average cathode pattern intensity shift, $\Delta\theta$, for images with $\Delta t = 0.2$ ms. The average value for the entire cathode surface is $\Delta\theta = -5.1 \pm 38.5$ degrees. Note in Figure 6.9 that the error bars are much bigger than the average variation of the data, and therefore it is difficult to say much about the behavior of the patterns from that plot. However, the data indicates that the variation of the light emitted from the neutrals occurs on a faster time scale than the inter-frame time (i.e., $\Delta t = 0.2$). The radii values at which the peaks of $\Delta\theta$ shift occur are also of significance. After taking the average of all cathode images (from $\Delta t = 0.2$
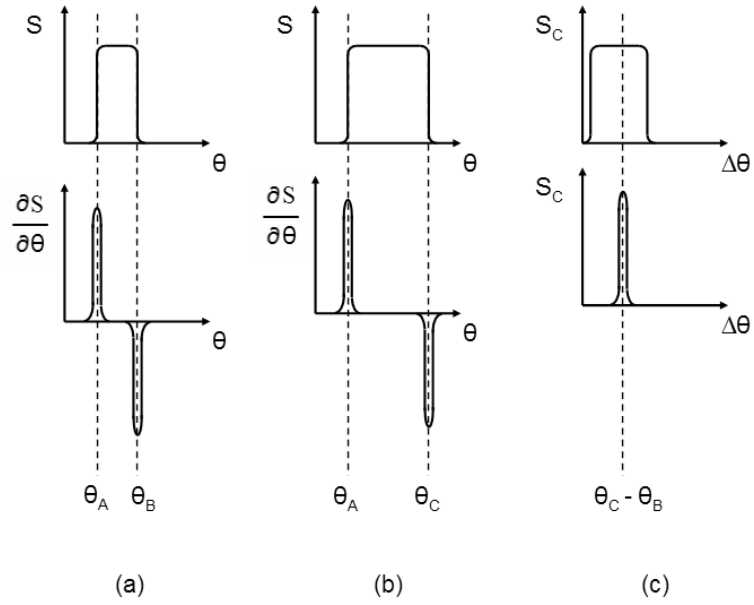
Fig. 6.7. Difference between correlation analysis with and without differentiation (keeping only the negative part) of a given signal S. (a) Signal S and its derivative at $t = t_o$. (b) Signals at $t = t_o + \Delta t$. (c) Correlation S_c of the signals shown in (a) and (b). Note that the correlation of the differentiated signals yields a precise difference of the 'elongated' angle between signals, $\theta_C - \theta_B$, while the correlation of the raw signals has uncertainty (flat top) at the maximum value.
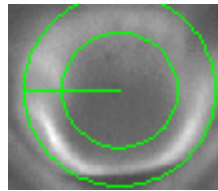
Fig. 6.8. Anode stretched image with radial boundaries for computing pattern intensity shift.
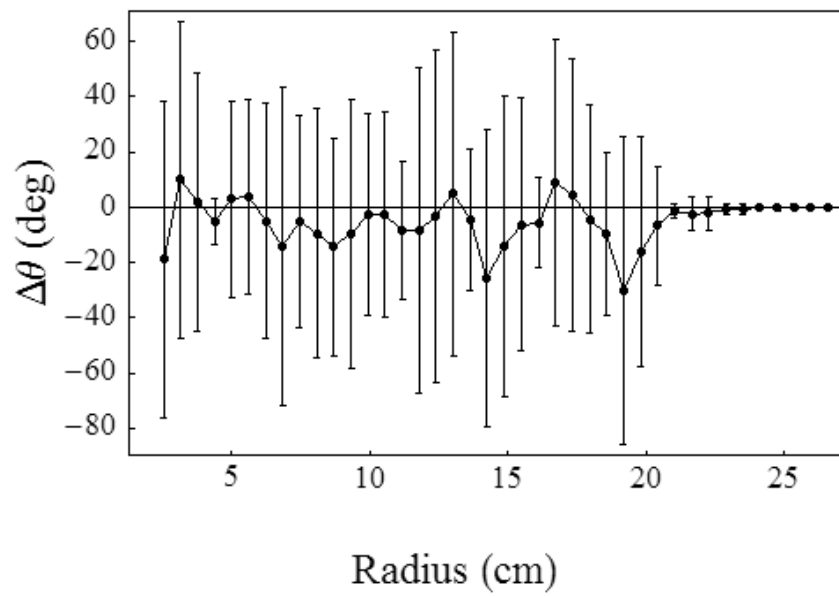
Fig. 6.9. Average cathode pattern intensity shift vs. radius.

to $\Delta t = 0.4$, shown on the left of Figure 6.10), and filtering the resulting image with a convolution operation using a Gaussian kernel to remove some of the noise, bands of intensity are seen corresponding to the regions where it is most probable to find patterns during sustainment of the SSPX discharge. Moreover, the bands also correspond to the strongest peaks found in Figure 6.9, as shown in Figure 6.10.

The anode exhibits much thicker and bigger patterns than the cathode. In this case, a single slice was used with $\Delta r = 90$ pixels (11.1 cm), from $R_{\min} = 135$ pixels (16.7 cm) to $R_{\max} = 225$ pixels (27.8 cm). The boundary used is shown in Figure 6.8. The average anode intensity shift found is $\Delta\theta = -1.4 \pm 4.5$ degrees.

6.5 Plasma drifts

6.5.1 $E \times B$ **drifts**

From the images analyzed above, it is certain that the patterns seen on the cathode and anode move with time. The patterns also seem to have a preferential direction of rotation or elongation (at least for the cathode), depending on the direction of the bias magnetic field near the cathode. This could be due to plasma drifts. The possibility that $E \times B$ drifts [1] are the source of rotation of the cathode patterns is examined here.

The magnetic field must intersect the cathode in order to have azimuthal $E \times B$ drifts. Since the initial condition has a vacuum magnetic field intersecting the cathode (in modified flux configuration), it is assumed the total magnetic flux remains essentially the same throughout the experiment. The justification comes from the characteristic diffusion time of magnetic flux through the cathode material. This is calculated from the magnetic
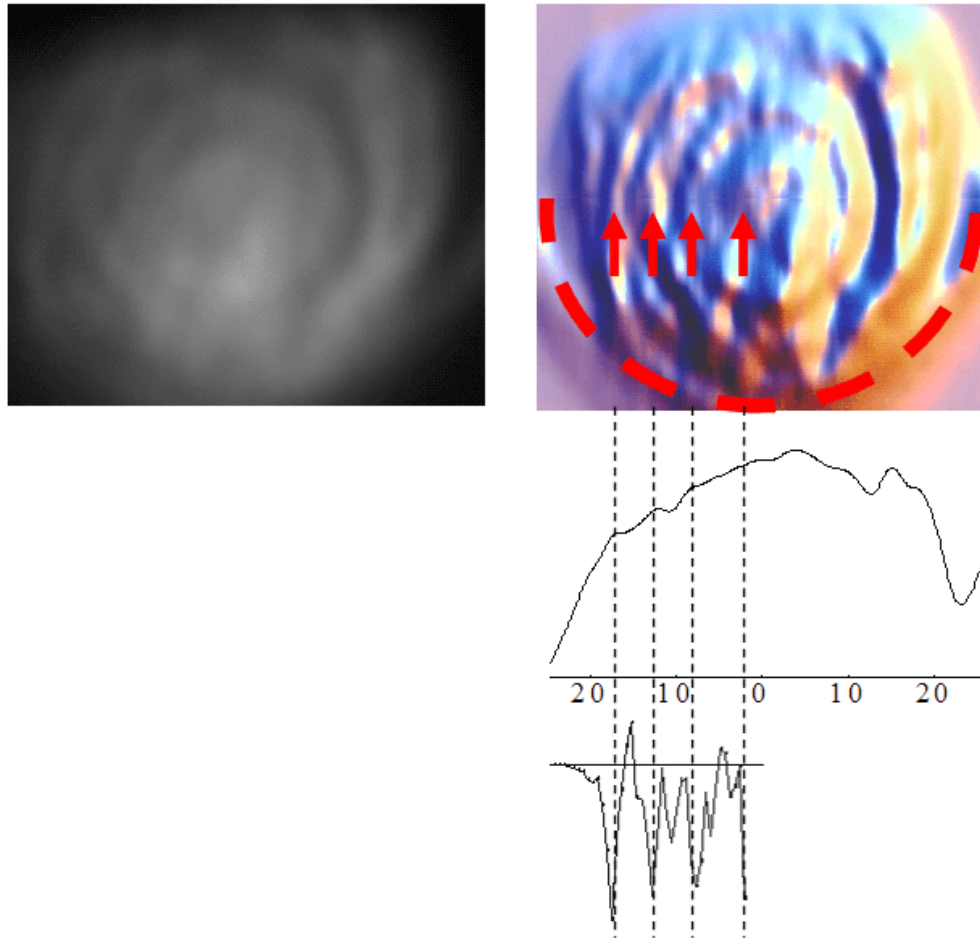
Fig. 6.10. Average image (left) composed of 25 different cathode images. The image on the upper right represents a contour relief of the image on the left. The pattern tracks on the averaged image are marked by the red arrows. The plot in the middle corresponds to relative intensity values along the horizontal of the upper right image, where the red arrows point. The plot at the bottom is the same as in Figure 6.9 (notice the horizontal axis is reversed to match the arrows; for clarity, the error bars are removed and the aspect ratio exaggerated). The red dotted circular segment represents the boundary of the cathode. Units are in centimeters.

diffusion equation

$$\nabla^2 \mathbf{B} = \frac{1}{\alpha} \frac{\partial \mathbf{B}}{\partial t} \tag{6.3}$$

where $\alpha = 1/(\mu_o \sigma)$, μ_o is the magnetic permeability and σ is the conductivity of copper. Although the flux conserver is tungsten coated, the effect of the tungsten will be neglected due to its small thickness, 100 μm [2]. On simple dimensional grounds, the characteristic time τ_d for the field to permeate or decay through the thickness δ of the flux conserver is

$$\tau_d \sim \frac{\delta^2}{\alpha} \tag{6.4}$$

For $\delta = 0.012$ m, $\tau_d \sim 10$ ms, which is much longer than the $0.2 - 0.4$ ms inter-frame time of the images discussed here. Therefore, the total flux going through the electrode should not change significantly on the time scale of the measurements presented here (nor do we expect it to change much during the entire plasma shot).

In order to estimate the electric field, the potential drop across the cathode ionization sheath must be estimated. For completeness, the expression for the potential drop is derived here (derivations and related information about sheath voltages can also be found in [4–6]). The derivation below is for non-magnetized plasmas. However, it was found theoretically by Chodura [7] and experimentally by Tonegawa et al. [8] that the potential drop across the ionization sheath is only weakly dependant on the angle and magnitude of the magnetic field through the sheath.

First, it is assumed that the ionization sheath is constant and that the cathode has the simple geometry shown in Figure 6.12. A 1-dimensional potential drop will also be assumed, i.e., no edge effects. The total current drawn between the electrodes is

$$j_c = e(\Gamma^e_{cw} - \Gamma^i_{cw}) = -e(\Gamma^e_{aw} - \Gamma^i_{aw}) = -j_a \tag{6.5}$$

where j_a and j_c are the anode and cathode currents, Γ^e_{aw} and Γ^i_{aw} are electron and ion fluxes at the anode wall and Γ^e_{aw} and Γ^i_{aw} are electron and ion fluxes at the cathode wall,

Fig. 6.11. Potential profile between electrodes. The voltage applied is $V_a - V_c$ and the sheath dimensions for the anode and cathode are Δ_A and Δ_C, respectively. The plasma potential is V_p.

respectively. We express the voltage applied between the electrodes, V, as

$$V = V_a - V_c \tag{6.6}$$

where V_a and V_c are the anode and cathode sheath voltage drops, respectively. For the electron velocity distribution near the electrode walls, we assume a Maxwellian distribution [9]. The one-way electron flux density at the anode is

$$\Gamma_{aw}^e = \frac{1}{4} n \overline{c_e} \exp(\frac{eV_a}{kT_e}) \tag{6.7}$$

with the average electron thermal speed $\overline{c_e}$ calculated for a Maxwellian distribution as

$$\overline{c_e} = \left(\frac{8kT_e}{\pi m_e} \right)^{1/2} \tag{6.8}$$

Assuming isothermal conditions inside the sheath, i.e., $T_e = T_i$, the ion acoustic velocity inside the sheath is

$$c_s = \left(\frac{k(T_e + T_i)}{m_i} \right)^{1/2} = \left(\frac{2kT_e}{m_i} \right)^{1/2} \tag{6.9}$$

The ion flux at the anode wall is simply

$$\Gamma_{aw}^i = n c_s \tag{6.10}$$

Equation 6.10 implies that the ion speed for both sides of the sheath (i.e., near the electrode wall and near the bulk plasma) is the same.

For the cathode, the ion flux is the same as for the anode (for sufficiently large negative bias, which is the case in our experiment), but for the electron flux at the cathode

$$\Gamma_{cw}^e = \frac{1}{4} n \overline{c_e} \exp(\frac{eV_c}{kT_e}) \tag{6.11}$$

Combining equations 6.5 and 6.10 we have

$$\Gamma_{aw}^e + \Gamma_{cw}^e = 2 n c_s \tag{6.12}$$
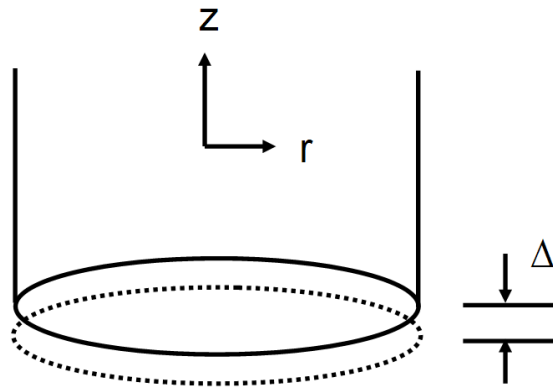
Fig. 6.12. Schematic of the ionization layer, Δ, at the cathode.

Expanding the left hand side of the equation above, and using Equation 6.6, we can solve for the voltage drop at the cathode

$$V_c = \frac{kT_e}{e} \ln \left(\frac{(16\pi)^{1/2}(m_e/m_i)^{1/2}}{1 + \exp(eV/kT_e)} \right) \tag{6.13}$$

For a hydrogen plasma $(m_e/m_i)^{1/2} = 2.33 \times 10^{-2}$ [10], and for sufficiently negative values of V, $\exp(eV/kT_e) \approx 0$. Equation 6.13 becomes

$$V_c = -1.8\frac{kT_e}{e} \tag{6.14}$$

To calculate the electric field across the sheath of the cathode, we use $E_z = -\partial V/\partial z$

$$E_z \approx \frac{2kT_e}{e\Delta} \tag{6.15}$$

where Δ is the characteristic thickness of the sheath, as shown in Figure 6.12.

To estimate the magnitude and direction of the magnetic field near the cathode surface, high-speed images as well as typical equilibrium calculations from CORSICA numerical simulations of MHD equilibrium [11, 12] were used (see Figure 6.13).

High-speed images during current sustainment in SSPX (with exposures of several microseconds) suggest nested current sheets in the central plasma column that map to the cathode surface and create the patterns that we have measured. From these observations we conjecture that ions travel to the cathode through discrete flux surfaces. The most probable radii for these flux surfaces can be inferred from the rings formed in the top-right image in Figure 6.10.

Numerical MHD calculations and high-speed imaging independently suggest that the magnetic field penetrates the cathode surface at an angle (see Figure 6.14 and Figure 6.15 near the cathode region at $t = 3600 \ \mu s$). For the calculations below, we will assume that all magnetic field lines enter the cathode at an angle of ~ 30 degrees.
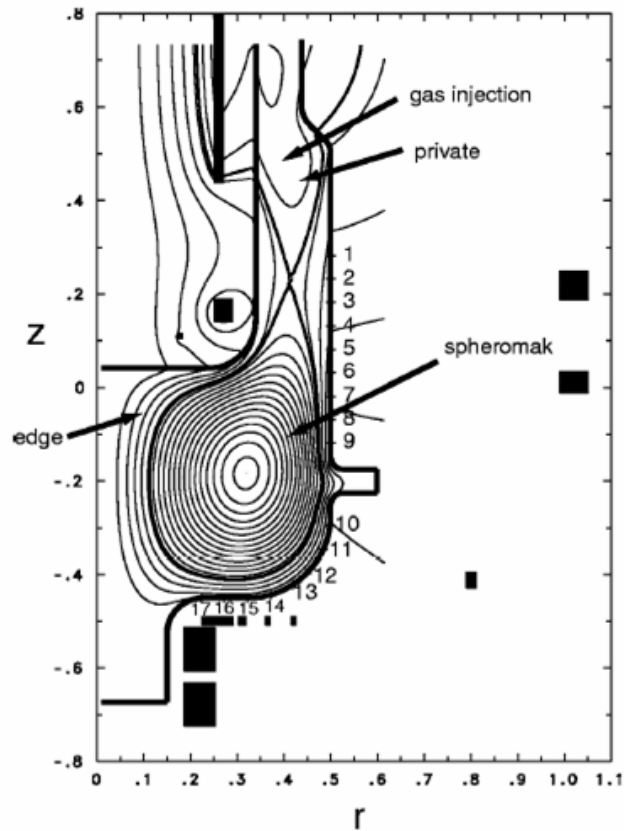
Fig. 6.13. Typical SSPX MHD equilibrium in modified flux [12] (image courtesy of E. B. Hooper). The open flux surfaces (intercepting the cathode near r = 0) were used to get an approximate value for the radius of curvature of the B field in the scrape-off layer (SOL).
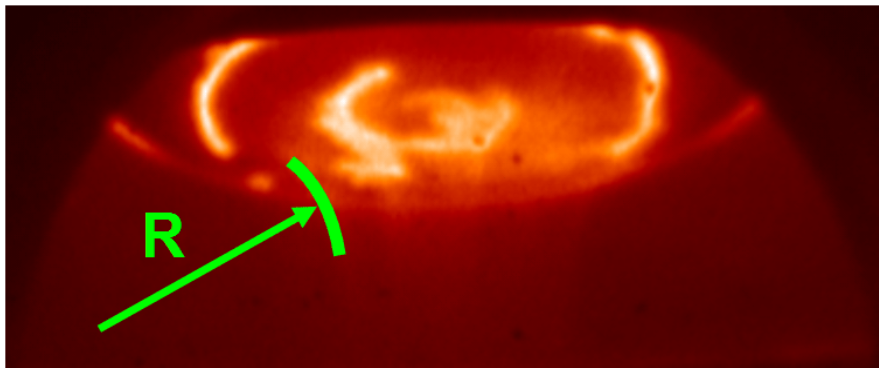
Fig. 6.14. Apparent radius of curvature of field lines near the cathode. (Note: Radius not to scale.) Shot 10418.

Using the same numerical values used by Ryutov et al. in [3], the plasma density and magnetic field strength are, respectively: $n_e \sim 5 \times 10^{19}$ m^{-3}, $B \sim 0.2$ T. The B_r and B_z components of the magnetic field can now be approximated to be

$$B_r = B\cos(30) = 0.17 \text{ T} \tag{6.16}$$

and

$$B_z = B\sin(30) = 0.1 \text{ T} \tag{6.17}$$

For the thickness of the cathode sheath, $\Delta = 0.05$ m is used (based on the thickness of the measured cathode patterns, not on the Larmor radius, as is sometimes used). If we assume $T_e \sim 10$ eV, then

$$E_z = 0.4 \times 10^3 \text{ V/m} \tag{6.18}$$

It will be assumed that E_r is small (with respect to E_z) on the grounds of good conductivity of the cathode material and the plasma near it. It will also be assumed that E_θ is small since the gun current is constant (no polarization currents).

Although it is difficult to measure the toroidal component of the magnetic field, B_θ, an approximate estimation of the magnitude near the cathode can be performed using Ampere's law,

$$\oint \mathbf{dl} \cdot \mathbf{B} = \mu_0 I \tag{6.19}$$

For a circular integration contour and constant $\mathbf{B}$ this gives

$$B_\theta = \frac{\mu_0 I}{2\pi r} \tag{6.20}$$

The gun current at SSPX is typically sustained at about $I = 2 \times 10^5$A. To obtain an approximate value of B_θ near the cathode, an assumption is made that the current per unit area on the cathode end face is constant (and all the current reaches the cathode on that face only). Using Equation 6.20, $B_\theta = 0$ T at $r = 0$, linearly increasing to $B_\theta = 0.16$ T at $r = 0.25$ m.

The general expression for the $E \times B$ drift velocity in cylindrical coordinates is

$$v_{E \times B} = \frac{\mathbf{E} \times \mathbf{B}}{B^2} = \frac{(E_\theta B_z - B_\theta E_z)\hat{\mathbf{r}} + (E_z B_r - E_r B_z)\hat{\boldsymbol{\theta}} + (E_r B_\theta - E_\theta B_r)\hat{\mathbf{z}}}{B_r^2 + B_\theta^2 + B_z^2} \quad (6.21)$$

Images of the cathode during the sustainment stage indicate that pattern elongation occurs only in the θ direction (except at the cathode edge, where there is a slight elongation in the r direction). With this constraint, the terms in the r and z directions of the drift equation must balance to zero. However, if B_θ is of the same order as B_r and B_z then the term in the r direction would not balance to zero. Therefore the assumption that the gun current is evenly distributed, implying a linearly increasing B_θ, must be incorrect. Having a small B_θ near the axis of the cathode implies that most of the current is conducted at the edges of the central column and the cathode (and possibly in the gun region, outside the field of view of the camera).

The resulting expression for the $E \times B$ drift near the cathode surface is

$$v_{(E \times B)_\theta} = \frac{E_z B_r}{B_r^2 + B_z^2} \quad (6.22)$$

Substituting the values from expressions 6.16, 6.17 and 6.18, the magnitude of the $E \times B$ drift velocity in the θ direction is $v_{(E \times B)_\theta} \sim 1.7$ km/s.

According to the results shown in Figure 6.5, the drift velocity has been overestimated by about an order of magnitude. Since T_e was given for the bulk plasma, it is likely that $T_e << 10$ eV for the cathode sheath. Indeed, if $T_e \sim 2$ eV is used, then the estimate of drift velocity gives the same order of magnitude as the measurements in Figure 6.5, i.e., $v_{E \times B} \sim 0.35$ km/s. It is also possible that E_r is considerable (due perhaps to flow asymmetries, as will be discussed in Section 6.7.2) and that E_z is bigger than is estimated here, but they balance in the θ component of Equation 6.21. Note that Equation 6.22 applies mainly at radii smaller than ~ 15 cm. It is possible that B_θ sharply increases towards the cathode edge, thus changing the direction of elongation near that region.

Most images suggest that patterns at the cathode edge elongate in both the r and θ directions. However, elongation and velocity in the r direction were not quantified, since changes in that direction are smaller (and harder to measure) than in the θ direction.

6.5.2 Curvature drifts

The estimated radius of curvature near the cathode is approximately $R_c = 15$ cm for sections of open flux surfaces near the edge, as shown in Figure 6.13.

The plasma drift due to curvature in the magnetic field [13] can be expressed as

$$v_{curv} = \frac{2W_\parallel}{qB^2} \frac{\mathbf{R_c} \times \mathbf{B}}{R_c^2} \tag{6.23}$$

where $W_\parallel$ is the energy of the ions along the flux tube arriving at the cathode. Using the same assumptions and values as in the previous section, $v_{curv} \sim 0.14$ km/s in the θ direction. It is important to mention that curvature drifts depend on the charged particle sign, and thus electrons should move in the θ direction opposite to that observed in the images. Along their path, these electrons could excite neutrals that would emit light. Elongation of the cathode patterns in both directions was not observed; therefore it is unlikely that drifts due to curvature are considerable.

6.5.3 Plasma flow due to $J \times B$ forces near the cathode surface

The modeling of spheromaks is based on the assumption that currents in the plasma are aligned with the magnetic field and create a nearly force free configuration. However, it is possible that near the SSPX cathode this assumption is incorrect and the forces associated with magnetic fields and the sustainment current cause the plasma to rotate toroidally, causing the pattern movement observed in the high-speed images.

There are no expected polarization currents during sustainment, therefore $J_r = 0$ is assumed. Since there is no radial elongation observed, the radial component of the $\mathbf{J} \times \mathbf{B}$ force must balance to zero, thus

$$J_\theta B_z = B_\theta J_z \tag{6.24}$$

The resulting expression for a purely toroidal force near the cathode surface is

$$(\mathbf{J} \times \mathbf{B})_\theta = J_z B_r \tag{6.25}$$

This expression is similar to Equation 6.22.

Note that plasma rotation due to $J \times B$ forces is fundamentally different from $E \times B$ drifts. A continuos force would imply an acceleration of the plasma. However, the measurements shown in Figures 6.5 and 6.6 were taken at different times throughout the sustainment stage, and thus suggest that the elongation velocity is approximately constant for the entire stage. Therefore, if $J \times B$ forces are responsible for this rotation, then these would have to be intermittent or have dissipation (i.e., viscosity).

To date, there are no measurements of the current profile near the cathode, and thus the components of the current and their spatial distribution are not known well enough to quantify their effect on the observed pattern elongation.

6.6 Filamentation of current near the cathode

Images taken during the decay phase of a typical SSPX shot suggest the presence of flux tubes or channels near the cathode. In Figure 6.15 current is decaying and the plasma temperature is colder than during sustainment, allowing for more recombination and hence more light emitted by neutrals. At $t = 3600 \ \mu s$ the filaments are already visible (marked with the white arrow) and apparently extend to the bottom of the flux conserver. At $t = 3800 \ \mu s$ structures are more diffuse. There is also presumably a drastic change in magnetic

configuration between the first and second images (i.e., loss of closed magnetic surfaces), but patterns can still be observed on the cathode. Structures attached to the cathode also become more diffuse and less defined, like the one marked by the two white arrows on the right image in Figure 6.15. After the gun current has decayed to a low enough value (~ 50 kA), the features seen in the plasma start to get dimmer. At this stage, there are plenty of neutrals, but little plasma to interact with them and make them glow. Figure 6.16 shows filamentation of the current arriving at the cathode. Since dI/dt is large and negative at this stage, we expect a polarization current to 'untwist' the flux channels, and so the field lines should straighten out. Note that the cathode patterns remain throughout this stage, but no patterns are seen anywhere on the anode.

6.7 Discussion and conclusions

From the measurements presented above, it is clear that cathode patterns elongate in a constant toroidal direction. This is especially true for radii < 15 cm. For greater radii values, some elongation in the radial direction was observed but was too small to be quantified. Elongation of the cathode patterns was measured for intervals greater than 0.1 ms between images of the same shot. For the anode, the patterns move on a time-scale much faster than 0.1 ms and are not as well defined as those at the cathode. All measurements were made from images taken during current sustainment.

6.7.1 Drifts and the hollow current profile of the central column

Taking into account the magnetic field shape and strength at the cathode surface, and estimating the electric field across the ionization sheath of the cathode, calculations indicate that $E \times B$ drifts might be responsible for the elongation of the patterns. It was found

t = 3600 μs   t = 3800 μs
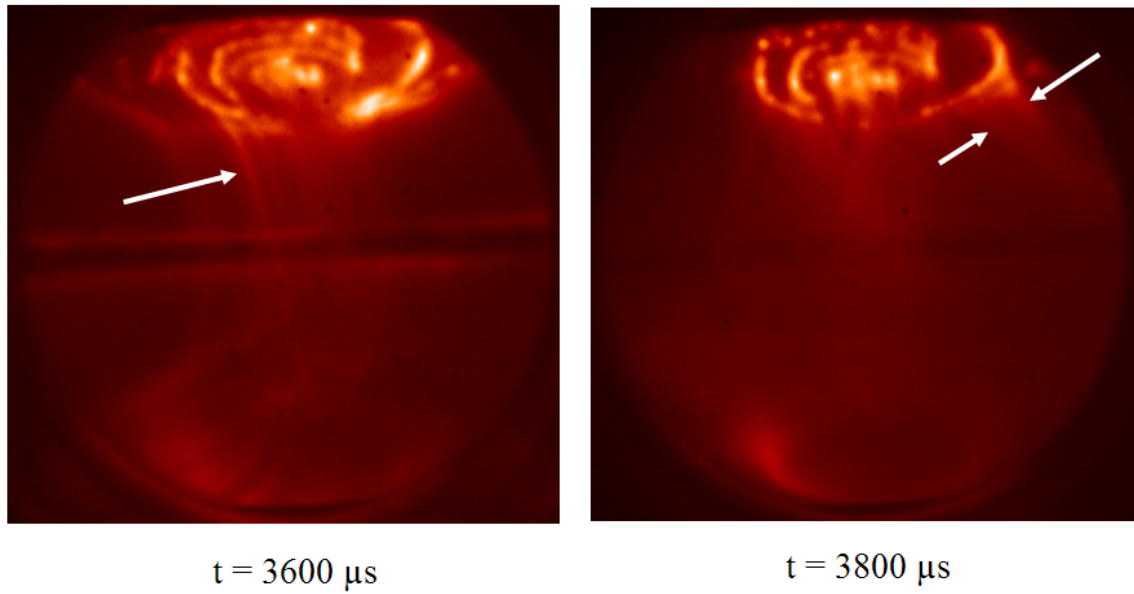
Fig. 6.15. Filamentation mapping to the cathode during the deacy phase of the current in SSPX. As the current decreases, the recombination of plasma to neutrals increases and emits more light that is captured by the camera. Shot 10432.

t = 3800 μs   t = 3900 μs
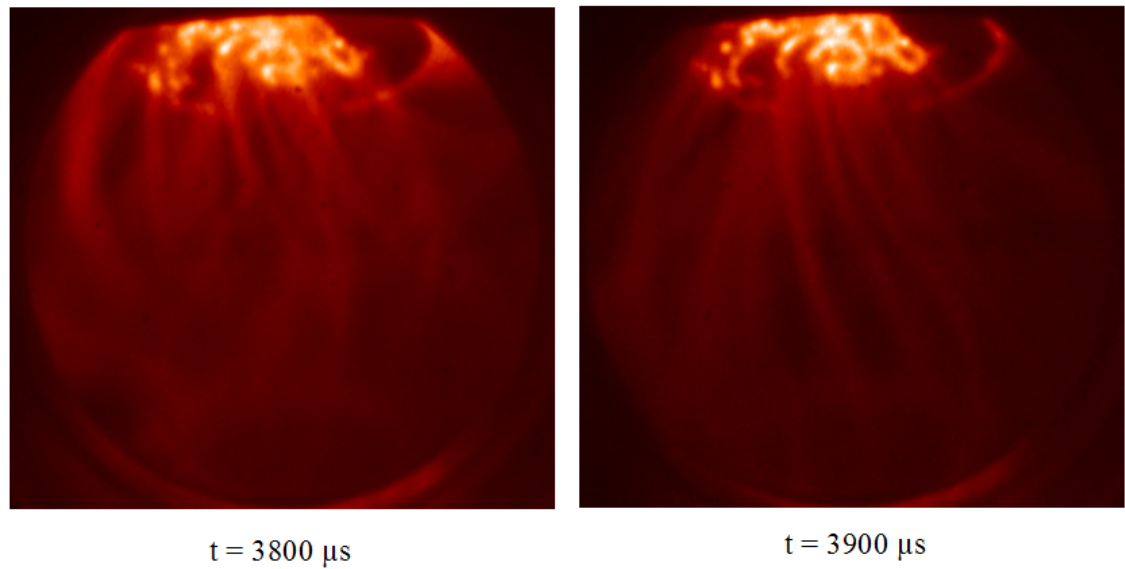
Fig. 6.16. Filamentation observed during current decay. No closed flux surfaces are expected at this stage.

that B_θ and E_r must be small close to the cathode axis in order for the patterns to elongate only in the θ direction. It is possible that B_θ and E_r become significant towards the cathode edge, thus changing the elongation direction. This would also explain the small r component in the elongation of the patterns near the edge.

A very important implication of small B_θ near the cathode end-face is that most of the current is not collected on that face. However, the discharge current still has to arrive at the cathode somehow, so if the pattern elongation direction is towards the edge, it is possible that most of the current reaches the round face (somewhere outside the field of view of the high-speed camera). Ryutov, Cohen and Hill [3] reported 'chicken track' marks on the round face, near the edge of the SSPX cathode. Those marks cannot be explained using the expressions derived in their paper (which provides a phenomenological model for plasma filamentation and the tracks that it leaves on the cathode during breakdown and ejection from the SSPX gun). This hints at the sustainment central column as being like a 'hollow' conductor close to the cathode, with most of the current going through the edge of the column, but with enough on the inside to create patterns on the cathode end-face.

6.7.2   Flow asymmetries

For any given plasma shot, the patterns never elongated at the same angular rate. The shot to shot variation in the elongation rates with respect to radii, and the variation in intensity of the light coming from the patterns, indicate that the temperature (and therefore the voltage) across the ionization sheath varies significantly throughout the current sustainment phase of SSPX.

Extensive theoretical and experimental investigations of the ionization sheath and scrape-off layer (SOL) have been carried out mainly for tokamaks. Cohen and Ryutov [15] present a unified picture of the drift phenomena on open field lines and derive the boundary

conditions necessary to describe convection and flow asymmetries near ionization layers for magnetic confinement devices. In their analysis (which includes an extensive list of references to previous work), they find that, for a magnetic field intercepting a wall (or layer of neutrals) at a shallow angle, plasma asymmetries driven by convection near the surface wet the surface only at some locations. These asymmetries cause cross-electric fields (in our case radial or toroidal) that can drive currents. In all the images analyzed, it was evident that the patterns at the cathode were elongating in a toroidal direction that depends on the sign of the B field and that one side of each individual pattern stays fixed. Besides $E \times B$ drifts, it is possible that the cross-electric fields at the ionization sheath, especially near the cathode edge, are responsible for such elongation.

During current sustainment, the plasma is expected to have currents across B-field lines near the cathode only due to flow asymmetries. When the current decays, pattern elongation is also observed. However, it is possible that at this stage $E \times B$ and curvature drifts are small, but polarization currents due to flow asymmetries and due to $dI/dt < 0$ are big and responsible for the elongation observed.

6.7.3   Nested flux surfaces and current filamentation

We now conjecture that the patterns observed on the cathode are projections of the open flux surfaces that carry currents. This means that current flows only at discrete radial locations along the central column. The outermost open surface can be identified from the change in brightness of the central column or 'hole' of the spheromak (Chapter 5). Note that MHD equilibrium analysis of the spheromak configuration allows for a continuum of open flux surfaces (both open and closed).

Although there are no closed flux surfaces expected late in the decay of the SSPX gun current, filaments and cathode patterns observed during that stage are also an indication of

discretization of flux surfaces. In Figure 6.16 for example, some of the filaments clearly map to the patterns on the cathode. Those same filaments extend from the cathode to the bottom of the flux conserver (near the divertor opening), and a slight helical twist on each of them is also apparent.

It is important to point out that the MHD equilibrium solutions obtained from COR-SICA do not contain details of filamentation. The fact that filamentation is found in the plasma, however, does not contradict the MHD solutions. The plasma can flow in filaments and still be attached to distinct flux surfaces. Plasma filamentation (driven by pressure gradients or by currents) has been widely studied for other magnetic confinement concepts with open and closed field lines (see, for example, [16–21]). Even though the sustainment central column of SSPX has stabilizing curvature in the magnetic field (concave towards the plasma) and the magnetic field intercepts highly conducting plates, filamentation is still present. Berk et al. [22] developed a model to address this issue. Their model predicts a rapidly growing flute-like instability based on the electron temperature gradient across field lines (i.e., parallel to the electrodes). At SSPX, there are no measurements of the temperature profile near the electrodes. However, if it is assumed that the light-intensity profile measured from images correlates to electron temperature, then the middle plot in Figure 6.10 indicates that there is a radial temperature profile near the cathode. Based on the $E \times B$ calculations presented above, it is reasonable to expect that the colder plasma temperature occurs at the cathode axis and increases towards the edge (i.e., with a profile inverted to that shown in the middle plot in Figure 6.10, due possibly to the low ionization percentage at the axis, with high neutral glow, and high ionization percentage towards the edge, with low neutral glow).

The apparent constant cross-section of the filaments can be explained by the model proposed by Bellan [23], in which current-carrying flux tubes that are bulged can become

thin and uniform by accelerating (and thus ingesting) plasma due to non-conservative $J \times B$ forces. Once the cross-section of a flux tube is constant throughout its length, the pumping effect ceases. The temperature gradients mentioned above, coupled to the pumping effect when there are perturbations from equilibrium (i.e., $\mathbf{J} \times \mathbf{B} \neq \mathbf{0}$), could be responsible for the fast change of brightness of the patterns observed on the electrodes.

6.8 References

[1]   R. J. Goldston and P. H. Rutherford, *Introduction to plasma physics*. IoP Publishing. Philadelphia, 2000. pp. 24 - 26.

[2]   R. D. Wood, D. N. Hill, E. B. Hooper, et al., J. Nucl. Mater. 290 - 293, 513 (2001).

[3]   D. D. Ryutov, R.H. Cohen and D. N. Hill. Plasma Phys. Rep. 29 (7), 605 (2003).

[4]   P. C. Stangeby, *The plasma boundary of magnetic fusion devices*. IoP Publishing. Philadelphia, 2000. pp. 79 - 84.

[5]   F. F. Chen, *Introduction to plasma physics and controlled fusion*, Vol. 1: Plasma Physics, second edition. Plenum Press, New York, 1984. pp. 290-295.

[6]   R. J. Goldston and P. H. Rutherford, *Introduction to plasma physics*. IoP Publishing. Philadelphia, 2000. pp. 3 - 7.

[7]   R. Chodura, Phys. Fluids 25, 1628 (1982).

[8]   A. Tonegawa, M. Ono, S. Sakamoto, et al., *Proceedings of the ICCP & 25th EPS Conference on Contr. Fusion and Plasma Physics*, Praha, ECA **22C**, 47-50 (1998).

[9]   P. C. Stangeby, *The plasma boundary of magnetic fusion devices*. IoP Publishing. Philadelphia, 2000. pp. 64 - 70.

[10]   J. D. Huba et al., *NRL Plasma Formulary*. Naval Research Laboratory, Washington, 2002, p. 29.

[11] J. A. Crotinger, L. LoDestro, L. D. Pearlstein, et al., *CORSICA: A Comprehensive Simulation of Toroidal Magnetic-Fusion Devices.* Final report to the LDRD program, June 12, 1997.

[12] B. W. Stallard, E. B. Hooper, S. Woodruff, et al. Phys. Plasmas 10, 2912 (2003).

[13] R. J. Goldston and P. H. Rutherford, *Introduction to plasma physics.* IoP Publishing. Philadelphia, 2000. pp. 33 - 36.

[14] R. J. Goldston and P. H. Rutherford, *Introduction to plasma physics.* IoP Publishing. Philadelphia, 2000. pp. 52 - 56.

[15] R. H. Cohen and D. Ryutov, Phys. Plasmas, 6 (5), 1995 (1999).

[16] R. J. Goldston and P. H. Rutherford, *Introduction to plasma physics.* IoP Publishing. Philadelphia, 2000. Chapter 19.

[17] I. F. Shaikhislamov, J. Plasma Phys. 68 part 1, 59 (2002).

[18] Ch. P. Ritz, H. Lin, T. L. Rhodes, A. J. Wooton, Phys. Rev. Lett. 65, 2543 (1990).

[19] C. Hidalgo, C. Silva, et al., Phys. Rev. Lett. 83, 2203 (1999).

[20] V. Antoni, D. Desideri, et al., Phys. Rev. Lett. 79, 4814 (1997).

[21] S. Coda, M. Porkolab, K. H. Burrell, Phys. Rev. Lett. 86, 4835 (2001).

[22] H. L. Berk, D. D. Ryutov, Y. A. Tsidulko, Phys. Fluids B (3), 1346 (1991).

[23] P. M. Bellan, Phys. Plasmas (10), 2000 (2003).

Chapter 7

Image restoration and tomography in SSPX using the maximum entropy principle

7.1 Introduction

High-fidelity imaging of the Sustained Spheromak Physics Experiment (SSPX) plasmas proved to be a challenging task. The most common problems encountered were blurriness and noise in the images. Blurriness resulted if the optics were misaligned, if there was stray light or undesired reflections going into the camera, or by aberrations [1] caused by limitations in the optics (Chapter 4). Image noise can be caused by spurious signals (mainly from thermal noise[1]) being amplified in the camera micro-channel plate (MCP) or in other electronics. Both of these problems can substantially degrade the image quality, and ultimately, the information that can be extracted from these images.

All the blurring mechanisms of an imaging system can be lumped into a single function, which is typically referred to as the point-spread function[2] (PSF). Image blurring can then be stated as the convolution of the real image (the image before it enters the instrument) with the PSF (which might include noise). In this sense, image restoration becomes a deconvolution problem.

Digital image processing is an active area of research, and thus numerous methods exist to digitally restore and enhance, to some extent, blurry and noisy images (see for

---

[1] To minimize thermal noise amplification, the DiCam-Pro has a cooling system to lower the temperature to -12 °C.

[2] Some authors also refer to the PSF as a degradation function, or instrument function.

example [2–6, 8]). Of particular interest here is the maximum entropy restoration method [6, 8], which is based on the Shannon concept of entropy as an information measure[3]. This method has the advantage of being robust for sets that are small or incomplete, i.e., have missing pixels [11]. This robustness contrasts with Fourier-based methods for which, in incomplete sets, the phases of the Fourier components are either inaccurate or unknown; because of these inaccuracies, the resulting reconstructions with Fourier-based methods often have artifacts. The maximum entropy algorithm and its implementation as a method for image restoration is derived here.

Interestingly, tomography, which is the cross-sectional imaging of an object reconstructed from transversal projections, can also be formulated as a convolution problem [12]. The larger the number of projections from different angles, the more precise the reconstruction will result. Medical imaging is the main application of tomography and has motivated the development of vast amounts of literature in the subject. However, mathematical methods geared for medical applications often assume that large data sets (typically hundreds to thousands of precision projections) are available. These methods become inappropriate for reconstruction when data sets are small. Therefore, anyone seeking to use tomographic techniques on small data sets and obtain the best possible reconstruction, normally has to tailor a method to their particular application. This is the case for the tomographic reconstruction of the SSPX transient central column from images taken with the double-branch fiber bundle.

Reconstruction of sections from the SSPX transient plasma column from only two projections is presented here. This tomographic method was created specifically for the geometrical and data-limited constraints of SSPX. The method is a combination of the

---

[3] E. T. Jaynes [9, 10] discusses in detail the fundamental implications of the maximum entropy concept applied to information theory.

above mentioned algorithm for image restoration, and a simple tomographic technique known as summation method [13]. However, since only two projections were used for the reconstructions, severe limitations were found with respect to other tomographic methods. Regardless of these limitations, this method was found useful in studying properties of the transient plasma column, in a way complementary to the images shown in Chapter 4.

This chapter is organized as follows. The maximum entropy algorithm is derived for completeness in Section 7.2. The characterization of the SSPX high-speed imaging system PSF using the double-branch fiber bundle, and the second generation relay lens (Chapter 3), is presented in Section 7.3. Examples of restored images using the maximum entropy method are also presented in this section. A derivation of the tomographic technique used here to reconstruct parts of the SSPX transient column is presented in Section 7.4. Reconstructions using this method with simulated patterns, as well as with actual images, is also presented in this last section.

7.2 Maximum entropy image restoration

In this section the maximum entropy restoration method and a computational algorithm to implement it are derived. The derivation of the maximum entropy method is largely based on the work of Wilczek and Drapatz [6], and the implementation algorithm is based on notes by Bellan [7].

7.2.1   The restoration method

Image acquisition with a linear image formation system, such as a photographic camera, can be described by the convolution equation

$$g(x, y) = \int_{-\infty}^{\infty} \int_{-\infty}^{\infty} h(x - \xi, y - \eta) f(\xi, \eta) d\xi d\eta \qquad (7.1)$$

where f is the true image brightness, h is the point-spread function (PSF) of the camera, and g is the image after being captured by the instrument. The problem of image restoration is to find f given g and h. In digital images (i.e., captured with CCD cameras), the information is inherently discretized. Therefore, it is appropriate to use summations instead of integrals. For convenience, single indexing will be used in the rest of the derivation.

Measurement errors are always present in a real imaging system. These errors might include noise in the capturing device, and thus need to be taken into account. Equation 7.1 can be expressed as

$$g_k + e_k = \sum_{i=1}^{n} h_{ik} f_i , \qquad k = 1, ..., m \; (m < n) \qquad (7.2)$$

where e_k is the unknown error at every pixel. In the present derivation it is assumed that the point-spread function h does not lose information (no edge effects) when operating on f. Therefore the requirement $m < n$ implies that h does not operate at the edges of the image, but somewhat inside only. This results in the total image brightness being the same for g and f (this will become useful later in the derivation).

Equation 7.2 is ill-conditioned, and thus the true distribution f cannot be found exactly with the available information. Instead, an approximate solution that can produce an 'acceptable' distribution f will be sought. With this in mind and following the same approach as Gull and Daniell [11], the noise is assumed to have a Gaussian distribution. With this assumption, the expression $\sum_{k=1}^{n} e_k^2 / \sigma_k^2$, where e_k is the error at every pixel and σ_k is

the standard deviation of that error, has a χ^2 probability distribution [14]. This expression will become useful in the derivation of the method, and the implementation algorithm. The standard deviation of the error at every pixel can be measured for the imaging system, for example, by making repeated measurements of a white screen (or any spatially constant background that does not change between measurements).

With these statistical assumptions of the measurement errors, the maximum entropy restoration method is outlined in the following steps:

1. Determine the value needed to obtain a confidence level close to 1 (say, 0.99) in the χ^2 probability distribution function with $\nu = m$ degrees of freedom. That is, obtain the value of χ^2 that yields $P(\chi^2|m) = 0.99$ in the χ^2 distribution function:

$$P(\chi^2|\nu) = \frac{1}{2^{\nu/2}\Gamma(\nu/2)} \int_0^{\chi^2} t^{\frac{\nu}{2}-1} e^{\frac{t}{2}} dt \qquad (7.3)$$

The solution for χ^2 can be found in several ways: numerically, that is, with the help of a computer; from asymptotic approximations (e.g. Severo and Zelen [15]); or if m is relatively small (< 100), the χ^2 can be found using tables (e.g. Spiegel [16]). The result is stored in the variable Ω. If the error has zero mean, then

$$\sum_{k=1}^m \frac{e_k^2}{\sigma_k^2} = \Omega \qquad (7.4)$$

2. Determine the total intensity γ received by the original image f. Using the assumption that h does not lose information (in Equation 7.2), γ is found by adding the total intensity received through the imaging system in g, and thus

$$\gamma = \sum_{i=1}^n f_i \qquad (7.5)$$

3. The only admissible solutions f_i are those that satisfy equations 7.2, 7.4, and 7.5. From these admissible solutions, select the one that maximizes the Shannon entropy

function

$$S = -\sum_{i=1}^{n} f_i \log(f_i) \tag{7.6}$$

7.2.2 The restoration algorithm

The Lagrange multiplier method is used to maximize equation 7.6, subject to constraints 7.2, 7.4, and 7.5. The Lagrangian L of the system is

$$
\begin{aligned}
L(f_1, ..., f_n, e_1, ..., e_m, \lambda_0, ..., \lambda_m, \mu) =\ & -\sum_{i=1}^{n} f_i \log f_i - \lambda_0 \left(\sum_{i=1}^{n} f_i - \gamma \right) \\
& -\sum_{k=1}^{m} \lambda_k \left(\sum_{i=1}^{n} h_{ik} f_i - g_k - e_k \right) \\
& -\mu \left(\sum_{k=1}^{m} \frac{e_k^2}{\sigma_k^2} - \Omega \right)
\end{aligned}
\tag{7.7}
$$

To maximize L with respect to the unknowns f_i and e_k, their partial derivatives $\partial L / \partial f_i$ and $\partial L / \partial e_k$ are set to zero. After some algebra, partial differentiation gives the following equations for f_i and e_k

$$\log f_i = -1 - \lambda_0 - \sum_{k=1}^{m} \lambda_k h_{ik} \, , \quad i = 1, ..., n \tag{7.8}$$

$$e_k = \lambda_k \frac{\sigma_k^2}{2\mu} \, , \quad k = 1, ..., m \tag{7.9}$$

Using Equation 7.5, λ_0 can be eliminated from Equation 7.8. After rearranging, this substitution yields

$$f_i(\lambda_1, ..., \lambda_m) = \gamma \frac{\exp\left(-\sum_{k=1}^{m} \lambda_k h_{ik} \right)}{\sum_{p=1}^{n} \exp\left(-\sum_{k=1}^{m} \lambda_k h_{pk} \right)} \tag{7.10}$$

The above expression for f_i now contains only m variables, and can be substituted into Equation 7.2 to yield

$$\sum_{i=1}^{n} h_{ik} f_i(\lambda_1, ..., \lambda_m) - \lambda_k \frac{\sigma_k^2}{2\mu} - g_k = 0 \, , \quad k = 1, ..., m \tag{7.11}$$

Substituting Equation 7.9 into Equation 7.4 gives

$$\frac{1}{4\mu^2} \sum_{k=1}^{m} \lambda_k^2 \sigma_k^2 - \Omega = 0 \tag{7.12}$$

Equations 7.11 and 7.12 represent the system of $m + 1$ equations to solve for the Lagrange multipliers λ, and thus for the true image g.

7.2.3 Iterative method for finding λ

The practical implementation of the maximum entropy method to restore the SSPX images is described below. This implementation is adapted from notes by Bellan [7] on maximum entropy methods. It should be noted that Wilczek and Drapatz used a Newton iteration method to solve the system of equations derived in the previous section. However, this method could be computationally expensive. The system of equations derived in the application of Wilczek and Drapatz involved about 10^2 different values of λ (unknowns), which can be solved in a reasonable amount of time and with enough stability in modern computers. However, the plasma images taken at SSPX had about 10^6 pixels, and thus the same number of unknowns. For this reason, it was decided against a Newton iteration method, and in favor of an iterative scheme that took advantage of pre-programed matrix operations in commercial software like Mathematica [17] or IDL [18]. Tensor notation is more appropriate than single indexing in this case. Nevertheless, single indexing will be used in the expressions below for consistency with the expressions derived in the previous section.

The procedure now is to start off with an initial guess for all λ_k and μ. For λ_k the choice was

$$\lambda_k^0 = \log(f_i + \varepsilon) \tag{7.13}$$

where the arbitrary value $\varepsilon << \min(f_i)$ was added to prevent indeterminate values if f_i was zero. The choice for μ was

$$\mu^0 = \frac{1}{\Omega} \sum_{i=1}^{n} \log(f_i + \varepsilon) \tag{7.14}$$

where ε has the same purpose as in Equation 7.13. These choices yielded a fast convergence of the algorithm, although almost any choice did, since the iterative scheme was robust in this sense.

Solving for the Lagrange multiplier μ in Equation 7.12 gives

$$\mu = \frac{1}{2} \sqrt{\sum_{k=1}^{m} \frac{\lambda_k^2 \sigma_k^2}{\Omega}} \tag{7.15}$$

The linear λ_k term in Equation 7.11 suggests that the expression can be solved iteratively. Substituting Equation 7.15 into 7.11 and solving for the linear λ_k term, the iteration expression is obtained

$$\lambda_k^{new} = \frac{2\mu^{old}}{\sigma_k^2} \sum_{i=1}^{n} h_{ik} f_i(\lambda_1^{old}, ..., \lambda_m^{old}) - g_k \tag{7.16}$$

For the iteration of μ, Equation 7.15 is modified to give

$$\mu^{old} = \frac{1}{2} \sqrt{\sum_{k=1}^{m} \frac{\left(\lambda_k^{old}\right)^2 \sigma_k^2}{\Omega}} \tag{7.17}$$

This iteration method was found to converge to in about ten iterations. Examples of image restoration using this iterative scheme and measured h (PSF) are presented in the section below.

7.3 The point-spread function and image restoration

Measurements of point-spread functions (PSF) for the SSPX high-speed imaging system and some examples of image restoration, are presented in this section. The PSF, that is, the amount by which the signal from a single pixel is spread over adjacent pixels, may cause
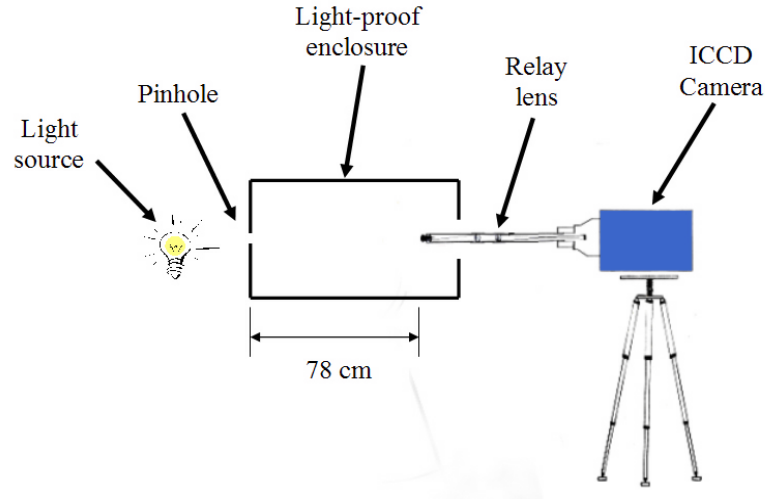
Fig. 7.1. Setup for the PSF measurements. The second generation relay lens and the double-branch fiber bundle were measured with this setup. With the lens inside the enclosure, the only light allowed was through the pinhole.

undesired blurring and inaccuracies in an image. Knowledge of the PSF is essential for the restoration of images using the maximum entropy method described in the previous section.

7.3.1 The point-spread function

Two different PSF measurements are presented here. The first measurement corresponds to the second generation relay lens, and the second to the double-branch fiber bundle (Chapter 4). To measure the PSF of both optical systems, a light-proof enclosure with a 100 μm pinhole was built. A strong light source was placed outside the box to create a 'point source' inside the box. The wide angle lens in both cases was placed 78 cm away from the pinhole, as shown in Figure 7.1. The distance between the lens and the pinhole was chosen such that the pinhole diameter would be equal or less than the size of a pixel in the final image.
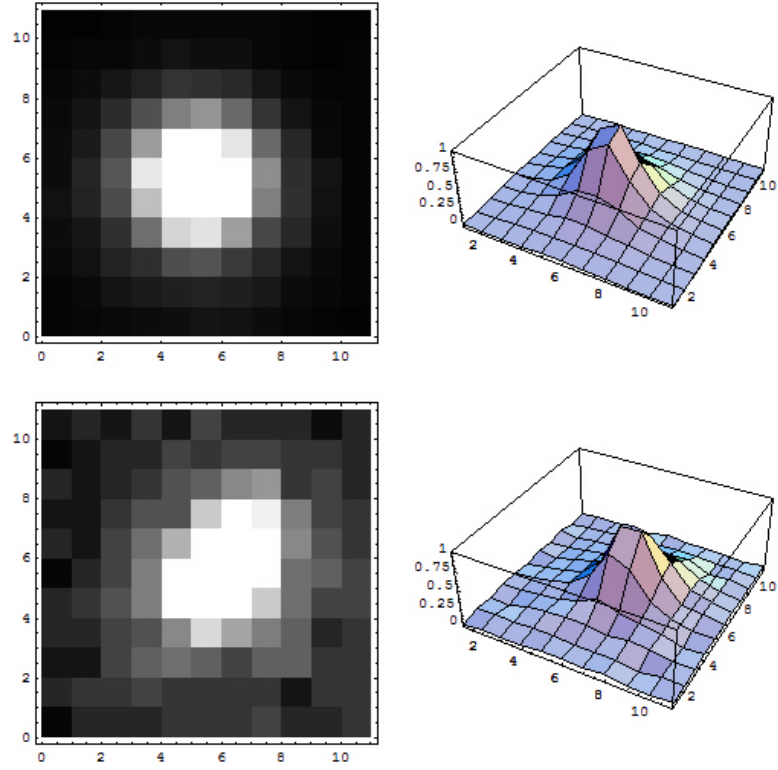
Fig. 7.2. Point-spread function (PSF) measurements for the second generation relay lens (top) and the double-branch fiber bundle (bottom).

The measurements on both cases were done with a 10% gain on the micro-channel plate (MCP) and exposures of 150 ms (to increase the signal to noise ratio). The results are shown in Figure 7.2. The values were saved as matrix arrays for later use as the h functions in the maximum entropy restoration method. Note that the PSF from the second generation relay lens seems to spread out more than the PSF for the double-branch fiber bundle. However, plasma images showed that the best quality obtained was from the relay lens. The difference could be in the amount of stray light that was generated in the different systems. The density plots shown in Figure 7.2 have high signal-to-noise ratios (compared to plasma images). However, the integration time for these images was much longer than for the plasma images.

It should be mentioned that these PSF measurements were done only for pixels at the center of the screen. At the edges there were distortions caused by the wide-angle lenses. Nevertheless, these regions of higher distortions usually fell outside the field of view where plasma was seen, and thus normally were not taken into account.

7.3.2   Image restoration using the maximum entropy method

The maximum entropy method described above was used to restore SSPX plasma images. Two examples are presented here. No other processing, e.g. coloring or filtering, was done to these images, and the restoration was done at the original resolution. The standard deviation σ of the noise, required for the iteration equations 7.15, 7.16, and 7.17, was not measured for all gain ranges of the MCP. However, by measuring σ for a small area in each image (usually an area not illuminated by the plasma), and assuming that σ is constant for all the pixels and MCP gain levels, then $\sigma \approx 1$ was considered a good approximation.

The first restoration example is for an image taken with the first generation relay lens (Chapter 3), and is shown in Figure 7.3. The original image is shown on top, and the restored image at the bottom. The major features (the plasma column, the opening at midplane, the bright spots, etc.) are seen on both images. However, the restored image shows finer and sharper details. This level of image definition was achieved after twelve iterations in the restoration method. Note that the PSF measured for the second generation relay lens (shown at the top of Figure 7.2) was used for the image in this example[4], which was taken with the first generation relay lens, and seems to have worked well. Images taken with the second generation relay lens and restored with the maximum entropy method have similar results as the one shown here. However, this example was chosen to show the

---

[4]   We were unable to measure the PSF for the first generation relay lens, since parts of it were 'canibalized' and modified to construct the second generation relay lens.
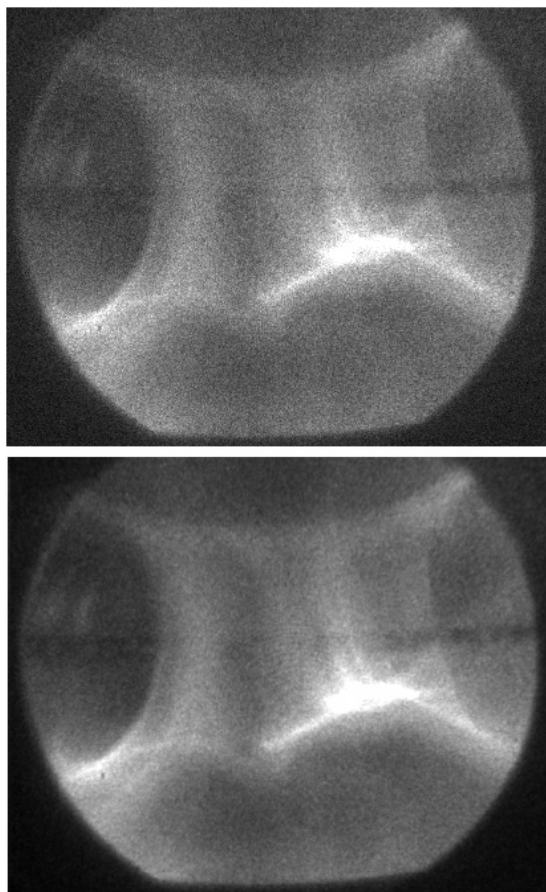
Fig. 7.3. Restoration of an image taken with the second generation relay lens. Shown here is the image before restoration (top), and after restoration (bottom) with the maximum entropy method. Shot 8181. $t = 55\,\mu s$. Gas used: hydrogen.

efficacy of the restoration method with an image that is particularly noisy, but contains sharp column edges.

The second example is for an image taken with the double-branch fiber bundle. The procedure and number of iterations were the same as in the previous example, but the PSF (shown at the bottom of Figure 7.2) was measured specifically for this optical system. The result is shown in Figure 7.4. Just like in Figure 7.3, the main features are seen on both the original and the restored images, but the restored image is cleaner and shows a sharper
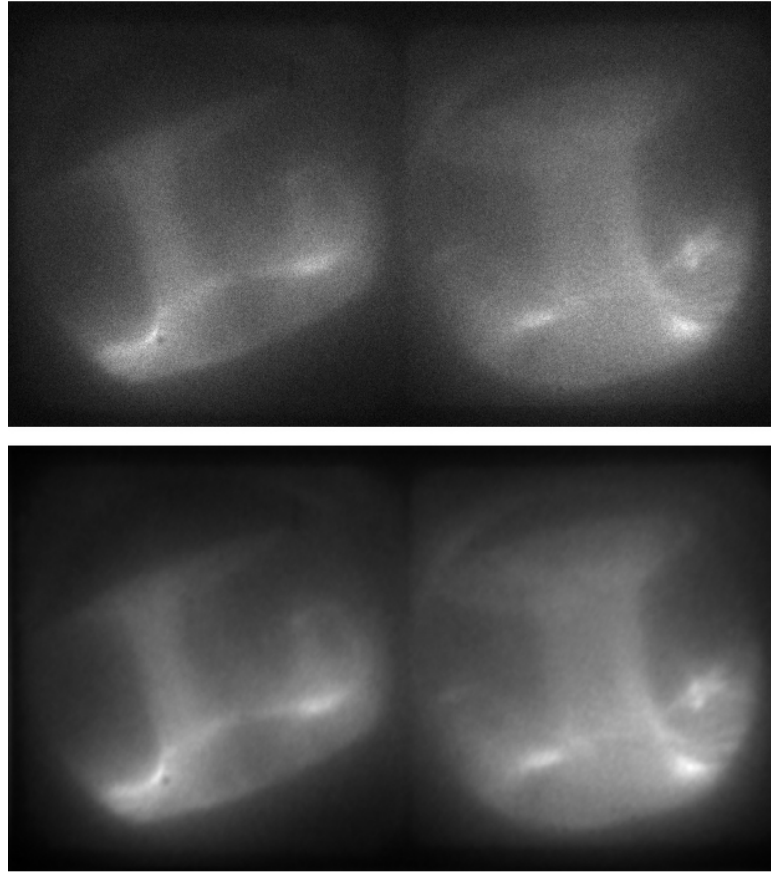
Fig. 7.4. Restoration of an image taken with the double-branch fiber bundle. Shown here is the image before restoration (top), and after restoration (bottom) with the maximum entropy method. The left image was taken from the $157.5\,^\circ$ port in SSPX, and the right image from the $270\,^\circ$ port. The rotation of each view is due to rotation of the fiber branches inside the ports. Shot 10375. $t = 50\ \mu s$. Gas used: hydrogen.

boundary of the central column. This is useful for the purpose of computer tomography, as will be shown in the following section.

7.4 Two-dimensional tomography of the SSPX transient plasma column

Tomography of the SSPX transient plasma column, and the method used to compute it, are presented in this section. The method is based on a novel extension of the maximum en-

tropy restoration method presented in Section 7.2. The method was created to reconstruct the cross-section of the SSPX plasma from images taken with the double-branch fiber bundle, which provided only two views per shot (e.g., Figure 7.4). This two-view limitation is in contrast with conventional (mostly medical) applications of tomography, in which dozens or hundreds or more views are available for high-fidelity reconstruction. For the method presented here, however, the availability of only two views imposes limitations on the resolution and complexity of the shapes that can be reconstructed. Thus, rather than pursuing precise reconstructions, the method is tailored to investigate changes in position and width of the column (or other features) from coarse reconstructions.

It should be noted that plasma tomography has been done before in plasma chambers with a reduced number of views (see for example [19–23]), including one that used a maximum entropy method [22]. However, the method presented here takes advantage of the image restoration algorithm presented above, such that only slight modifications to that algorithm are required to obtain a tomographic algorithm.

The method, the limitations, and some examples, are presented in the following sections.

7.4.1   The tomographic method

The first step in the tomographic method is to create a reconstruction grid. It is convenient to make this grid such that it follows the rays that map to both cameras (or detectors). This is illustrated in Figure 7.5. The grid cells do not have equal areas, and thus do not have equal weight when assigning intensity values in the reconstruction space. To give the cells equal weight, the area of each cell is calculated and stored in a weight matrix W.

The grid cells that fall outside the field of view (FOV) of one camera need to be included if they fall within the FOV of the other camera. Note that no grid cells are included
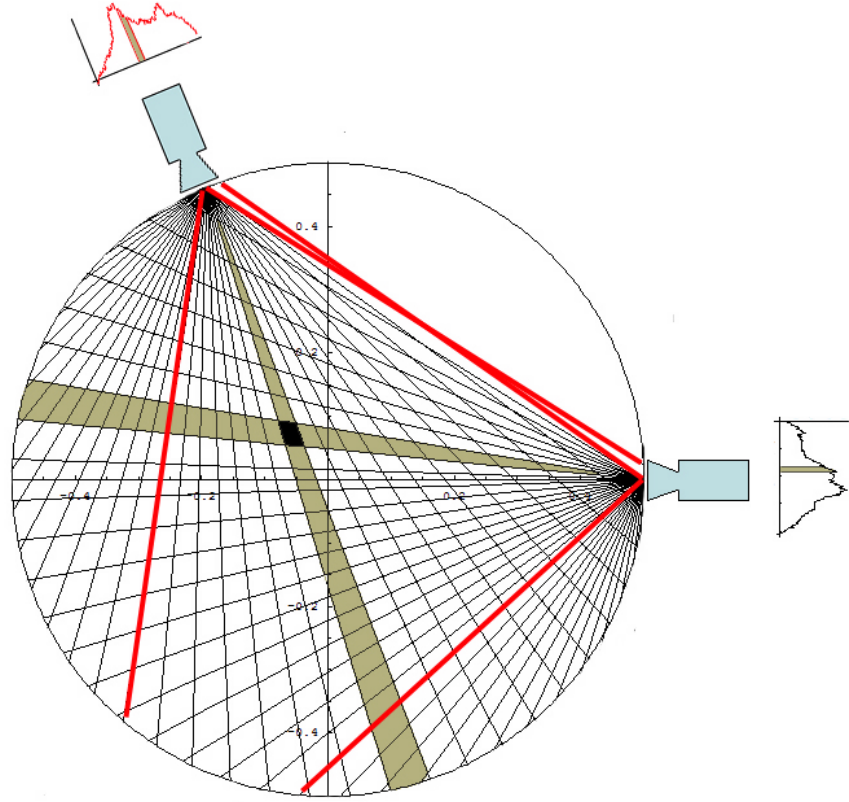
Fig. 7.5. Two-dimensional tomographic grid. The reconstruction area only where the rays intersect inside the circumference (flux conserver). The cameras, placed immediately outside the circumference, capture the information that is then projected and combined ray by ray back into the reconstruction area. The thick (red) lines represent the field of view (FOV) of both cameras.

if they fall outside both FOVs. In Figure 7.5, the FOV of each camera is marked with thick (red) lines. If both cameras have the same FOV and resolution (number of pixels), the W matrix is simply a triangular matrix. The assignment of the grid cells and their reconstruction weight is done only once for a given angle between the two views.

The second step in this method is to combine the data from the two views and situate it in the reconstruction grid. This is done with the summation method, which is finding the intersection of two rays from two views and assigning the sum of the projected values to the grid cell where both rays intersect. For example, if the ith ray, g_i^1, from the first camera
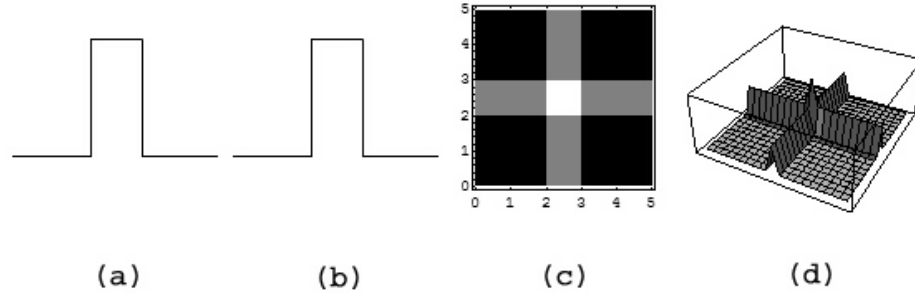
Fig. 7.6. The point-spread function (PSF) created by the summation method. The signals received by two perpendicular detectors (a) and (b) from a point source, are combined to produce a 'smeared' reconstruction (c) of the point source. The PSF for this case is shown in (d).

is being combined with the jth ray, g_j^2, from the second camera, then the combination matrix G is assigned the value $g_i^1 + g_j^2$ at cell G_{ij}. The summation of two rays is shown in Figure 7.5 with two shaded rays. The cell at which both rays intersect (darker cell in the figure) is assigned the sum of the intensity from both rays. Rays that fall outside the FOV of one camera are assigned the intensity value of zero for that camera. This is a sort of zero-padding to make the G matrix rectangular.

The third step is to create a point-spread function (PSF). This PSF serves the same function as the one in the sections 7.2 and 7.3. However, in this case the PSF is not created by cameras or detectors, but by the summation method used to populate the G matrix. Thus, in this method the PSF could be considered a 'numerical' PSF, since the summation method spreads the signal from a point over the range of the rays that capture the signal. This spreading is shown in Figure 7.6. Indeed, the PSF shown in this figure was used for all the reconstructions presented in this chapter.

The tomographic method now follows the same steps as for the maximum entropy restoration derived in the previous section. In this sense, the G matrix is like an image that needs restoration, and the PSF is known for that image. However, unlike the PSFs

measured in Section 7.3, here the PSF spreads the information over a wider range in the image (i.e., the G matrix). This wider spreading imposes a limitation for restoration, since it is equivalent to trying to restore an image that is extremely blurred. Another limitation comes from the number of projections. It is possible that features in the reconstruction plane were blocked from the two cameras by other features during data acquisition. Thus, these hidden features cannot be resolved from only two projections.

With these limitations, it is clear that this method is not appropriate if high-fidelity reconstruction is desired. However, the coarse reconstruction resulting from this method is useful in finding the position of features like the transient central column or thick filaments that might be present. Even though the sustainment central column (Chapter 5) falls within this category of features, it was unfortunately not possible to reconstruct it because of the low contrast[5] (caused by a highly ionized plasma) near midplane.

It is worth mentioning that the summation method can be extended to more than only two projections. In this case, a PSF would have to found based on the angle and number of the projections. For example, if there are five projections, the PSF would be a star shaped version of the one shown in Figure 7.6. However, the grid generation would be different from the one presented here. Details of the extension to more than two views are out of the scope of this chapter, and the interested reader is referred to the work of Holland and Navratil [22], and Terry et al. [19], for a discussion about the generation of a grid for a few projections. Of course, if many projections are available, more conventional methods are advisable for tomographic reconstruction.

---

[5] Low contrast is a common problem for other tomographic techniques [24].

7.4.2 Tomographic reconstruction

Examples of reconstructions using the tomographic method described above, and its limitations, are presented in this section. To test the method, a number of reconstructions using simulated signals were made. The results are shown in Figure 7.7. Columns (a) and (b) represent the simulated signals received by two detectors positioned $112.5°$ apart, just like the detectors shown in Figure 7.5. The simulated signals are Gaussian functions, and are shown in column (c). The tomographic reconstructions with the input signals from columns (a) and (b), are shown in column (d). Two hundred beams were used for each detector.

The first striking difference between the original Gaussian contours and the reconstructed ones, is the distortion of the contours. This is inherent to the summation method and the irregular grid used. That is, there is only a limited amount of spread caused by the summation method that can be corrected with the PSF used in the maximum entropy restoration method.

Note that all the Gaussian functions are identical. These functions simulate dense plasma filaments with identical characteristics, all within the FOV of both detectors. When the signals are integrated (along the line of sight of each detector) and recorded by the hypothetical detectors, it might not be evident that all the signals have the same characteristics or that the number of peaks seen in the detectors correspond to the number of hypothetical columns. In fact, the layout of these columns was chosen such that some would overshadow others.

The layout of these simulated signals is considered a 'tough' test for the reconstruction method. The limitation in the number of features that can be reconstructed is evident from these tests, since lower contrast (or less contours in the reconstructed figures) results as the number of features in the reconstruction area increases. For example, the recon-
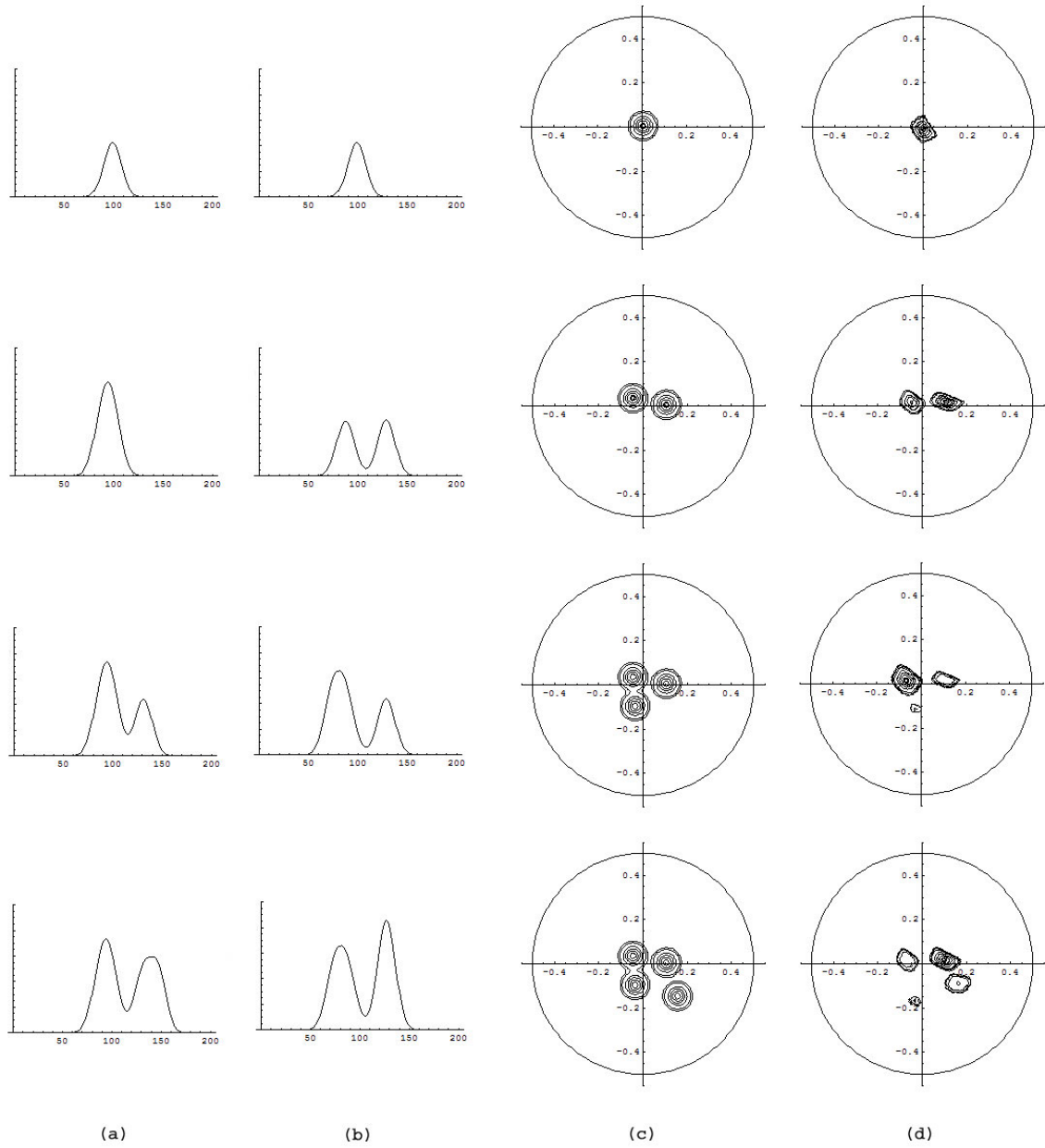
Fig. 7.7. Comparison between simulated reconstructions. See text for details.

structed cross-sectional image in the second row of Figure 7.7 show clearly the contours for two columns. However, the reconstruction for three columns shows only two that are of significant intensity, and a third column that is very faint. The small contours represent less than five percent of the maximum intensity after reconstruction.

Another problem that may occur when reconstructing cross-sections with multiple features, is the confusion in their position. This is shown in the last row in Figure 7.7, which shows the test for four columns. The reconstruction is not only faint for some of the columns, but it is also inaccurate in their position.

Based on the above tests, it was accepted for the present work that the position and contrast of features was accurate for a maximum of two features, to within $2\,\mathrm{cm}$ (not counting the deformation of the features). With these limitations in mind, the cross-section of features visible by the high-speed imaging system through the double-branch fiber bundle, were reconstructed for the midplane section. An example is presented here using the images shown in Figure 7.4. Of course, the restored version of these images was used for this reconstruction. After digitally rotating the images, a row of pixels was taken from each image. These rows of pixels are the input signals for the reconstruction algorithm (just like columns (a) and (b) in Figure 7.7).

The result from this reconstruction is shown in Figure 7.8. It is possible that due to the limitations mentioned above, the actual shape of the sustainment central column was not exactly as it appears in the figure. Nevertheless, it is clear that the column is not centered at the axis of the flux conserver. This is perhaps also apparent from the full images. However, there is no depth perception from these images, and thus it is not possible to measure the location of the column this way. Therefore, the reconstruction method presented here might be useful in characterizing the position and size of the transient plasma column (Chapter 4) in the SSPX discharge.
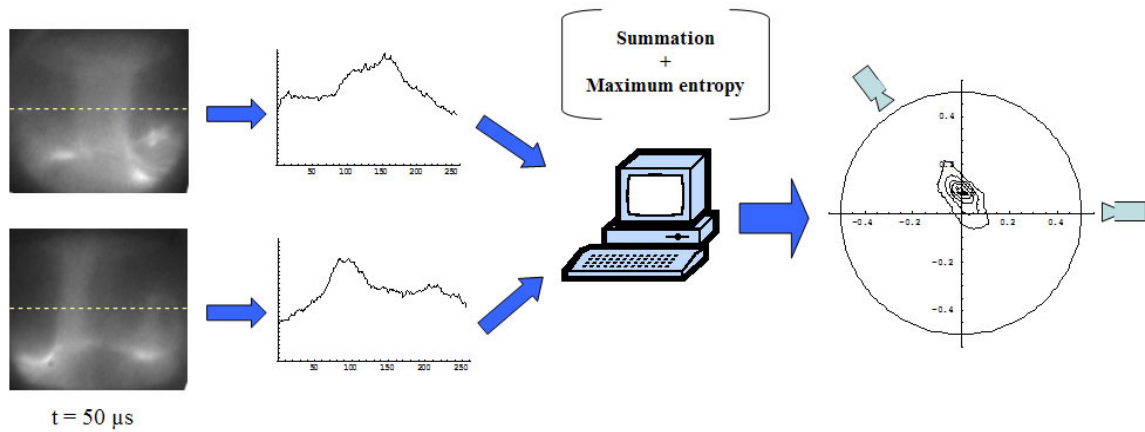
Fig. 7.8. Cross section reconstruction of a transient central column at midplane. A row of pixels is selected from the midplane section on both images. Using the reconstruction method detailed in this chapter, the approximate position and size of the plasma column is found. The position of the views is indicated outside the reconsruction diagram on the right. The circumference depicts the boundary of the SSPX flux conserver.

7.5 References

[1]   E. Hecht and A. Zajac. *Optica*, (Addison-Wesley Iberoamericana S. A., Mexico, 1986), pp. 185 - 204.

[2]   S. E. Umbaugh, *Computer vision and image processing, a practical approach using CVIP tools*, (Prentice Hall PTR, Upper Saddle River, 1998), Chapters 3 and 4.

[3]   G. X. Ritter and J. N. Wilson, *Handbook of Computer Vision Algorithms in Image Algebra*, (CRC Press, New York, 2001), Chapter 2.

[4]   S. E. Reichenbach and S. K. Park, IEEE Trans. Signal Processing **39**, 2263 (1991).

[5]   C. L. Fales, F. O. Huck, J. A. McCormick, and S. K. Park, J. Opt. Soc. Am. A **5**, 300 (1988).

[6]   R. Wilczek and S. Drapatz, Astron. Astrophys **142**, 9 (1985).

[7]   P. M. Bellan, Personal communication, June 25, 2003.

[8]   B. R. Frieden, J. Opt. Soc. Am. **62**, 511 (1972).

[9]   E. T. Jaynes, Phys. Rev. **106**, 620 (1957).

[10] E. T. Jaynes, Phys. Rev. **108**, 171 (1957).

[11] S. F. Gull and G. J. Daniell, Nature **272**, 686 (1978).

[12] S. Webb, *The physics of medical imaging*, (IOP Publishing Ltd, Bristol, 1988), pp. 111 - 119.

[13] G. T. Herman, *Image reconstruction from projections, the fundamentals of computerized tomography*, (Academic Press, Inc., New York, 1980), pp. 108 - 110.

[14] W. W. Hines, D. C. Montgomery, D. M. Goldsman, C. M. Borror, *Probability and Statistics in Engineering, fourth edition*, (John Wiley and Sons, Inc., Hoboken, 2003), pp. 205 - 208.

[15] N. C. Severo and M. Zelen, Biometrika **47**, 411 (1960).

[16] M. R. Spiegel, *Manual de fórmulas y tablas matemáticas*, (McGraw Hill, Mexico, 1991), p. 259.

[17] Mathematica 5.0, Wolfram Research, Inc., http://www.wolfram.com/, August 20, 2004.

[18] IDL Software, Research Systems, Inc., http://www.rsinc.com/idl/, August 20, 2004.

[19] S. D. Terry, D. Q. Hwang, H. S. McLean, et al., Rev. Sci. Instrum. **71**, 4119 (2000).

[20] Y. Nagayama, S. Tsuji, K. Kawahata, et al., Jpn. J. Appl. Phys. **20**, 779 (1981).

[21] R. S. Granetz and P. Smeulders, Nucl. Fusion **28**, 457 (1988).

[22] A. Holland and G. A. Navratil, Rev. Sci. Instrum. **57**, 1557 (1986).

[23] Y. Liu, A. Yu, and B. J. Peterson, Rev. Sci. Instrum. **74**, 2312 (2003).

[24] S. Webb, *The physics of medical imaging*, (IOP Publishing Ltd, Bristol, 1988), pp. 94 - 96.

Chapter 8

Multielement magnetic probe using commercial chip inductors

(Note: This chapter was published by C. A. Romero-Talamás, P. M. Bellan, and S. C. Hsu[1], in Review of Scientific Instruments, Volume 75, August 2004, pp. 2664 - 2667.)

8.1 Introduction

Magnetic probes are widely used in measurements of current-carrying plasmas [1, 2], but multi-element and compact arrays are often difficult and tedious to make when winding coils manually [3–5]. The part-to-part uniformity of hand-wound, millimetric size coils is usually poor since it is difficult to keep the wire aligned for every turn. Alignment and separation between coils can also become difficult if there is no substrate or fixture on which to mount the coils.

To give an idea of the difficulties in fabricating millimetric size coils, we compare the pick-up coils used in our probe, to those used in probes reported by Granetz et al. [6] and Takahashi et al. [7]. Hand-winding 3 cm x 8 mm coils with #30 AWG wire (as reported by Granetz et al.), is very different from hand-winding 2.9 mm x 2.0 mm coils with a wire of size #42 (used in our probe). The diameter of a #30 wire is 0.254 mm, and the diameter of a #42 wire is 0.0635 mm, therefore the cross-sectional area of a #42 wire is 16 times smaller than that of a #30 wire and consequently the mechanical strength is also much smaller. Wire of #42 size can easily break if pulled too hard by hand. Takahashi et al.

---

[1] Current address: P-24 Plasma Physics Group, Los Alamos National Laboratory, NM 87545.

present a novel way of fabricating induction coils using thick-film technology. However the dimensions per coil that they used are too big (of the order of $1 - 2\,\mathrm{cm}$) to create a multi-element and compact array probe, especially if the probe is to be immersed in the bulk plasma.

The probe array presented here is designed for use in spheromak research, and has a combination of off-the-shelf components and custom computer-designed parts. The custom parts were machined to high precision with numerically controlled machine tools using information from computer-generated drawings. The coils are commercial chip inductors with precise dimensions and excellent consistency. The probe has a modular design for easy assembly and mounting on the chamber, and for easy component replacement if necessary.

Spheromaks [8] are self-organizing, toroidal, axisymmetric magnetohydrodynamic configurations in which the magnetic fields are produced almost entirely by currents flow-ing in the plasma. Although spheromak research is geared mainly to achieve the goal of thermonuclear fusion, spheromak physics is also relevant to the study of how plasma mag-netic topology evolves.

At Caltech, spheromaks are created in a large cylindrical vacuum chamber using a planar gun [9] (see Figure 8.1). Since spheromaks in the Caltech chamber expand freely and translate away from the gun, a magnetic probe can be fixed in front of the gun; the recorded signals can then be combined to produce contour maps of the spheromak as it flows past the probe [10].

8.2 Design and construction

Sixty commercial chip inductors with fifty-two turns each (inductance $= 5 \pm 0.1\,\mu\mathrm{H}$) were used (Coilcraft Inc., model 1008CS-472XGBB). The nominal dimensions of the chip in-

Fig. 8.1. Cutaway view of the Caltech vacuum chamber. Magnetic probe (labeled B-dot) is placed in front of the planar spheromak gun. The spheromak gun is 50.8 cm in diameter, and the chamber dome is 137 cm in diameter.
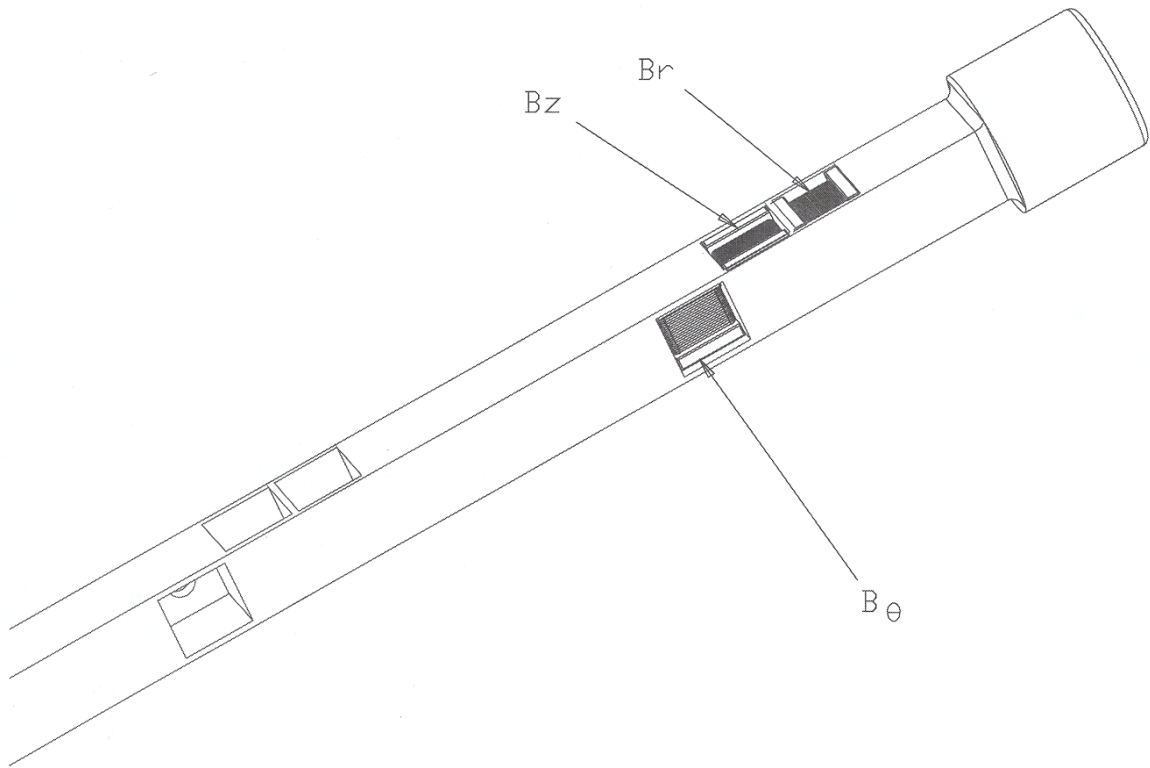
Fig. 8.2. Plastic retention fixture for induction coils. Two clusters are shown. The cluster on the right contains the inductor coils, with the direction of the B field that they measure indicated.

ductors are $2.8\,\mathrm{mm} \times 2.9\,\mathrm{mm} \times 2.0\,\mathrm{mm}$. The inductors were inserted into a Delrin plastic retention fixture that was fabricated to precise specifications using numerically controlled machining (see Figure 8.2). The spacing between clusters is $20\,\mathrm{mm}$; thus the effective probe length is $380\,\mathrm{mm}$.

Pairs of twisted magnet wires (38-gauge) were soldered to the terminals of the inductors. Each twisted pair of wires connects to a BNC panel jack, and the signal of each coil is recorded using 100 MHz, 12-bit analog to digital converters (ADC). The soldering of the wires was done manually using a precision jig made to hold the wires in place on top of

each terminal during the soldering operation. A special grinding machine (Carpenter Mfg. Co., model 88-D) was used to strip the insulation enamel from the wires.

Teflon tape was wrapped around the subassembly of the plastic fixture, chip inductors and magnet wires to prevent damage during the insertion of the assembly into its housing. The housing was made of quartz tubing to prevent electrical interaction with the plasma. The coils, plastic fixture, and wiring remain at atmospheric pressure, since the housing is vacuum tight. The probe diameter is $8.4\,\mathrm{mm}$.

To connect the quartz tube to the rest of the housing, Torr-seal vacuum epoxy was used to fix the quartz tube to a standard Swagelok VCO socket gland. A tight fit of the plastic fixture into a Swagelok elbow prevents the subassembly from rotating after assembling the probe and tightening the vacuum seals. The coil cables were soldered to three 20×2-pin insulation displacement connector sockets (3M, model 517-89140-0001), which were then inserted into a metal box that serves as an EMI shield and panel for the BNC connectors.

The mechanical support of the probe is achieved through a $1\,\mathrm{in}$ diameter, highly polished stainless steel tube. The tube is connected to the probe housing through a combination of standard Swagelok connectors and custom-made welded reducers. Once mounted on the vacuum chamber, the probe can slide in the Z direction and also rotate in the θ direction. The vacuum seal is achieved by an O-ring seal around the $1\,\mathrm{in}$ diameter tubing, mounted on a $2.75\,\mathrm{in}$ flange. A high-precision, double linear bearing (McMaster-Carr, model 64825K87) mounted on the outside of the chamber assures that the $1\,\mathrm{in}$ diameter tubing remains parallel to the Z direction (see Figure 8.3). The double linear bearing also relieves the O-ring seal from any load that could result from the weight of the probe and the $1\,\mathrm{in}$ diameter tube. Even though the entire probe assembly is very rigid, care was taken to ensure that the probe position would not be affected by deflection or sagging from the
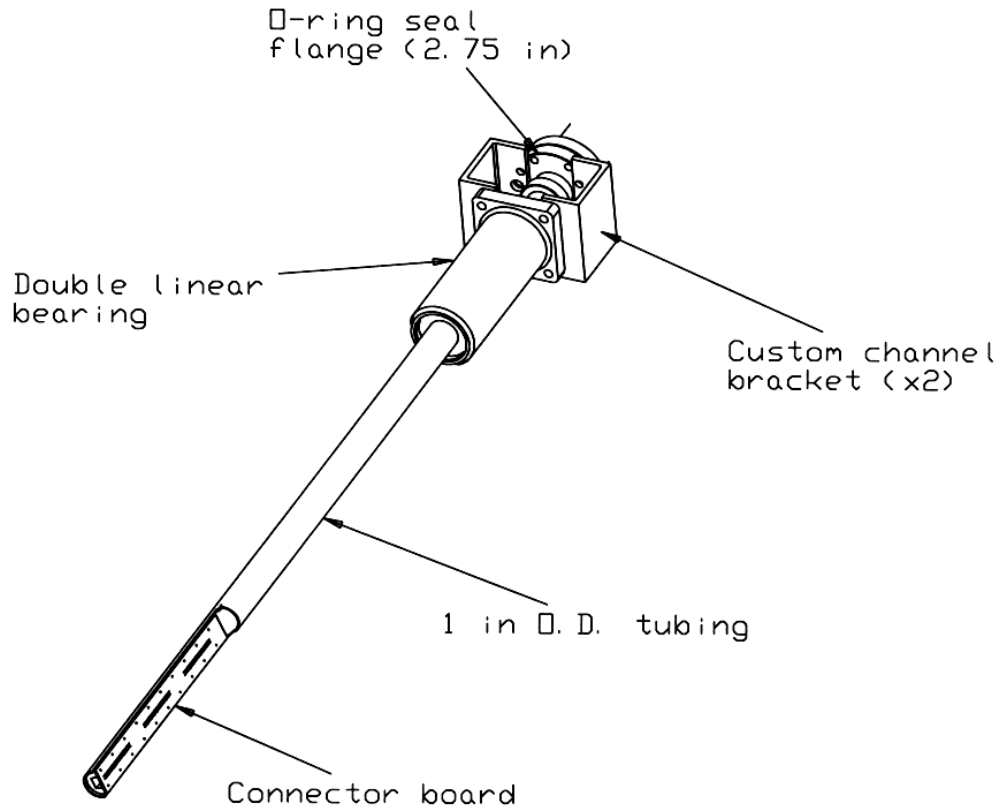
Fig. 8.3. External view of the magnetic probe mounted on the Caltech vacuum chamber. The 2.75 in. O-ring seal flange is attached to the vacuum chamber flange. Note: Probe connectors and EMI shield not shown.

weight of the tubing or its connectors. Positioning measurements were carried out for the $50\,\mathrm{cm}$ range of motion required in our experiments. Positioning in the θ direction was measured with a tilt indicator attached to the $1\,\mathrm{in}$ diameter tubing at the outside of the vacuum chamber. In a $50\,\mathrm{cm}$ displacement range no deflection was detected, to within $1\,\mathrm{mm}$ precision in the positioning of the probe. All measurements were carried out with respect to the axis of the planar spheromak gun shown in Figure 8.1. Fiducial marks were placed on the tubing to facilitate alignment when moving the probe between experimental runs.

8.3 Operation principle and calibration

Using Faraday's law, the induced voltage in a loop of conducting material in the presence of a time-varying magnetic field is $V = -d\Phi/dt$, where Φ is the magnetic flux through the loop. If every coil has N turns with an area A, the induced voltage can be expressed as $V = -NA \, (dB/dt)$. For practical purposes, the values N and A can be lumped into one constant, which we will refer to as the NA value.

To obtain the NA value for every coil, a Helmholtz coil was used to produce a known magnetic field. Since the current through the Helmholtz coil is known, the expression for calibration becomes

$$NA = \frac{a \int_{t_o}^{t} V_{coil}(t')dt'}{\left(\frac{4}{5}\right)^{3/2} \mu_o n \left[I(t')\right]_{t_o}^{t}} \tag{8.1}$$

where a, $I(t)$, and n are respectively the Helmholtz coil radius, current, and number of turns, and $V_{coil}(t')$ is the voltage across the terminals of the pick-up coil.

For every cluster of coils, a calibration operator was defined for precise measurements, since it is possible that a given coil can pick up unwanted signal (i.e., different from the intended direction) at the interface between the soldered wire and the coil. The calibration operator subtracts the unwanted signals and is defined as follows

$$\mathbf{C} = \begin{pmatrix} 1 & -C_{R\theta} & -C_{RZ} \\ -C_{\theta R} & 1 & -C_{\theta Z} \\ -C_{ZR} & -C_{Z\theta} & 1 \end{pmatrix} \tag{8.2}$$

with the components of the operator defined as

$$C_{ij} = \frac{NA_j^{perp}}{NA_i} \tag{8.3}$$

with NA^{perp} being the NA value for the pick-up of a signal by a coil oriented perpendicular to the direction being measured (also the direction of the B field). The true field is then

$$\mathbf{B} = \mathbf{C} \cdot \mathbf{B}_m \tag{8.4}$$

where $\mathbf{B}_{m_i} = -1/NA_i \int_{t_o}^{t} V_i(t')dt'$.

The average value for the effective NA was found to be $1.21 \times 10^{-4}\,\mathrm{m}^2$ for the probe presented here. All the coils were absolutely calibrated in the probe assembly using a pulsed capacitor bank power supply that rings at 280 kHz. The relative uncertainty of the calibration system, including the power supply for the Helmholtz coil and the digitizers was 0.48%. The average absolute value for the off-diagonal elements of the calibration operator was found to be 0.076.

The relative difference of NA values between clusters was found to be 2.4% for the R-direction coils and 4.3% for the θ and Z-direction coils. The main reason for such variation in the θ and Z-direction coils is the small wire loop that results at the interface of each coil and its leads. Given the thin wire used, it was difficult to twist the wire tightly at the interface with the chip inductor without breaking the wire. In the R-direction the variation comes mainly from the inductance tolerance of the commercial chip inductors used.

The phase shift between the known magnetic field signal and the probe signal at the digitizers was also measured during calibration. The difference in phase between the two signals yielded a time lag in the probe current of 114 ± 17 ns. The electrical circuit for any given coil in the probe and its corresponding digitizer channel is shown in Figure 8.4. The equation for the coil current is

$$L\frac{dI}{dt} + I(R_d + R_c) = \phi_o \cos(\omega t) \tag{8.5}$$

where R_d is the digitizer and cable impedance ($50\,\Omega$), R_c is the coil and coil lead resistance ($12\,\Omega$), L is the inductance of the coil and I is the current through the circuit. The right hand side represents the voltage source due to the time dependent flux linked by the coil. This flux is due to the external magnetic field, $B \times NA$. The solution for the above equation
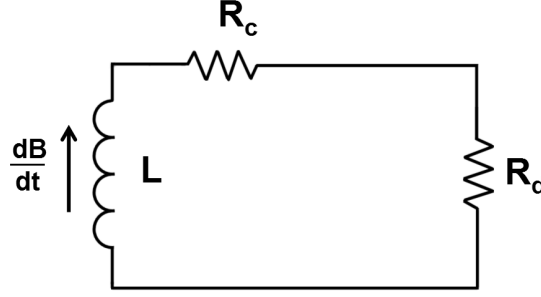
Fig. 8.4. Equivalent circuit for each coil in the magnetic probe, including the transmission line to the digitizer. Measured values are $L = 6.17\,\mu\text{H}$, $R_c = 12\,\Omega$ and $R_d = 50\,\Omega$.

can be written as

$$I(t) = \frac{\phi_o}{\sqrt{(R_d + R_c)^2 + \omega^2 L^2}}\cos(\omega t - \theta) \qquad (8.6)$$

with $\theta = \tan^{-1}(\omega L/(R_d + R_c))$ being the phase shift. For the values shown in Figure 8.4, $\theta = 0.173\,\text{rad}$, or equivalently a time lag in the signal of $\Delta t = 99\,\text{ns}$ is obtained.

8.4 Measurements

Figure 8.5 shows an example of the raw signal (dB/dt) and integrated signal (B) at a radius of 12 cm from the axis of the chamber (see Figure 8.1). The sampling time for the raw data is 0.01 μs, and the integration was performed numerically [11].

Using the Single Shot Propagation Inference (SSPI) method described by Yee and Bellan [10], it is possible to obtain approximate information on magnetic topology from a single discharge. Figure 8.6 shows a contour plot of data from the entire magnetic probe array; the contours represent surfaces of constant magnetic flux, $\psi(r, z_p) = \int_0^r 2\pi r' B_z(r', z_p)dr'$, where z_p is the axial coordinate in the frame of reference of the plasma. The propagation velocity of the plasma was estimated to be $V_p = 1.5\,\text{cm}/\mu\text{s}$ from images taken with a 16-frame, gated, intensified CCD camera (DRS Hadland Imacon 200). The probe was placed
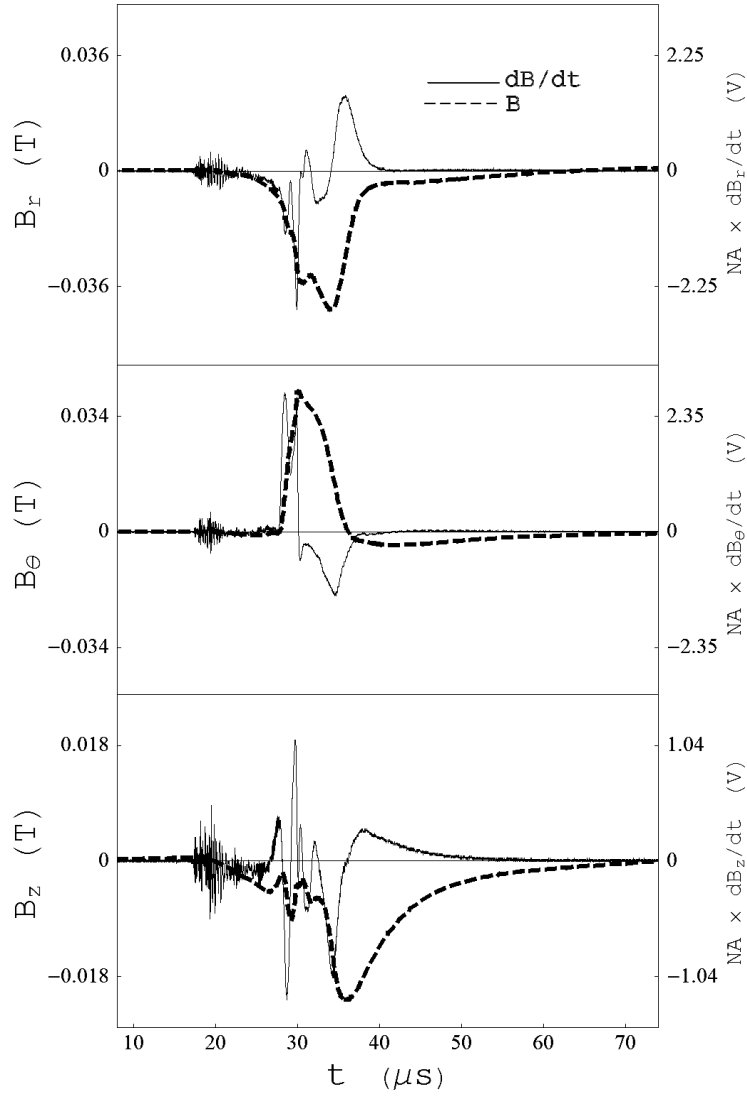
Fig. 8.5. Digitizer and integrated signals of the cluster found at $R = 12\,\mathrm{cm}$.
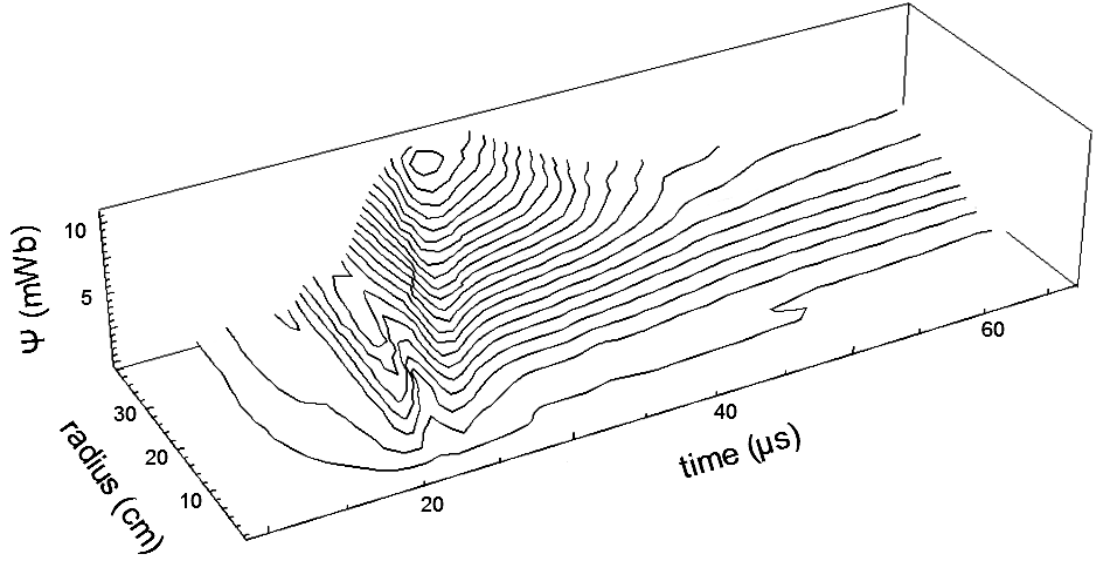
Fig. 8.6. Contours of constant ψ (in units of mWb). Contours are drawn along the vertical axis every 0.5 mWb. The top (closed) contour represents 10.6 mWb. The probe was placed 22.5 cm away from the planar gun. Shot #4855.

at $z = 22.5\,\text{cm}$ from the planar gun ($z = 0$). Assuming constant V_p and using the transformation $z_p = z - V_p t$, we find that the range of time shown in Figure 8.6, $10\,\mu\text{s}$ to $65\,\mu\text{s}$, corresponds to $97.5\,\text{cm}$ to $15\,\text{cm}$ (note that the direction of the distance axis reverses with respect to the direction of the time axis). Thus, the time axis in Figure 8.6 can be transformed to a distance axis to obtain spatial information of the magnetic flux along the Z direction .

8.5 Acknowledgments

8.6 References

[1] R. H. Lovberg. *Plasma Diagnostic Techniques*. R. H. Huddlestone and S. L. Leonard, Editors, (Academic Press, 1965, New York), Chapter 3.

[2] I. H. Hutchinson, *Principles of Plasma Diagnostics*, (Cambridge University Press, 1987), Chapter 2.

[3] D. E. T. F. Ashby, L. S. Holmes and M. A. Kasha, J. Sci. Instrum. **40**, 364 (1963).

[4] P. Beiersdorfer and E. J. Clothiaux, Am. J. Phys. **51** (11), 1031 (1983)

[5] Donald G. Pellinen et al., Rev. Sci. Instrum. **51** (11), 1535 (1980).

[6] R. S. Granetz, I. H. Hutchinson, et al., Rev. Sci. Instr. **61** (10), 2967 (1990).

[7] H. Takahashi, S. Sakakibara et al., Rev. Sci. Instr. **72** (8), 3249 (2001).

[8] P.M. Bellan, *Spheromaks: A practical application of magnetohydrodynamic dynamos and plasma self-organization* (Imperial College Press, London, 2000).

[9] S. C. Hsu and P. M. Bellan, Mon. N. Roy. Astron. Soc. **334**, 257 (2002).

[10] J. Yee, P. M. Bellan. Phys. Plasmas **7**, 3625 (2000).

[11] S. Wolfram. The Mathematica Book. Fourth Edition, (Cambridge University Press and Wolfram Media, 1999. New York), pp. 909-916.

Chapter 9

Summary and recommendations

9.1 High-speed imaging

The high-speed images, which captured the visible atomic radiation from the plasma and neutrals (see Appendix A), revealed unprecedented detail of the Sustained Spheromak Physics Experiment (SSPX) plasma. The images showed the presence of features, such as filaments, in various locations and times throughout the discharge. With the capability to take up to two images and to precisely time them (typically with respect to breakdown), it was possible to identify the movement of these filaments and electrode patterns at any given discharge. In some cases, it was also possible to measure their displacement and velocity. The camera has access to most of the volume where spheromaks are formed, since it has a wide angle view of the inside of SSPX and the plasma is optically thin for the most part of a typical discharge. Precise image timing also allowed the synchronization of images with other diagnostics. Thus, the high-speed imaging system provided not only a diagnostic in itself, but a complement to existing diagnostics at SSPX.

Thousands of images have been obtained with the high-speed imaging system. Three different stages were identified during the plasma shots according to the distinct plasma features observed. These stages are: breakdown and ejection, sustainment, and decay. During the breakdown and ejection stage, plasma comes out of the gun and into the flux conserver region in the first hundred microseconds after breakdown. A short-lived plasma column (oriented in the axial direction) is formed shortly after the plasma is first seen at

the flux conserver. After about five microseconds, the column bends and disappears seemingly merging with the toroidal plasma. This bending and disappearing seem to happen in less than one microsecond and proved to be extremely elusive to the camera, because the shot to shot reproducibility of features during this stage could be done to within two or three microseconds. Even when image timing was synchronized with the bending event, the plasma (either hydrogen or helium) became so highly ionized that no light could be captured by the camera shortly after the bending. How the plasma rearranges itself during that time continues to be a mystery, since the gun current flows uninterrupted.

During the sustainment stage, patterns on the end-face of the cathode (inner electrode) were observed to elongate consistent with the theory of $E \times B$ drifts (and possibly $J \times B$ forces). The pattern velocity was measured to be ~ 0.25 km/s in the toroidal direction, describing trajectories in the form of circular segments located at discrete radial locations on the surface of the cathode.

It is conjectured that if $E \times B$ drifts are responsible for the cathode pattern elongation, then the sustainment current profile is hollow. That is, most of the current flows at the edge of the sustainment central column in order for the patterns to move in a toroidal-only direction. It is also conjectured that the cathode patterns are caused by current filaments carrying relatively small amounts of current along open field lines inside the hollow profile. These conjectures contrast with the commonly assumed peaked current profile at the axis of the chamber. To the time of writing of this thesis, measurements of voltage, magnetic field, and current profile near the cathode surface, needed to identify the cause for the pattern drifts, have not been performed. A recommendation for future work is thus to measure these parameters locally and compare to the high-speed imaging findings. Understanding the cathode patterns could shed light in the formation and evolution of closed (and open)

magnetic flux surfaces, and in the engineering and geometrical considerations for future cathode designs.

During the sustainment stage, information from the high-speed imaging system has also been used to compare the width of the sustainment central column with the CORSICA code. The comparison showed that the CORSICA reconstructions are in good agreement with the measurements. The typical sustainment column radius is about 12 cm, increasing slightly towards the end of the sustainment stage. All the shots used for the comparison had very similar parameters and were created using the modified flux configuration. However, to fully benchmark the central column reconstruction of CORSICA (or any other MHD equilibrium code) using high-speed imaging measurements, a wider variation in the central column diameter is recommended (changing, for example, the flux configuration).

The sustainment stage ends when the current starts to ramp down. The decay stage then begins. At this last stage, the central column and the cathode patterns are still present. As the gun current decreases, the central column diameter increases and at some threshold (about 50 kA), the column breaks up into many filaments. No closed magnetic surfaces are expected after this break up. The cathode patterns also change, going from the long circular patterns seen during the sustainment stage, to a more segmented version resembling a 'string of pearls' in the decay stage. Future studies of this stage are recommended to include cathode measurements similar to those proposed during the sustainment stage, and investigations of the filamentation of the central column, which is relevant to magnetic reconnection.

The high-speed images were not free of noise and some blurriness. The noise was created mainly in the camera, and the blurriness in the optics. An algorithm based on the maximum entropy principle applied to information theory was implemented to restore the images. For the images presented here, the measure of restoration was subjective. However,

the results shown in Chapter 7 are considered good and acceptable improvements over the unrestored images. Many of the restored images were used in the cathode pattern and column diameter measurements.

The maximum entropy restoration method was modified to produce tomographical reconstructions of the transient column cross-section (at midplane) seen during the breakdown and ejection stage. The reconstructions are considered 'rough' because only two projections were available from the double-branch optical fiber bundle. Tests with simulated projections showed that, although the shape of the column could not be discerned accurately with only two projections, the location of the column in the flux conserver could be found within a few centimeters of error. Poor contrast in the projections was also a limitation on precise reconstructions. A recommendation for future work is to improve the projection contrast (using perhaps relay lenses instead of fiber bundles), and increase the number of projections. Detailed investigation of the transient column evolution (position, size, brightness, etc.) could shed light into the helicity injection process during that early stage in the plasma shots.

9.2 Multielement magnetic probe

The multielement magnetic probe presented in this thesis was designed and built using a combination of off-the-shelf and custom-made parts. The probe was installed at the Caltech Spheromak Experiment and has been used to investigate the magnetic topology and evolution of the unbounded spheromaks produced there. The linear array of miniature chip inductors yields three-dimensional information of the magnetic field that evolves with the plasma. It was shown here that using the Single Shot Propagation Inference method, it is possible to obtain approximate information on magnetic topology of an expanding

spheromak in a single shot. Using this approximate information, contours of constant flux were constructed.

More probes are needed to achieve better accuracy in the magnetic measurements. Using the same off-the-shelf components and custom designs used in the probe presented in this thesis, more probes could be built and inserted in the Caltech chamber through different ports (provided there are sufficient number of digitizers to record all the signals). However, an increase in the number of probes leads to a higher degree of perturbation in the plasma being measured. Thus, a recommendation for future work is to measure this perturbation effect. This could be done by inserting 'dummy' probes (i.e., obstacles similar to the finished probes) and measuring the change in magnetic signals using the existing probe. These measurements would also be relevant to other types of probes or obstacles inserted in the plasma, not only magnetic probes.

Appendix A

Correlation between bright features in the images and the plasma

All the plasma images presented in this thesis were taken in the visible light range. This visible light came from atomic line emission[1] of neutral hydrogen (mostly H_α; hydrogen is the gas most commonly used at SSPX and the Caltech Spheromak Experiment) and helium, depending on the gas used during a particular shot. Because neutrals can easily escape electric and magnetic fields, it is important to question the relation between the light captured by the high-speed camera, and the plasma behavior. Are the neutrals simply entrained by the plasma and their glow telling the position and behavior of filaments and similar features, or are the glowing neutrals unrelated to the position of these plasma features?

The answer to this question is not trivial. It is possible that during a given shot, part of the emitted light is related to the plasma features and then later it is not. However, in the plasmas imaged for this thesis there is evidence that suggests the light indeed corresponds to plasma features. For example, the plasma images in Figure A.1 show the correspondence between the expanding plasma and its toroidal magnetic field (the other two field components are shown in Figure 8.5). The position of the multielement magnetic probe (see Chapter 8) is indicated with a dotted line in each image. The leftmost image shows the plasma shortly after breakdown. The vacuum magnetic field (i.e., the field prior to break-

---

[1]   Photon emission by an atom (or a molecule) arises from the de-excitation of the particle from a higher internal energy state to a lower one. The processes by which a neutral particle in a plasma gains the energy to release a photon are complex. Details of these processes are beyond the scope of this section, and are found in textbooks such as those by Messiah [1] and Griem [2].
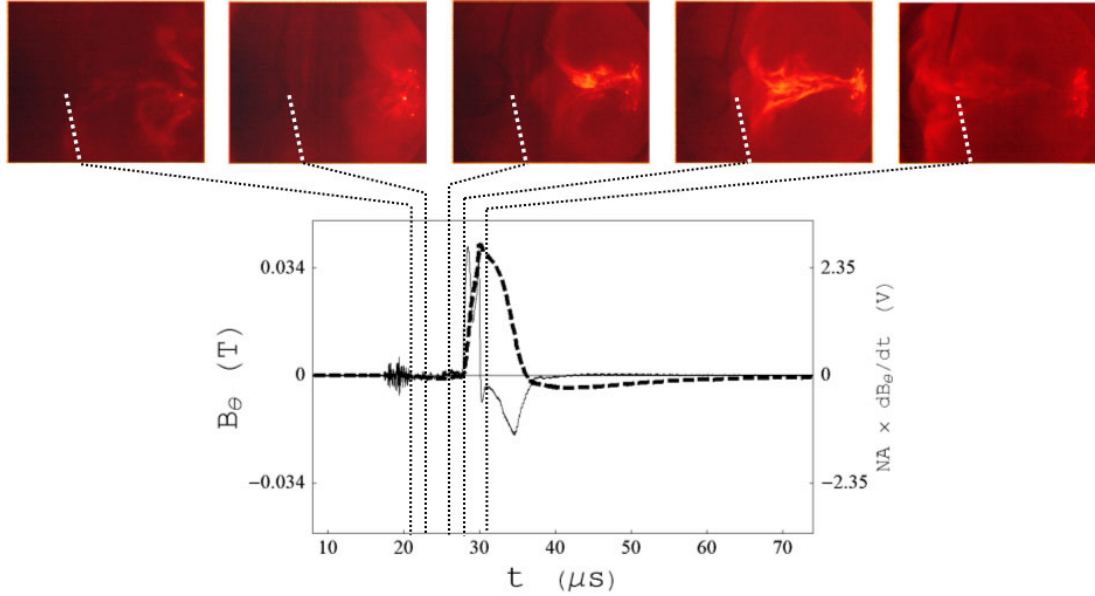
Fig. A.1. Toroidal magnetic field produced by the plasma at the Caltech Spheromak Experiment. The dotted line on each image represents the position of the multielement magnetic probe. The other two field components for this shot are shown in Figure 8.5.

down) has no toroidal component, and thus the only way to have a magnetic signal is if the plasma produces a toroidal field.

The sequence shown in Figure A.1 demonstrates how the probe receives no signal until the bright features reach the probe. In this particular example, the sharp increase in the signal is probably caused by the field at the plasma-vacuum boundary, and later by the vacuum field produced by the central column. After the column seemingly detaches from the gun (rightmost picture), plasma light intensity decreases rapidly and becomes too dim to photograph with the high-speed camera. Thus, light captured by the high-speed camera indicates the presence of plasma, but plasma can also exist without being detected by the camera.

At SSPX the situation is similar. Figure A.2 shows the correspondence between the images and the magnetic signals recorded by the probes mounted on the flux conserver
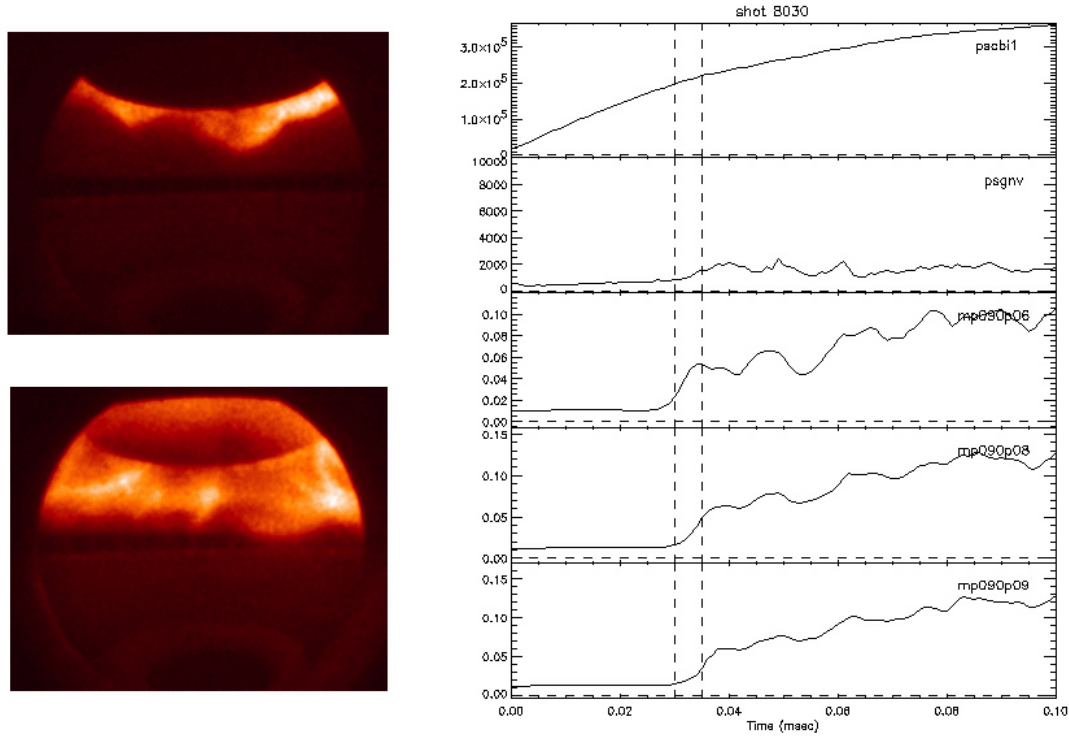
Fig. A.2. Correspondance between magnetic traces (in units of Tesla) and the images captured by the high-speed camera at SSPX. The traces are from probes arranged vertically (at 90° toroidal location) just above midplane. The bottom plot correspond to a probe about 5 cm above midplane, followed by a probe at 10 cm; the third plot corresponds to a probe at 20 cm above midplane. The vertical lines correspond to the time of the first image (top) and the second image (bottom) five microseconds later. The upper plots correspond to the current (top) and the voltage (second from top), in ameperes and volts, respectively.

walls (see Chapter 3 and Figure 2.8 for more details). In this case, however, the correspondence cannot be determined accurately because the probes are just out of the field of view of the camera. Nevertheless, the qualitative behavior is the same as in the previous example. The vertical dotted lines across the plots correspond to the times at which the images were taken. As the plasma travels down from the gun and into the flux conserver (forming the theater curtains described in Chapter 4) the magnetic signal increases in the vertical array of probes along the flux conserver wall (lower three plots in the figure).

It should be noted that, although the presence of bright features in the images is interpreted as being the plasma, the apparent vanishing of those bright features from one image to the next has, in general, a different interpretation between the Caltech Spheromak Experiment and SSPX. At Caltech, the vanishing of the features is attributed to the disconnection of the plasma from the gun. That is, the plasma ceases to receive external power, the ionization percentage decreases, and thus there are less hot ions and electrons to excite the neutrals that emit light. At SSPX, in contrast, the plasma remains coupled to the gun and the decrease in plasma light intensity is attributed to a very high degree of ionization, to the point that there are few or no neutrals that irradiate (visible) light.

A.1 References

[1]   A. Messiah, *Quantum Mechanics,* (Dover Publications, Inc., New York, 1999), pp. 1041 - 1045.

[2]   H. R. Griem, *Plasma Spectroscopy*, (McGraw Hill, New York, 1964), Chapter 2.